University of Sussex

Tools and fundamental techniques for Bose-Einstein condensate microscopy

Timothy Martin James

Submitted for the degree of Doctor of Philosophy

University of Sussex, Brighton, United Kingdom. September 2019

Declaration

I hereby declare that this thesis has not been and will not be submitted in whole or in part to another University for the award of any other degree.

Signature: T M James

Date: September 2019

Acknowledgements

There are a few people I would like to thank for helping make the work here possible. First I would like to thank my supervisors Peter Krüger and Fedja Orucevic for their guidance throughout the project. I would like to thank DSTL for funding the project and for interesting summer workshops throughout the course. I would like to thank and acknowledge Xiaoke Li, Rityan Roy and Amruta Gadge for their help in setting up and running the experiment. I would also like to thank Julia, Tom and Mark for their help and discussions during the project. I would like to thank Dr Manoj Tripathi and Alan Dalton's group for providing me with the atomic force microscopy samples. I would like to thank Hellen Ticktin-Smith for her help with the administration at the end of the PHD. I would like to thank the other people in the lab for helping make my time with the group enjoyable and helping with various bits and pieces and for putting up with my puzzles. I thank my family as I would not have managed this without their support their help throughout the years. Finally I thank Shobita for always being there for me and providing loads of support, especially in the last few months I took to write this.

Abstract

Ultra-cold atoms have small kinetic energy and are therefore very sensitive to external fields that act on the atoms. By having fine control over the positioning of the ultra-cold atom cloud we can use the atom cloud as a sensor for magnetic fields. By imaging these atom clouds we can infer a spatial map of the magnetic field. This spatial map will have a resolution proportional to the distance between the source of the magnetic field and the atom cloud which can be on the order of 0.1 µm. In the first half of the thesis, we investigate the two colour magneto-optical trap. This is a simple technique that can lead to a multiplicative increase in the number of atoms in a magneto-optical trap with a simple change to the optical setup. Using the two colour magneto-optical trap we have observed an increase of 5 times in the number of trapped atoms. An increase in the number of atoms in a magneto-optical helps with later cooling processes that are not lossless such as evaporative cooling which in turn helps the realisation of the ultra-cold atom microscope. In the second half of the thesis, we demonstrate how a 2d current density can be recovered from a 2d magnetic field map generated by the ultra-cold atom microscope. We then go on to show the sensitivity and responsivity of a cold atom cloud and a Bose-Einstein condensate. We then use the results of the previous section to simulate the measurement of currents in a silver nanowire network. Properties of the silver nanowire network can be simulated and aid in showing the abilities and limitations of the ultra-cold atom microscope. We found that the ultra-cold atom microscope can directly measure currents in low-density silver nanowire networks. In a high-density silver nanowire network, the average distance between the wires becomes too small to resolve. Hot-spots, areas of high current density can still be identified using the ultra-cold atom microscope. The ultra-cold atom microscope could then be used as a tool to aid the research look to use silver nanowires in many industrial applications such as touch screens.

Contents

Chapter 1

Introduction

This thesis presents work we undertook towards the implementation and operation of the Bose-Einstein condensate microscope (BEC-M). The BEC-M will be used to measure magnetic fields, on a microscopic scale and spatially close to the sample of interest. In this introduction, we will introduce the key concepts used in this thesis and give an overview of this work in a broader context. To understand the BEC-M we break the subject down into two major fields. First, we will give an overview of the steps involved in forming a BEC and consider other applications of the BEC. Second, we discuss magnetometers, using the BEC as a magnetometer and using the BEC magnetic magnetometer to measure currents in a silver nanowire network.

1.1 Magneto-optical traps

The magneto-optical trap (MOT) is the first stage used in the process of cooling atoms down towards condensing into a BEC. Magneto-optical traps were first demonstrated in the late 80's and early 90's [Raab et al., 1987, Phillips and Metcalf, 1987, Chu, 1992]. This work led to a Nobel prize in physics for Steven Chu, Claude Cohen-Tannoudji and William D. Phillips in 1997 [Phillips, 1998b]. Recently there has been research into a variety of novel methods for generating the magneto-optical trap. These include, a pyramid MOT [Pollock et al., 2009], 3d printed traps [Saint et al., 2018], grating MOT [Lee et al., 2013]. A review of the different trap types can be found in [Barker et al., 2019]. The goal of these techniques is to trap and cool the atoms to as low a temperature as possible. The temperature in a magneto-optical trap is limited by re-scattering of light this temperature is called the Doppler temperature [Metcalf, 1989]. The Doppler temperature depends on the atomic species and for ^{87}Rb the Doppler temperature is 146 µK. There are sub-

Doppler cooling mechanisms that allow the Doppler temperature limit to be surpassed [Steane and Foot, 1991]. The final number of atoms trapped in a the MOT is governed by the interplay between the rate at which atoms are loaded into the trap and the rate atoms are lost from the trap [Prentiss et al., 1988, Marcassa et al., 1993]. Further details are provided in chapter two where we present the theory behind laser cooling and Magneto-optical trapping.

In chapters three and five we investigate a different type of MOT called the two colour (or dual colour) magneto-optical trap due to the second frequency of cooling light. In chapter three we discuss theoretical models to try and explain the effects of the two colour MOT and in chapter five we present the results of experiments done on the two colour MOT. The two colour magneto-optical trap (TCMOT) was first demonstrated by Qiang et al. in [Qiang et al., 2012]. This method involved adding a second cooling beam to the standard setup. More details on the specifics of the setup can be found in chapters four and five. The TCMOT gave a in a three-fold increase in the number of atoms in the trap. In this thesis we further the investigation into the two colour magneto-optical trap, characterising the effects of the second cooling laser and showing the results of experiments to further the theoretical understanding of the two colour magneto-optical trap. There are other 'Two colour' experiments however these use a different scheme to the one outlined in this thesis [Metcalf and van der Straten, 2001] [Kawasaki et al., 2015]. In [Metcalf and van der Straten, 2001] the two frequencies of light are used in an optical trap and are far detuned from resonance. In [Kawasaki et al., 2015] each frequency of light has the opposite circular polarisation to excite systems with a small or zero Zeeman splitting in the excited state.

1.2 Bose-Einstein condensate

In 1995, the first BEC was demonstrated experimentally. This was first done by Eric Cornell and Carl Wieman [Anderson et al., 1995] and was shortly followed by Wolfgang Ketterle [Levi, 2001]. This work was awarded a Nobel prize in physics in 2001 [Ketterle, 2002, Cornell and Wieman, 2002]. A Bose-Einstein condensate (BEC) occurs when the wave function of the individual atoms begin to overlap and can be described as one continuous wave function. The measure of wavefunction overlap is given by the phase space density. The phase space density is a unit-less measure of the number of atoms occupying a given volume in phase space. To increase the atoms phase space density we can either reduce the momentum of the atoms and therefore temperature or decrease the spatial distance

between the atoms via methods such as increasing the tightness of the trap. The transition from a thermal atom cloud to a BEC occurs at a critical temperature that depends on the density of atoms in the trap [Dalfovo et al., 1999]. The critical temperature is usually hundreds of nano-Kelvin. To go from the micro-Kelvin temperatures of the MOT down to the temperatures required for the BEC a different cooling mechanism other than laser cooling is needed. This cooling is done via evaporation which is the same mechanism that cools hot drinks. The atom cloud is suspended using magnetic fields and by applying a radiofrequency field at a precise frequency the hottest atoms are allowed to escape which lowers the average temperature of the remaining atoms [Petrich et al., 1995]. The process of evaporative cooling inherently loses atoms from the trap, therefore, requiring a large initial collection of atoms in the magnetic trap.

1.3 Magnetometry

Magnetometry is the measurement of magnetic fields. There are two types of magnetometer, scalar and vector. A scalar magnetometer measures the magnitude of the magnetic field whilst a vector magnetometer can resolve the individual components of the magnetic field. Today there is a wide range of magnetometers to choose from, a review of modern magnetometers is given in [Edelstein, 2007]. Current magnetometers have a pay off between high sensitivity and resolution so that magnetometers with high spatial resolution will have poor sensitivity and magnetometers with high sensitivity will have poor spatial resolution. Optically pumped magnetometers have been shown to have a sensitivity of less than $1\,\mathrm{fTHz}^{1/2}$ but with a resolution of 2 mm [Kominis et al., 2003]. On the other end of the scale Nitrogen vacancy (N-V) center magnetometers has a micro-Tesla sensitivity and $\sim 500\,\mathrm{nm}$ [Rondin et al., 2014, Tetienne et al., 2017].

1.3.1 Bose-Einstein condensate microscopy

The Bose-Einstein condensate microscope (BEC-M) was first demonstrated to measure magnetic fields in 2005 [Krüger et al., 2005]. Since then the BEC-M has been used as a magnetometer on several occasions [Yang et al., 2017, Vengalattore et al., 2007]. Ultracold atoms have been shown to lie in the middle of this sensitivity-resolution payoff with pico-Tesla sensitivity and micrometre resolution [Wildermuth et al., 2005, Supplementary Figure 2]. To measure magnetic fields from a sample of interest, the BEC can be held in a so-called 1d magnetic trap, where the gradient of the magnetic fields is large in two directions and small in the third. This has the effect of confining the atoms into a long

thin cylinder. In the weak trapping direction, the atoms are sensitive to inhomogeneous external fields in the direction of the weak trapping axis. The external magnetic fields changes the local atom density of the BEC, this change in the local atom density is measured using absorption imaging, which is covered in more detail in chapter four. By measuring the changes in local atom density we can measure the external magnetic field. In this configuration, the BEC is a one-axis vector magnetometer. The BEC could also be placed in a 2d optical trap and measure a 2d scalar magnetic field, which has the advantage of measuring and area simultaneously. The sensitivity of the BEC magnetometer depends on the number of atoms in the BEC, the trapping frequencies and the resolution of density variations. High-resolution imaging allows for variations as small as one atom per micron to be measured. The magnitude of the density variations can be controlled by tuning the strength of the interactions between the atoms [Chin et al., 2010].

1.4 Silver nanowires

The BEC-M is ideally suited for directly measuring the current in silver nanowires. Over the last decade, the demand transparent conductors have increased at an unprecedented pace. Currently, Indium tin oxide (ITO) is the most widely used transparent conductor. Recently there has been a lot of interest in alternate transparent conductors to reduce the demand for ITO [Minami, 2008] [Kumar and Zhou, 2010]. Silver nanowires (AgNWs) and reduced graphene oxide/silver nanowire (R/AgNWs) networks have shown to be a promising contender to ITO [Park et al., 2015][Hong et al., 2015].

However, there are still problems to overcome, such as junction burnout and wire drift [Fantanas et al., 2018][Langley et al., 2014], before silver nanowires can replace ITO. Currently researches use conductive atomic force microscopy (CAFM) [Shaw et al., 2016], lock-in thermography (LiT) [Sannicolo et al., 2016] and

Kelvin probe microscopy [Vinaji et al., 2009] to probe the properties of the AgNW networks. However, with such methods, it is not currently possible to directly measure the current in the AgNW network on a microscopic scale. Direct measurements of current flow in silver nanowires would allow effects such as the emergence of winner-takes-all connectivity paths [Manning et al., 2018] and spontaneous changes in current paths due to heating [Das et al., 2016] to be investigated. This would allow further development of silver nanowires in industry.

1.4.1 Measuring silver nanowires with the BEC-M

In chapter seven we go show the results of a simulation of the BEC-M measuring currents in a silver nanowire network. To directly measure the current paths in a silver nanowire network we would move the atom cloud over the surface and measure the density changes in the BEC. These density changes allow one component of the magnetic field generated by the silver nanowires to be measured. The smaller the distance between the BEC and the surface of the sample, the better the magnetic field can be resolved spatially. This is due to the smoothing of the magnetic field as the distance to the source increases [Roth et al., 1989]. The minimum distance between the BEC and the surface is limited by the lifetime of the BEC near the surface. Effects such as the Casimir force [Casimir and Polder, 1948] and Johnson Nyquist noise limits the lifetime of the BEC. The rate at which a scan of the silver nanowires can be taken is limited by the rate at which a BEC is made. This can be done in as little as one second [Rudolph et al., 2015]. Currently, each image of the BEC is destructive so that a new cloud needs to be formed for the next run. Non-destructive measurement techniques such as Phase-contrast imaging [Durfee and Ketterle, 1998] could be used to further increase the repetition rate of imaging the atomic cloud.

1.4.2 Thesis layout

- Chapter 2: This chapter begins with a detailed description of light-atom interactions and a derivation of the optical Bloch equations which is relevant for chapter 3. We then go on to present theoretical concepts used in magneto-optical trapping.

- Chapter 3: This chapter uses the derivation of the optical Bloch equations in chapter 2 and modifies the equations to include a second light field. The consequences of adding the second light field are then explored.

- Chapter 4: Presents a technical description and methods of the experimental apparatus. We outline modifications required for the two colour magneto-optical trap experiment.

- Chapter 5: In this chapter, we present the characterisation of the TCMOT. We then present and discuss the results of the measurement of the force of the TCMOT. Finally, we give a framework in which the TCMOT can be optimised for other ultracold atom experiments.

- Chapter 6: In this chapter, we give a theoretical framework for the ultra-cold atom microscope. We outline the method to calculate the sensitivity and responsivity of both the thermal atom cloud and the BEC. We then compare the thermal atom cloud to the BEC-M and outline when to use thermal atoms instead of a BEC.
- Chapter 7: Silver nanowires are an interesting sample to test the BEC-M. In this chapter, we first outline the steps used to simulate the silver nanowire network. We then demonstrate how the current paths can be recovered from measurements of the magnetic fields above the silver nanowires. We then show results of the simulations of the BEC-M measuring the magnetic fields from silver nanowires. This includes a comparison to CAFM data.
- Chapter 8: This chapter summaries the work done in the thesis and concludes with a discussion on future work including a discussion of possible methods for solving the unconstrained inverse problem that was outlined in chapter 7.

1.4.3 List of acronyms

- Magneto-optical trap (MOT)
- Two colour magneto-optical trap (TCMOT)
- Bose-Einstein condensate (BEC)
- Bose-Einstein condensate microscope (BEC-M)
- Acoustic optical modulator (AOM)
- Radio frequency (RF)
- Silver nanowires (AgNW)
- Atomic force microscope (AFM)
- conductive atomic force microscope (CAFM)
- Printed circuit board (PCB)

Chapter 2

Light atom interactions theory

The magneto-optical trap (MOT) uses lasers and magnetic fields to cool and trap atoms and is a fundamental tool in cold atom experiments [Lu et al., 1996]. One of the main topics covered in this thesis is the so-called two colour magneto-optical trap (TCMOT). It is necessary to understand the theory behind the single colour MOT to gain insight into the TCMOT. In this section, we will present the theory for a two-level atom interacting with a light field using a density matrix formalism. It is still worth presenting a formalism that will be used when applying these methods to the TCMOT. We will show how the density matrix formalism is used to describe the cooling and trapping of the atoms using magnetic fields and laser light. The methods will use a semi-classical approximation such that we treat the light as a wave rather than individual photons. The majority of material in this section is covered by [Metcalf and van der Straten, 2001, Foot et al., 2005, Steck, 2007, Cohen-Tannoudji et al., 1998, Le Kien and Hakuta, 2004]. This chapter will also cover a theoretical description of some of the experimental aspects of the MOT such as loading rate and Zeeman splitting.

2.1 Light atom interactions

In this section we introduce the description of the two-level atom interacting with the light field. We will use the density matrix formalism as described in [Cohen-Tannoudji et al., 1998] to show how the state of the two-level atom changes when it interacts with a light field.

2.1.1 The two-level atoms

The two-level atom is a theoretical model used to gain insights into real atom-light interactions. A two-level atom would have a single outer electron which can only occupy

one of two energy levels, the ground state denoted by $|g\rangle$ and the excited state denoted by $|e\rangle$ [Le Kien and Hakuta, 2004]. This is represented diagrammatically in figure (2.1). The electron can also occupy a linear superposition of the ground and excited states [Davis, 1996].

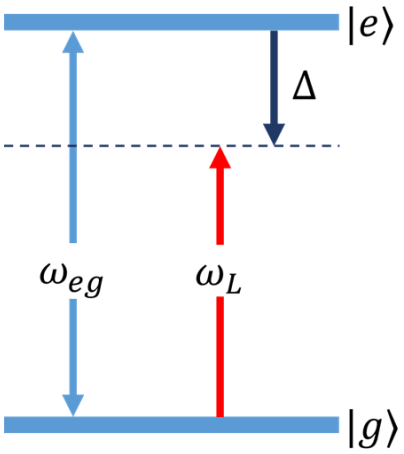

Figure 2.1: The energy diagram of the two level atom with an incident laser beam. The ground and excited states are denoted by $|g\rangle$ and $|e\rangle$ respectively. ω_{eg} is the difference in angular frequency between the ground and excited states. ω_L represents the angular frequency of an incident laser beam and $\Delta = \omega_L - \omega_{eg}$.

The ground state and excited states have associated energy, E_e and E_g respectively. It is often a standard practice to set E_g to zero. The Hamiltonian for a two-level atom in [Cohen-Tannoudji et al., 1998, p. 388]

$$H_0 = \begin{pmatrix} \hbar\omega_e & 0 \\ 0 & \hbar\omega_g \end{pmatrix}, \tag{2.1}$$

where $\omega_k = E_k/\hbar$. This Hamiltonian describes the two-level atom in the absence of an external field and will remain the same thorough this section and in the two colour theory section.

2.1.2 Wave function

The evolution of a quantum system in time is given by the time dependant Schrödinger equation [Kosloff and Kosloff, 1983]. The time dependant Schrödinger equation is given

by.

$$H\left|\psi\right\rangle = \frac{i}{\hbar}\frac{\partial}{\partial t}\left|\psi\right\rangle . \tag{2.2}$$

The Schrödinger equation is linear with respect to the wave function $|\psi\rangle$, this means that a solution to the Schrödinger equation can be expressed as [Metcalf and van der Straten, 2001]

$$\left|\psi\right\rangle = \sum_{k=1}^{n} c_k \left|\phi_k\right\rangle . \tag{2.3}$$

Here $|\phi_k\rangle$ are the eigen-states of the Schrödinger's equation and c_k is the probability amplitude to find $|\psi\rangle$ in the state $|\phi_k\rangle$. c_k is a complex value that sets both the magnitude and phase of the state $|\phi_k\rangle$. n is the number of eigen-states the sysem has. The two level system has two eigenstates and therefore $n = 2$. These probability amplitudes are usually time dependant, for example, for the two level system the general solution is given by,

$$\left|\psi\right\rangle = c_e \left|\phi_e\right\rangle + c_g \left|\phi_g\right\rangle . \tag{2.4}$$

This only holds when the system is in a pure state [Metcalf and van der Straten, 2001]. If the system is in a mixed state then a more complete formalism is needed. In the absence of external fields the time evolution of c_e and c_g is [Le Kien and Hakuta, 2004]

$$\begin{aligned} c_e(t) &= e^{-\omega_e t} c_e(0) \\ c_g(t) &= e^{-\omega_g t} c_g(0). \end{aligned} \tag{2.5}$$

The magnitude of c_e and c_g is constant but c_e and c_g rotate in complex space. The angular frequency of the rotation for c_e and c_g is ω_e and ω_g respectively.

2.1.3 Density operator

In experiments we can not directly measure $|\psi\rangle$ and will instead measure the expectation value for an operator [Cohen-Tannoudji et al., 1998, p. 353]. We then describe the system in terms of its density operator

$$\rho = \left|\psi\right\rangle \left\langle\psi\right| . \tag{2.6}$$

In the case of a pure state, ρ is given by,

$$\rho_{ij} = c_i c_j^*, \tag{2.7}$$

where * denotes the complex conjugate. The diagonal terms $\rho_{ii} = |c_i|^2$ given the probability that the system is in state i. The off-diagonal terms give the coherence's between state i and j. The coherence is dependant of the phase difference between the two states c_i and c_j. For the two level atom the off diagonal of the density matrix is,

$$\rho_{eg}(t) = c_e(t)c_g^*(t) = c_e(0)c_g(0)e^{-(\omega_e - \omega_g)t}. \tag{2.8}$$

This rotates in complex space at a rate

$$\omega_{eg} = \omega_e - \omega_g. \tag{2.9}$$

This result is used later in section (2.1.5).

When the system is described by a statistical mixture this definition of the density operator no longer holds. The density operator is now defined as

$$\rho = \sum_k p_k \left|\phi_k\right\rangle \left\langle\phi_k\right|, \tag{2.10}$$

where p_k is the probability that the system is in state k. The two-level system the density matrix is defined as

$$\rho = \begin{pmatrix} c_e c_e^* & c_e c_g^* \\ c_g c_e^* & c_g c_g^* \end{pmatrix} = \begin{pmatrix} \rho_{ee} & \rho_{eg} \\ \rho_{eg}^* & \rho_{gg} \end{pmatrix} \tag{2.11}$$

2.1.4 Interaction Hamiltonian

The interaction between the two level atom and an incident light field is described by the interaction Hamiltonian [Steck, 2007].
The general interaction Hamiltonian is [Metcalf and van der Straten, 2001],

$$H_I = -\vec{d} \cdot \vec{E}, \tag{2.12}$$

where $\vec{d}$ is the transition dipole matrix and $\vec{E}$ is the electric field. In the case of the light field interacting with the two level atom the electric field is described as,

$$\vec{E} = \frac{E_0 \vec{\epsilon}}{2}(e^{-i\omega_L t} + e^{i\omega_L t}). \tag{2.13}$$

Here $\vec{\epsilon}$ is the polarisation vector, E_0 is the amplitude of the laser field and ω_L is the frequency of the light. The full interaction Hamiltonian is given by,

$$H_I = -\frac{\hbar}{2}(\left|e\right\rangle \left\langle g\right| + \left|g\right\rangle \left\langle e\right|)(\Omega e^{-i\omega_L t} + \Omega^* e^{i\omega_L t}). \tag{2.14}$$

Here Ω is the Rabi frequency, $\left|e\right\rangle \left\langle g\right|$ and $\left|g\right\rangle \left\langle e\right|$ describe the coherence between the ground and excited states.
For a more indepth derrivation of these equations see [Metcalf and van der Straten, 2001, Steck, 2007]. As we saw in 2.1.3 $\left|e\right\rangle \left\langle g\right|$ and $\left|g\right\rangle \left\langle e\right|$ rotate in the complex plane at a rate $-\omega_L$ and ω_L respectively. We perform a rotating wave approximation by expanding H_I and removing terms rotating at $\omega_L + \omega_{eg}$ whilst keeping terms that rotate at $\omega_L - \omega_{eg}$ we find,

$$H_I = -\frac{\hbar}{2}\Big(\Omega \left|e\right\rangle \left\langle g\right| e^{-i\omega_L t} + \Omega^* \left|g\right\rangle \left\langle e\right| e^{i\omega_L t}\Big). \tag{2.15}$$

This equation describes the interaction of the light field with the two level atom. Combining the interaction Hamiltonian with the Hamiltonian for a two level atom we find

$$H = H_0 + H_I = \hbar \left(\omega_e \left|e\right\rangle \left\langle e\right| + \omega_g \left|g\right\rangle \left|g\right\rangle - \frac{1}{2}\Big(\Omega \left|e\right\rangle \left\langle g\right| e^{-i\omega_L t} + \Omega^* \left|g\right\rangle \left\langle e\right| e^{i\omega_L t} \Big) \right) \quad (2.16)$$

We will use this equation in the next section to calculate the time evolution of the density matrix and derive the optical Bloch equations.

2.1.5 Time evolution of the density matrix

The time evolution of the density matrix is given by [Bason et al., 2009]

$$\frac{d\rho}{dt} = -\frac{i}{\hbar}[H, \rho], \quad (2.17)$$

where [.,.] denotes the commutation relation. As both H and ρ are matrices the commutation relation is the difference in the multiplication of matrices.

$$\frac{d\rho}{dt} = \begin{pmatrix} -\frac{i}{2}(\Omega^* \rho_{eg} e^{i\omega_L t} - \Omega \rho_{eg}^* e^{-i\omega_L t}) & -i\omega_{eg}\rho_{eg} + i\Omega e^{-i\omega_L t}(\rho_{gg} - \rho_{ee}) \\ i\omega_{eg}\rho_{eg}^* - i\Omega^* e^{-i\omega_L t}(\rho_{gg} - \rho_{ee}) & \frac{i}{2}(\Omega^* \rho_{eg} e^{i\omega_L t} - \Omega \rho_{eg}^* e^{-i\omega_L t}) \end{pmatrix}. \quad (2.18)$$

We now have equations for the evolution of the elements of $\dot{\rho}$.

$$\begin{aligned} \dot{\rho}_{ee} &= -\frac{i}{2}(\Omega^* \rho_{eg} e^{i\omega_L t} - \Omega \rho_{eg}^* e^{-i\omega_l t}) \\ \dot{\rho}_{gg} &= \frac{i}{2}(\Omega^* \rho_{eg} e^{i\omega_L t} - \Omega \rho_{eg}^* e^{-i\omega_l t}) \\ \dot{\rho}_{eg} &= -i\omega_{eg}\rho_{eg} + i\Omega e^{-i\omega_L t}(\rho_{gg} - \rho_{ee}). \end{aligned} \quad (2.19)$$

We have not included ρ_{ge} as $\rho_{ge} = \rho_{eg}^*$. We then perform a rotational co-ordinate transformation to remove time dependant parts of equations (2.19)

$$\tilde{\rho}_{eg} = \rho_{eg} e^{i\omega_L t}. \quad (2.20)$$

We now apply the transformation to equations (2.19), remembering that

$$\dot{\tilde{\rho}}_{eg} = \dot{\rho}_{eg} e^{i\omega_L t} + i\omega_L \tilde{\rho}_{eg}. \quad (2.21)$$

Finally giving a set of time-dependent coupled differential equations,

$$\begin{aligned} \dot{\rho}_{ee} &= -\frac{i}{2}(\Omega^* \tilde{\rho}_{eg} - \Omega \tilde{\rho}_{eg}^*) \\ \dot{\rho}_{gg} &= \frac{i}{2}(\Omega^* \tilde{\rho}_{eg} - \Omega \tilde{\rho}_{eg}^*) \\ \dot{\tilde{\rho}}_{eg} &= i\Delta\tilde{\rho}_{eg} + \frac{i\Omega}{2}(\rho_{gg} - \rho_{ee}), \end{aligned} \quad (2.22)$$

where $\Delta = \omega_L - \omega_{eg}$ and so is negative for red detuned laser light. These equations describe the two-level system interacting with a light field.

2.1.6 Optical Bloch equations

In the previous section we described the interaction of the two level atom with a light field. This picture has so far neglected decay into the ground state either by collisions or spontaneous emission. In this derivation we only consider spontaneous decay. Spontaneous decay is added in to these equations using the Lindblad superoperator [Steck, 2007]

$$\frac{d\rho}{dt} = -\frac{i}{\hbar}[H, \rho] + \Gamma D[\sigma]\rho. \tag{2.23}$$

Where the Lindblad superoperator is defined as,

$$D[\sigma]\rho = \sigma\rho\sigma^\dagger - \frac{1}{2}(\sigma^\dagger\sigma\rho + \rho\sigma^\dagger\sigma). \tag{2.24}$$

In this case σ and $\sigma^\dagger$ are $|g\rangle\langle e|$ and $|e\rangle\langle g|$ respectively. Using the matrix forms of $|e\rangle\langle g|$ and $|g\rangle\langle e|$ we can now express the Lindblad superoperator as

$$D[|e\rangle\langle g|]\rho = \begin{pmatrix} \rho_{ee} & \frac{\rho_{eg}}{2} \\ \frac{\rho^*_{eg}}{2} & -\rho_{ee}. \end{pmatrix} \tag{2.25}$$

Putting together equations (2.23), (2.25) and (2.19) and combining ρ_{gg} and ρ_{ee} into the difference between populations, $w = \rho_{gg} - \rho_{ee}$ we finally get,

$$\dot{w} = \Gamma(1 - w) - \frac{i}{2}(\Omega^*\tilde{\rho}_{eg} - \Omega\tilde{\rho}^*_{eg}) \tag{2.26a}$$

$$\dot{\tilde{\rho}}_{eg} = (i\Delta - \frac{\Gamma}{2})\tilde{\rho}_{eg} + \frac{i\Omega w}{2}. \tag{2.26b}$$

These equations can be solved numerically and have been shown in figure (2.2)

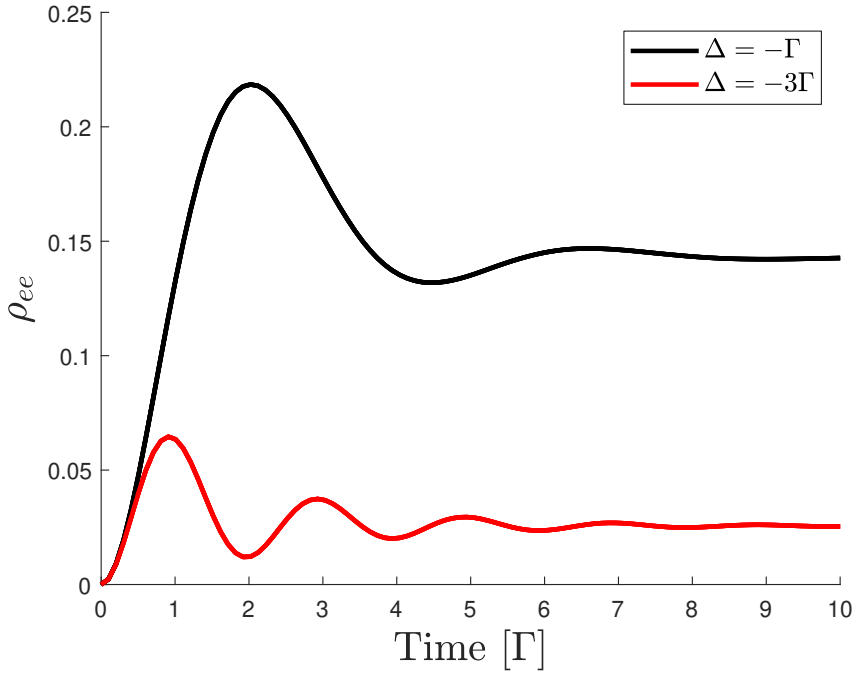

Figure 2.2: The figure shows the probability an atom is in the excited state for two different detunings of the incident light. Initially the system oscillates with a frequency Ω. These oscillations exponentially decay leaving the system in a steady state. In both cases $\Omega = \Gamma$.

Whilst a fully analytic solution to these equations is not possible [Metcalf and van der Straten, 2001], it is possible to find an analytic solution to the steady-state values of the system. These are given by [Metcalf and van der Straten, 2001].

$$w(t \to \infty) = \frac{1}{1+s}. \tag{2.27a}$$

$$\rho_{eg}(t \to \infty) = \frac{i\Omega}{2(\frac{\Gamma}{2} - i\Delta)(1+s)}, \tag{2.27b}$$

where

$$s = \frac{s_0}{1 + (\frac{2\Delta}{\Gamma})^2} \tag{2.28}$$

and

$$s_0 = I/I_s = \frac{2|\Omega|^2}{\Gamma^2}. \tag{2.29}$$

Here, I is the intensity of the incoming light field and I_s is the saturation intensity which depends on the exact transition so s_0 is a measure of saturation.

2.1.7 Scattering rate

The scattering rate is defined as the excited state decay time multiplied by the probability the atom is in the excited state [Phillips, 1998a],

$$\gamma_s = \Gamma \rho_{ee}. \tag{2.30}$$

As the probability of being in the excited state ρ_{ee} is limited to $\frac{1}{2}$, the maximum scattering rate is limited to $\Gamma/2$. The scattering rate affects several different mechanisms involved in laser cooling.

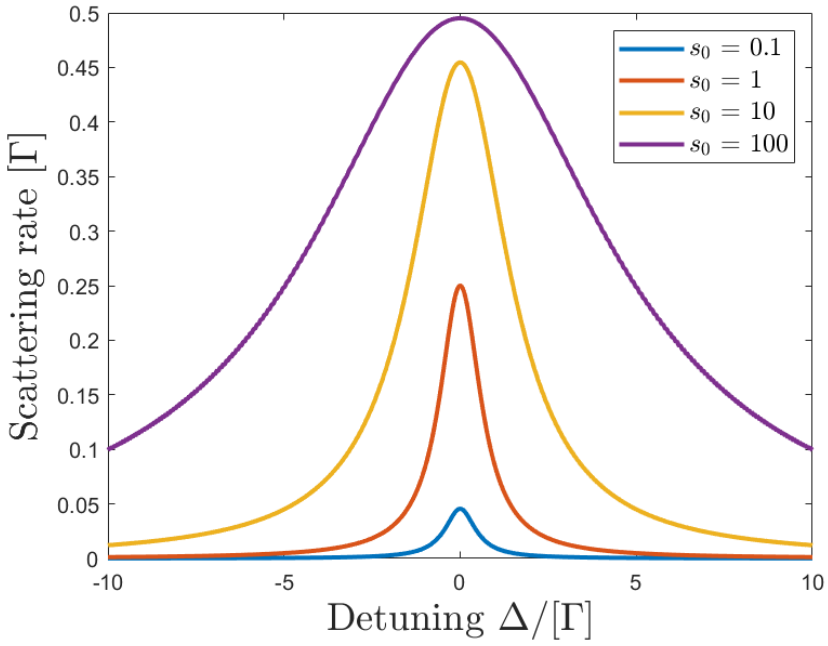

Figure 2.3: Scattering rate as function of detunting for different s_0 values. The detuning and scattering rate are measured in units of Γ. At larger optical intensities the peak scattering rate approaches the saturation values of $\Gamma/2$.

At higher optical power the width of the peak increases, this is called power broadening. Figure (2.3) shows that for low optical power $s_0 < 10$ that the scattering rate is a Lorentzian function with a linewidth of Γ. This scattering rate concept will be important when considering the TCMOT as it is fundamental in understanding the effects of the two colour MOT and the push beam.

2.1.8 Force on a two-level atom

The main motivation behind the theory above is to derive a model for the force on an atom from a laser with a given frequency and intensity. We could begin with a naive model

for the force on a two-level atom. First, when an atom absorbs a photon the momentum carried by the photon, $\hbar k$, is transferred to the atom [Nichols and Hull, 1903]. Second, the atom re-emits the photon. The direction of the re-emitted photon from the atom is random. Over a large number of emissions the momentum kick from this photon will average to zero. The rate at which one absorption and re-emission cycle happens is $\Gamma\rho_{ee}$. Combining all these elements the force, which is equal to the rate of momentum transfer, is given by

$$F = \hbar k \Gamma \rho_{ee}. \tag{2.31}$$

However, this does not give a complete picture of force on the two-level atom. Instead, a more complete picture can be derived by first, starting with the Ehrenfest equation for the force,

$$F = \langle F \rangle = -\left\langle \frac{\partial H}{\partial x} \right\rangle. \tag{2.32}$$

Using the result that $\langle \mathcal{A} \rangle = Tr(\rho A)$ and that H_0 has no spatial dependence we find that,

$$F = -\frac{\hbar}{2}\left(\frac{\partial \Omega}{\partial x}\rho^*_{eg} + \frac{\partial \Omega^*}{\partial x}\rho_{eg} \right). \tag{2.33}$$

To calculate $\partial\Omega/\partial x$ we use a logarithmic derivative. The derivative of the log of a function is,

$$\frac{\partial \log(f(x))}{\partial x} = \frac{\partial f(x)/\partial x}{f(x)}. \tag{2.34}$$

We can rearrange this equation for $\partial f(x)/\partial x$,

$$\frac{\partial f(x)}{\partial x} = f(x)\frac{\partial \log(f(x))}{\partial x}. \tag{2.35}$$

The logarithmic derivative is used in cases where it is easier to calculate the derivative of the log of a function than the function its self. Applying the logarithmic derivative to $\partial\Omega/\partial x$ we find,

$$\frac{\partial \Omega}{\partial x} = (q_r + iq_i)\Omega, \tag{2.36}$$

where,

$$(q_r + iq_i) = \frac{\partial \log(\Omega)}{\partial x}. \tag{2.37}$$

The separation of $\partial\Omega/\partial x$ into real and imaginary parts is motivated by the end result of this derivation . Substituting equation (2.36) into (2.33) gives,

$$F = \frac{\hbar}{2}\left(q_r\Big(\Omega\rho^*_{eg} + \Omega^*\rho_{eg}\Big) + iq_i\Big(\Omega\rho^*_{eg} - \Omega^*\rho_{eg}\Big) \right). \tag{2.38}$$

The corresponding equation in [Metcalf and van der Straten, 2001], equation (3.9) is missing a factor of 1/2 which has been included here. For a travelling wave with an electric field given by

$$E(x) = \frac{E_0}{2}\left(e^{i(kx-\omega_t)} + e^{-i(kx-\omega_t)}\right). \tag{2.39}$$

From this we find that,

$$\frac{\partial \log \Omega}{\partial x} = k \tag{2.40}$$

therefore $q_r = 0$ and $q_i = k$. A physical way to interpret q_r and q_i is that q_r is the gradient of the amplitude of the wave, as is found in standing waves. Where q_i is the gradient of the phase of the wave, as has been shown for the travelling wave [Steck, 2007]. We can substitute equations (2.27b) for the steady state solution for ρ_{eg} into (2.38) we find that

$$F = \hbar k \Gamma \rho_{ee}, \tag{2.41}$$

which is the same result as was found from the naive view of the momentum transfer. The naive approach will break down in the next chapter when we consider two light fields with different but similar frequencies.

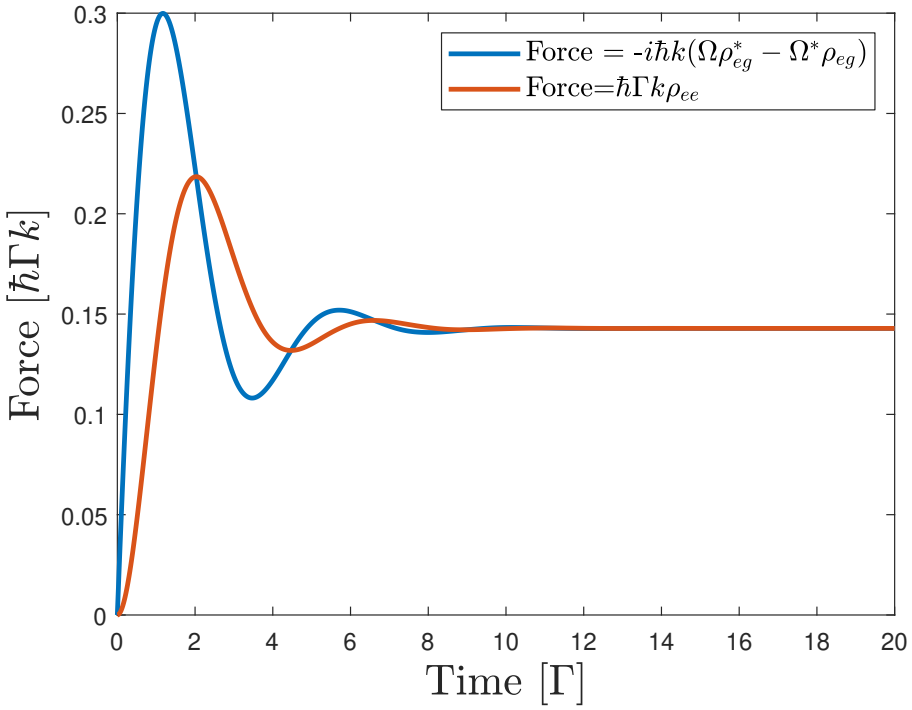

Figure 2.4: Force from a single light field with $\Omega = \Gamma$ and $\Delta = -\Gamma$. Initially the two force calculations give different values however once the Rabi oscillations have decayed the two equations give the same result.

Doppler shift of the incident light is incorporated into the system of equations by adding a velocity-dependent term to the detuning of the laser from resonance. In one

dimension the velocity dependant frequency shift is,

$$\Delta_{\pm} = \Delta \mp k \cdot v. \tag{2.42}$$

The $\mp$ term accounts for the direction of the two counter-propagating beams as the frequency shift of the light is directional dependant. Using this modification we can calculate the force from a pair of counter-propagating beams on a two-level atom. The intensity of the beams is assumed low enough that the scattering rate from each beam can be treated separately.

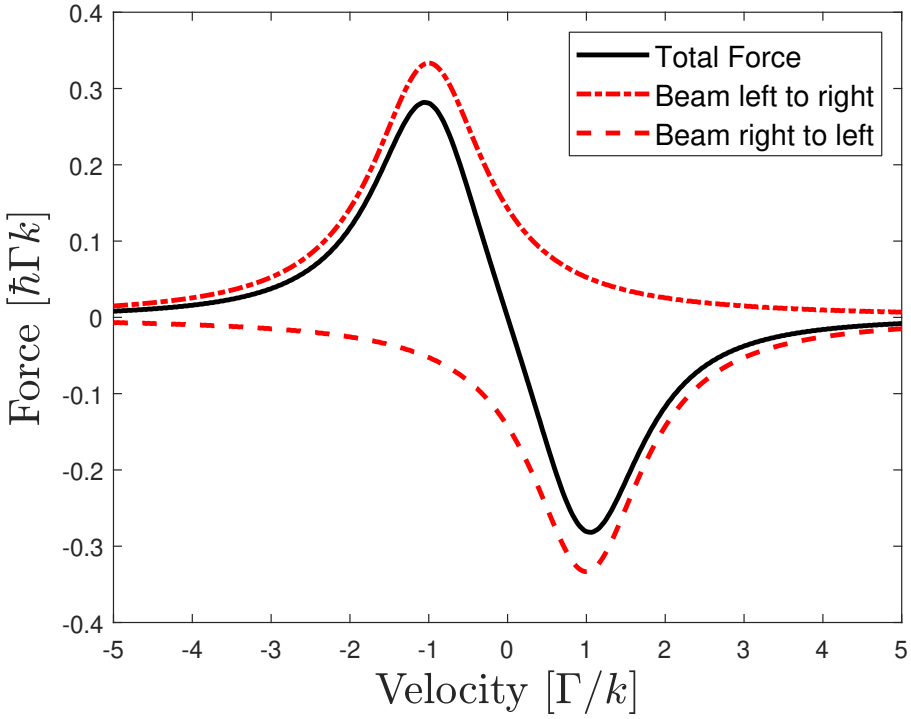

Figure 2.5: Force on an atom as a function of velocity. There are two counter-propagating beams. Each beam has an intensity of $\Omega = \Gamma$ and a detuning of $\Delta = -\Gamma$. The sum of the forces as a function of velocity is depicted by the black curve. When the velocity of the atoms is less than Γ/k then the force is approximately linear

The force applied by the incident beams on the atoms depends on velocity of the atoms. This dependence leads to the deceleration of the atoms. Without positional based trapping the velocity dependant deceleration of the atoms is called optical molasses. To trap the atoms spatially we add a linear magnetic field gradient to induce a position dependence on the force. This is covered in more detail in (2.2).

2.1.9 Doppler temperature

It should be noted that the concept of temperature does not strictly apply to atoms in a MOT as it is not in equilibrium. Instead, in later sections, we will use temperature as a way to express the energy using the relation $k_bT = mv^2$ where k_b is the Boltzmann constant. Optical molasses cools the atoms to a finite temperature where the random re-emissions of photons can no longer be averaged to zero. The re-emission of the photons causes the atoms to undergo a random walk in momentum space. The heating rate is given by [Foot et al., 2005]

$$\dot{E}_{heat} = \frac{\hbar^2 k^2}{2m}\gamma\rho_{ee}. \tag{2.43}$$

Here $\hbar^2k^2/2m$ is the energy the atom gains from each re-emitted photon and $\gamma\rho_{ee}$ is the rate at which this process happens. At the cooling limit, the velocities of the atoms are small therefore the force can be expanded to the first order in velocity giving,

$$F = -\alpha v, \tag{2.44}$$

and the cooling rate is given by

$$\dot{E}_{cool} = F\dot{v} \simeq -\alpha v^2, \tag{2.45}$$

where α is approximated by the linear part of the force velocity curve.

$$-\alpha v \simeq \frac{8\hbar k^2 \Delta s_0}{\Gamma(1 + s_0 + (\frac{2\Delta}{\Gamma})^2)^2} v. \tag{2.46}$$

The negative sign arises from Δ if the laser were blue detuned then the force would accelerate the atoms away from the centre of the trap. Equating the heating rate with the cooling rate we get an expression for the steady-state velocity, which we express as v^2 so that it is easier to relate to the temperature.

$$v^2 = \frac{\hbar^2 k^2}{2m\alpha}\rho_{ee}. \tag{2.47}$$

The heating rate gives a limit to how much the atoms are be cooled by laser light. For an ideal system with $s_0 = 2$ and $\Delta = -\Gamma/2$, which minimises the laser cooling limit is called the Doppler temperature and is given by $T_D = 146\,\mu\text{K}$. This assumes there are no sub-Doppler cooling mechanisms, such as Sisyphus cooling [Foot et al., 2005], that allow for colder temperatures to be reached in experiments.

2.2 Magneto-optical trapping

Atoms in optical molasses will undergo a random walk in phase space [Foot et al., 2005]. The random walk will eventually result in the atoms leaving the cooling region. To trap the atoms spatially there needs to be a restoring force pushing the cold atoms back towards the centre of the MOT.

2.2.1 Hyperfine splitting

It was shown by Pieter Zeeman [Feynman, 1965] that the hyperfine levels of an atomic transition can be split by an external magnetic field. A more complete model for this splitting can be found at [Foot et al., 2005], however, the majority of the details are not necessary for the understanding of laser cooling. Below 0.1 T the distance between Zeeman sub-levels is a linear function of the magnetic field. If we consider the two-level atom in one dimension, the magnetic field causes the excited state to split into 3 energy levels.

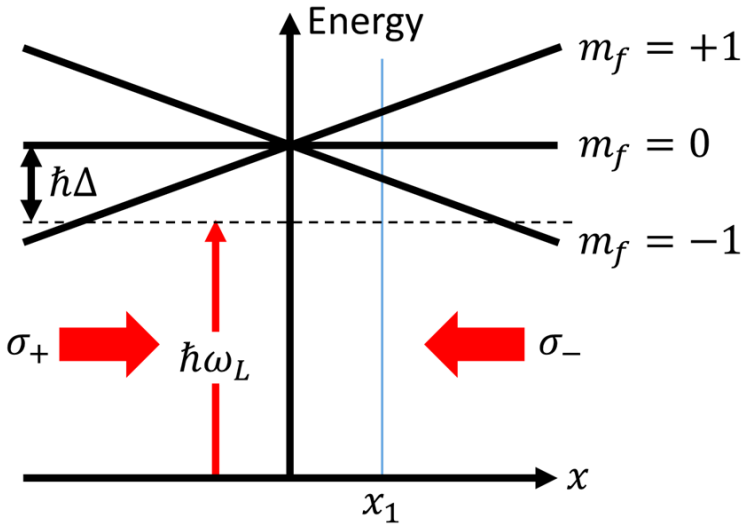

Figure 2.6: A breakdown of a MOT setup in 1d. The red arrows represent the incident laser beams on the two-level atom. The dotted line represents the energy level of the laser light. Each beam is circularly polarized. The σ_+ light will interact with the $m_f = +1$ state whilst σ_- will interact with $m_f = -1$ state. At the position x_1 the Zeeman shift has changed the excited state energy levels such that the σ_- light is closer to resonance than the σ_+ light.

In a magnetic field with a linear gradient, the magnitude of the energy levels splitting

is position-dependent. The linear gradient is generated by a pair of anti-Helmholtz coils [Bergeman et al., 1987]. Consider an atom at rest in figure (2.6), the σ_- beam is closer to resonance than the σ_+ beam due to the splitting of energy levels. This causes an imbalance in the force, accelerating the atom towards the centre of the trap.

The detuning of the light is now expressed as [Metcalf and van der Straten, 2001],

$$\Delta_\pm = \Delta \mp k \cdot v \pm \frac{\mu' A x}{\hbar}, \tag{2.48}$$

here A is the gradient of the magnetic field which for most MOT experiments is between $8\,\mathrm{G/cm}-15\,\mathrm{G/cm}$. μ' is the effective magnetic moment [Metcalf and van der Straten, 2001] For a real ensemble of atoms all magnetic states need to be considered when calculating μ'. When the atoms are being cooled and trapped the velocity distribution becomes squeezed. The atoms are pushed towards the velocity class such that $\Delta_\pm = 0$ where the force between the two counter-propagating beams is zero. This squeezing is highlighted in figure (2.7) in the next section.

2.2.2 Capture velocity

In a MOT the diameter of the beams defines a region in which the atoms are decelerated. An atom is captured when it enters this region with a velocity lower than a capture velocity. The most basic way to describe the capture velocity is to consider an atom that enters the trapping region at v_c and reaches the other side of the trapping region with $v = 0$ where the atom will be pushed back into the trap. Atoms with a velocity $v > v_c$ will escape the trap. As the trapping force is non-linear and depends on both position and velocity it is very difficult to analytically calculate the capture velocity of a MOT. The capture velocity can, however, be calculated numerically in 1d. To calculate the trajectories of the atoms in 1d we use Matlab's ode45 function to numerically solve a set of differential equations. The ode45 function numerically solves differential equations using a 4th or 5th order Runge-Kutta formula [Dormand and Prince, 1980]. In one time step we solve the optical Bloch equations stated in (2.26a) and (2.26b), the force on the atom using equation (2.41) and the equations of motion of the atom assuming the acceleration on the atom is $a = F/m$ where m is the mass of the atom and F is the force calculated from (2.41).

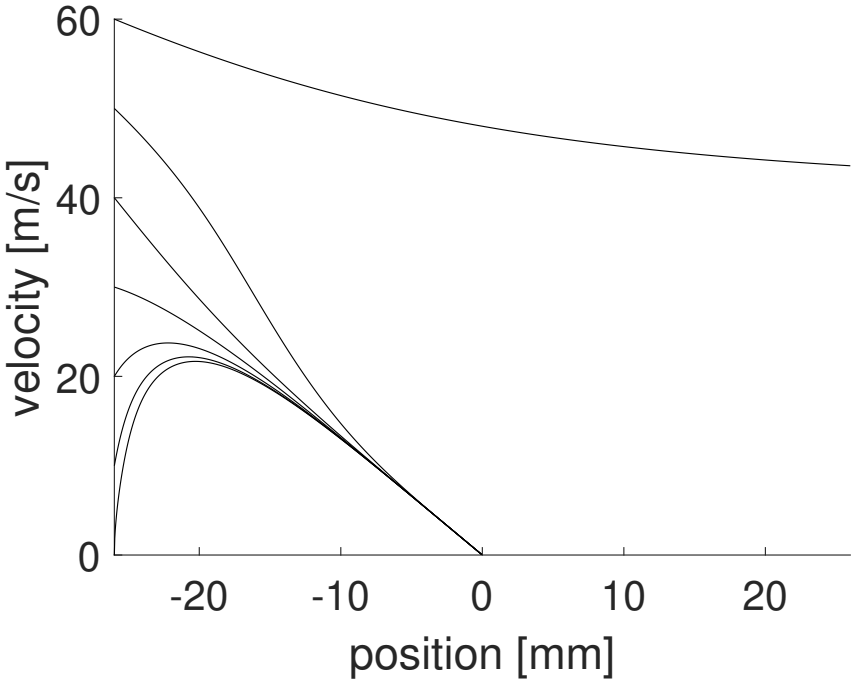

Figure 2.7: Trajectories for a range of different initial velocities. The initial position is $-26\,\mathrm{mm}$ from the centre of the trap. Only the trajectory with an initial velocity of $60\,\mathrm{m/s}$ is not trapped. The capture velocity for this setup is $55.7\,\mathrm{m/s}$.

Numerical estimation of the capture velocity is done using a shooting method. By calculating the first position at which a trajectory has a velocity of zero, or if the trajectory leaves the trapping region, we can use an interval bisection method to iterate the initial velocity to find v_c.

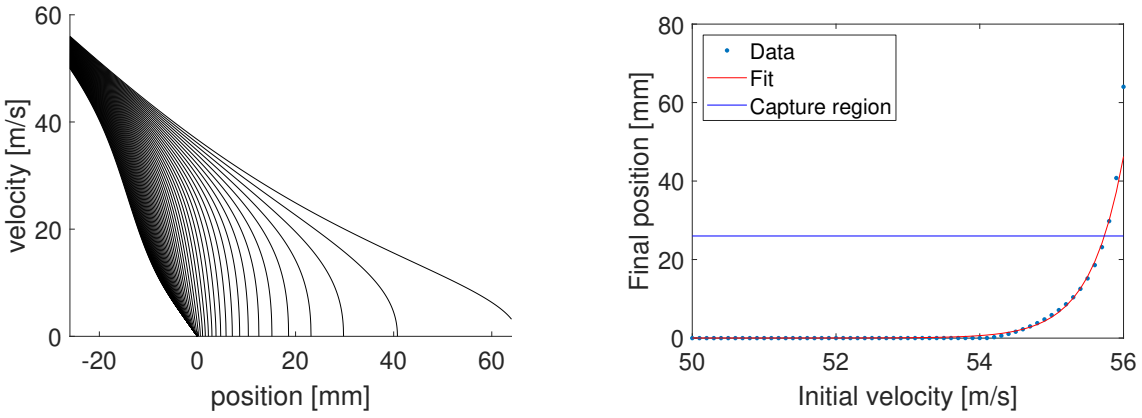

(a) (b)

Figure 2.8: (a) Shows the trajectories for atoms whose velocity is close to the critical velocity. The simulation stops when the velocity is zero or the time exceeds the allowed run-time. The trapping region is ±26 mm Only the last point exceeded the set time for the simulation. The trajectories continue into the negative velocities, this is not shown on the plot as these trajectories are trapped. (b) Shows the position at which an atom, for a given initial velocity, reaches zero velocity. The blue line indicates the boundary of the trapping region. The area below the line is within the trapping region. Any atom that reaches zero velocity before exiting the trapping region is trapped. The final position as a function of initial velocity can be fitted to an exponential allowing for an estimate of the capture velocity to be calculated.

In figure (2.8b) we show that the final position is very sensitive to initial conditions once the atoms have enough velocity to pass through the centre of the trap. The exponential fit is not perfect which suggests either some numerical errors or some real deviation of the system from an exponential behaviour.

2.2.3 Loading rate

In our experiments using the MOT, the atoms are cooled and captured from a hot background gas. In other experiments, a 2d MOT is used to pre-cool the atoms before the atoms are pushed into the trap. The rate at which the atoms are captured, along with other loss rates that we will go into more detail in this section define the steady-state atom number in the trap. The number of atoms in a MOT changes according to the differential equation [Steane et al., 1992],

$$\dot{N} = R - \gamma N - \beta \frac{N^2}{V}. \tag{2.49}$$

This equation can be understood as a constant loading rate from the background

vapour R competing with the two-loss rates, first, γ is the loss due to collisions with the hot background vapour. This is a two-body loss rate depends on the background pressure of the chamber and the number of atoms in the trap. The second loss rate term $\beta N^2/V$ is due to light assisted collisional losses. Here β is the light loss rate and V is the volume of the atom trap. The light loss is caused by an atom re-emitting a photon that is absorbed by a second atom. The second atom can gain enough energy from this collision to leave the trap. This loss rate is a so call three-body loss rate as it relies on three elements interacting. For a more in-depth look into cold collisions, the reader can read [Weiner et al., 1999]. For a MOT containing more than 10^6 atoms the average density $\bar{n}$ becomes constant [Overstreet et al., 2005] therefore we can re-write the equation (2.49) as,

$$\dot{N} = R - N(\gamma + \beta\bar{n}). \tag{2.50}$$

Assuming $N(0) = 0$ so that the trap starts empty, the differential equation can be solved to give

$$N = R\tau(1 - e^{-t/\tau}), \tag{2.51}$$

where the characteristic time τ equals

$$\tau = 1/(\gamma + \beta\bar{n}). \tag{2.52}$$

The characteristic time is the average time an atom spends in the MOT. The loading rate and loss rates determine the steady-state atom number in the MOT. This will become more important when considering the two colour MOT and why the two colour MOT can support a larger atom number. Measuring γ and β directly is usually done by turning off the repump laser and measuring the decay in atom number [Marcassa et al., 1993]. The atom number in the MOT then decays, the characteristic time of this decay will change from quadratic to linear. In our experiment, we can not turn off the background pressure so suddenly but we will show that β can be measured using the two colour MOT.

2.3 Phase space density

The phase space density is a measure of the number of atoms within the thermal wavelength and is an important parameter when it comes to Bose-Einstein condensation.
The wavelength of a thermal atom is given by [Proukakis et al., 2017],

$$\lambda_T = \left(\frac{2\pi\hbar^2}{mk_bT}\right)^{\frac{1}{2}}. \tag{2.53}$$

Phase space density is then defined as [Townsend et al., 1995],

$$PSD = n_0 \lambda_T^3, \tag{2.54}$$

In a MOT experiment depending on the atomic species, the value of the phase space density is usually on the order of $10^{-5} - 10^{-6}$. The phase space density is limited by both the temperature and the maximum density of atoms in the trap. The density in the MOT is limited by photon re-absorption. This can be limited in a few ways as shown in [Vengalattore et al., 2004, Radwell et al., 2013, Rosi et al., 2018]. This formula will be further used in chapter 6 when looking at the formation of BECs.

Chapter 3

Two-colour theory

3.1 Introduction

The two colour magneto-optical trap (TCMOT) was first demonstrated by Cao Qiang et al in [Qiang et al., 2012]. In this experiment, they took a standard magneto-optical trap setup and added a second cooling beam. This setup led approximately to a three times increase in atom number. We later replicated the experiment and also found an increase in atom number [Gadge, 2018]. To try and optimise the setup we need a theoretical understanding of the TCMOT. We will use the theoretical framework presented in chapter two and apply it to the TCMOT to gain further insight into the underlying mechanisms. In chapter five we will try to use the theory outlined in this chapter to explain the results from the two colour experiment.

3.2 Two colour Magneto-optical trap

We will look at the two colour theory following the steps as outlined in chapter two. To simplify these calculations, we use the same two level model used in chapter two. The energy level diagram for the two level TCMOT is shown below in figure (3.1). We define the difference in frequency between the two beams as,

$$\delta = \omega_1 - \omega_2. \tag{3.1}$$

The mean detuning of the two beams is given by Δ which is the same Δ as in the single colour case.

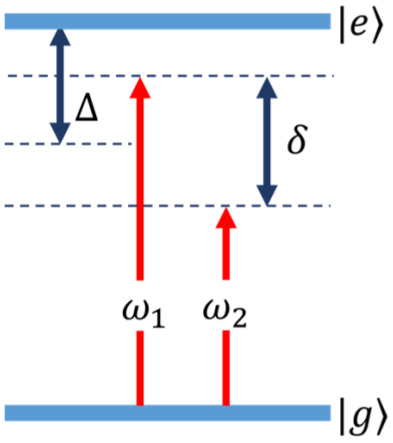

Figure 3.1: The energy level diagram for the TCMOT (not to scale). The ground and excited state and denonted by $|g\rangle$ and $|e\rangle$ respectively. The two frequencies are separated by δ. Δ is the mean detuning of the two beams and is equivalent to detuning Δ in the single colour case in (2.1). The total detuning from resonance for the two cooling beams is $\Delta \pm \delta/2$.

3.3 Equations of motion

In this section, we derive the equations governing the two-level atom in the presence of two light fields. In the first part of the section, we show that there are multiple ways to do the co-ordinate rotation as was done in 2.20. We then choose one of the transformations for the rest of the chapter and show that the choice of transformation does not affect the measurable outcomes such as force and excited-state probability.

3.3.1 Modified Hamiltonian

We begin by adding a second light field to the interaction Hamiltonian and applying the same rotating wave approximation done in (2.15),

$$H_I = -\frac{\hbar\Omega_1}{2}\Big(|e\rangle\langle g|\, e^{-i\omega_1 t} + |g\rangle\langle e|\, e^{i\omega_1 t}\Big) - \frac{\hbar\Omega_2}{2}\Big(|e\rangle\langle g|\, e^{-i\omega_2 t} + |g\rangle\langle e|\, e^{i\omega_2 t}\Big). \tag{3.2}$$

This time the rotating wave approximation removes the two fast rotating terms with a similar frequency. H_I is now the sum of the two laser fields that are interacting with the two-level atom.

We then follow the same procedure in section (2.1.6) to calculate the optical Bloch equations. Starting with the master equation,

$$\frac{d\rho}{dt} = -\frac{i}{\hbar}[\rho, H] + \Gamma D[|e\rangle\langle g|]\rho, \tag{3.3}$$

we then find,

$$\begin{aligned}
\dot{\rho}_{ee} &= -\frac{i}{2}\Big((\Omega_1 e^{-i\omega_1 t} + \Omega_2 e^{-i\omega_2 t})\rho^*_{eg} - (\Omega^*_1 e^{i\omega_1 t} + \Omega^*_2 e^{i\omega_2 t})\rho_{eg}\Big) - \Gamma\rho_{ee} \\
\dot{\rho}_{gg} &= \frac{i}{2}\Big((\Omega_1 e^{-i\omega_1 t} + \Omega_2 e^{-i\omega_2 t})\rho^*_{eg} - (\Omega^*_1 e^{i\omega_1 t} + \Omega^*_2 e^{i\omega_2 t})\rho_{eg}\Big) + \Gamma\rho_{ee} \\
\dot{\rho}_{eg} &= -\left(i\omega_{eg} + \frac{\Gamma}{2}\right) + \frac{i}{2}(\Omega_1 e^{-i\omega_1 t} + \Omega_2 e^{-i\omega_2 t})(\rho_{gg} - \rho_{ee}).
\end{aligned} \tag{3.4}$$

In these equations there are no interaction terms between the two laser beams. We now have two physically sensible choices when it comes to choosing a rotating frame of reference. First, we can rotate with one of the lasers such that

$$\tilde{\rho}_{eg} = \rho_{eg} e^{i\omega_1 t}. \tag{3.5}$$

Which leads to,

$$\dot{w} = \Gamma(1-w) - \frac{i}{2}\Big((\Omega_1 + \Omega_2 e^{i\delta t})\rho^*_{eg} - (\Omega^*_1 + \Omega^*_2 e^{-i\delta t})\rho_{eg}\Big) \tag{3.6a}$$

$$\dot{\tilde{\rho}}_{eg} = (i\Delta - \frac{\Gamma}{2})\rho_{eg} + \frac{iw}{2}(\Omega_1 + \Omega_2 e^{i\delta t}). \tag{3.6b}$$

In this case $\Delta = \omega_1 - \omega_{eg}$. These equations are equivalent to transforming the Rabi frequency such that,

$$\Omega \to \Omega_1 + \Omega_2 e^{i\delta t}. \tag{3.7}$$

Second, we can choose the rotation to be the average of the two laser frequencies

$$\tilde{\rho}_{eg} = \rho_{eg} e^{i(\omega_1+\omega_2)t/2}. \tag{3.8}$$

Which leads to

$$\dot{w} = \Gamma(1-w) - \frac{i}{2}\Big((\Omega_1 e^{-i\delta t/2} + \Omega_2 e^{i\delta t/2})\rho^*_{eg} - (\Omega^*_1 e^{i\delta t/2} + \Omega^*_2 e^{-i\delta t})\rho_{eg}\Big) \tag{3.9a}$$

$$\dot{\tilde{\rho}}_{eg} = (i\Delta - \frac{\Gamma}{2})\rho_{eg} + \frac{iw}{2}(\Omega_1 e^{-i\delta t/2} + \Omega_2 e^{i\delta t/2}). \tag{3.9b}$$

This is equivalent to transforming the Rabi frequency such that,

$$\Omega \to \Omega_1 e^{-i\delta t/2} + \Omega_2 e^{i\delta t/2}. \tag{3.10}$$

Ultimately there is no physical difference between the two cases. Both transformations give the same value for real observable such as the probability of being in the excited state and the force on the atom.

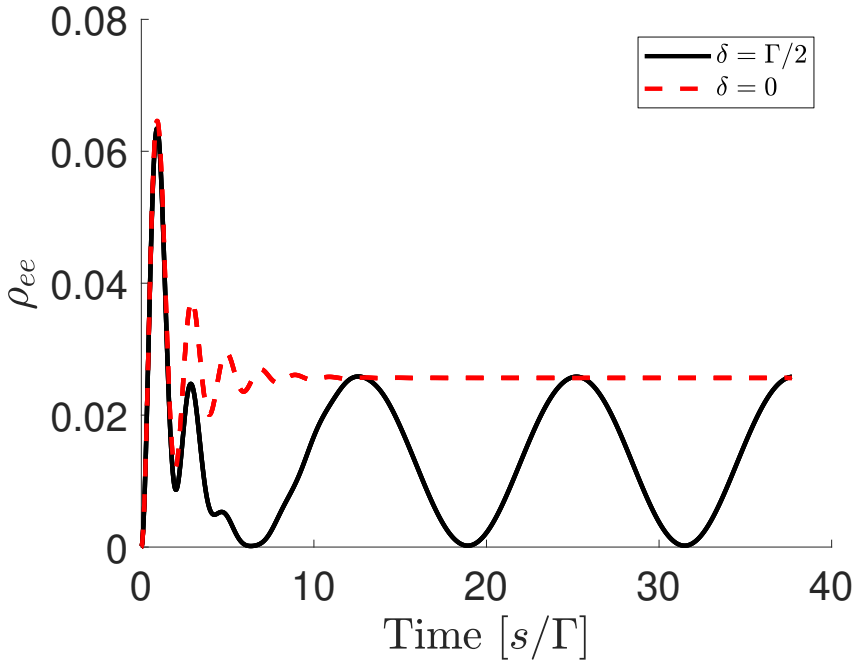

Figure 3.2: Probability of being in the excited state for the single colour light field (blue) and two light fields (black). The two colour solution to ρ_{ee} no longer reaches a steady-state and oscillates at a rate of δ. It is worth noting that the average ρ_{ee} for the two colour case is always lower than that of the single colour case. Here $\Omega_1 = \Omega_2 = \Gamma$ and $\Delta = -3\Gamma$.

Figure (3.2) shows the difference between the two colour and single colour probability of being in the excited state ρ_{ee}. First the ρ_{ee} no longer reaches a steady-state equilibrium but instead, ρ_{eg} oscillates at a rate of δ. The oscillation arises from the modulated intensity due to the beat note between the two cooling beams. When the intensity of the incident light becomes very small the system decays to the ground state, then as the intensity increases, the system is driven into the excited state. Usually, in cold atom experiments, the optical power incident on the atoms is much greater than the saturation intensity of I_s. When the optical power is low, the long term state of ρ_{ee} is approximated using a cosine fit. However, at larger optical powers this approximation breaks down.

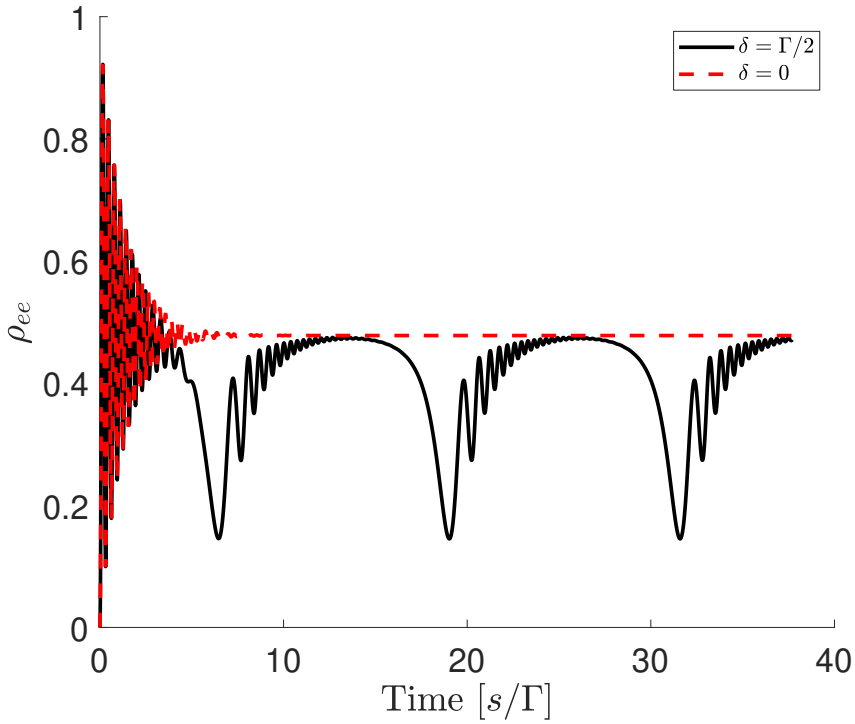

Figure 3.3: Comparison between two colour and single colour with $\Omega = 20\Gamma$ and for the two colour $\Omega_1 = \Omega_2 = \Omega/2$. The cosine approximation has broken down but the period of oscillation has not changed. We see that ρ_{ee} tends towards the limit of $1/2$ with some oscillations which have a frequency of Ω.

In figure (3.3) we can see that the area under the two colour curve is less than that of the single colour. This implies that the atom spends less time in the excited state in the TCMOT. In all these simulations we have assumed that the laser frequency is monochromatic. This approximation leads to some nonphysical results as $\delta \to 0$ there is a discrete step between the average ρ_{ee} in the single colour case and the two colour case. In a real experiment, we expect a smooth transition from the single to the two colour MOT. In the experiment, the laser has a linewidth on the order of 1 kHz. This linewidth would serve to smooth out the transition. Unfortunately, we have not found anything in the literature where the laser linewidth is not treated as monochromatic.

3.3.2 Rotating frame transformation

When deriving the equations that describe the time evolution of the density matrix we made a transformation in equation (2.20) and in (3.5,3.8). The transform applies a rotation to the coherence term of the density matrix ρ_{eg} so that only slowly varying terms remain. In the single colour case, the choice of rotation frequency is obvious. However, in the two colour case the choice of transformation is arbitrary but we need to be sure that our choice

of transform does not affect physical variables such as the probability that the two level atom is in the excited state.

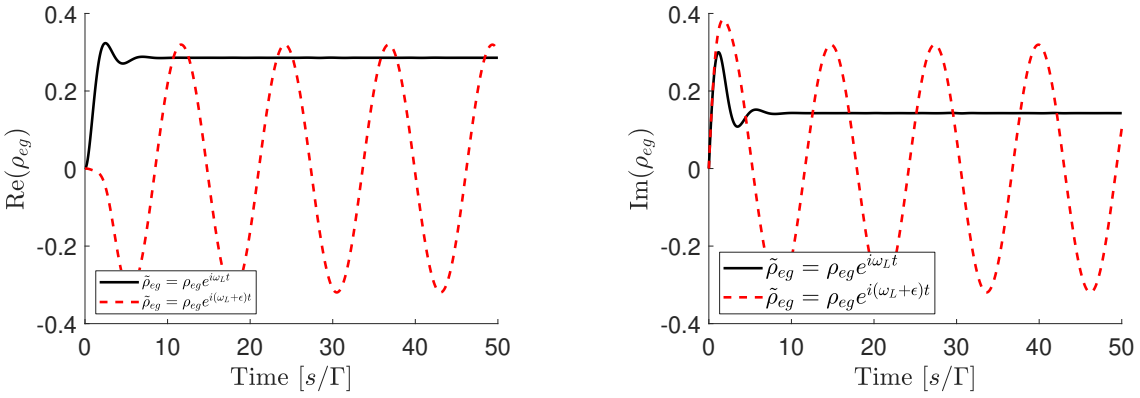

(a) (b)

Figure 3.4: Comparison between two different choices of the rotation. The black curve using the rotation frequency used in (2.20). The red dashed line shows the effect of increasing the frequency of the transformation by a small amount ϵ. With the small change in frequency ρ_{eg} is no longer constant but instead rotates in the complex plane. In this case $\epsilon = \Gamma/2$.(a) and (b) shows the real and imaginary components of ρ_{eg} respectively.

In figures (3.4a) and (3.4b) $\tilde{\rho}_{eg}$ is a stroboscopic measure of ρ_{eg}. While choosing a different frequency for the transform of $\rho_{eg} \to \tilde{\rho}_{eg}$ can lead to an apparent change in ρ_{eg} measurable parameters such as ρ_{ee} should remain unchanged. This is shown in figure 3.4a and 3.5b where we measure ρ_{ee} and the force from the laser respectively. When considering the TCMOT there is no longer a clear choice for the transformation frequency as there are now two intuitive choices for the transformation frequency. These choices are covered in more detail later in the chapter, here we are checking that our choice of transformation does not change the physical result.

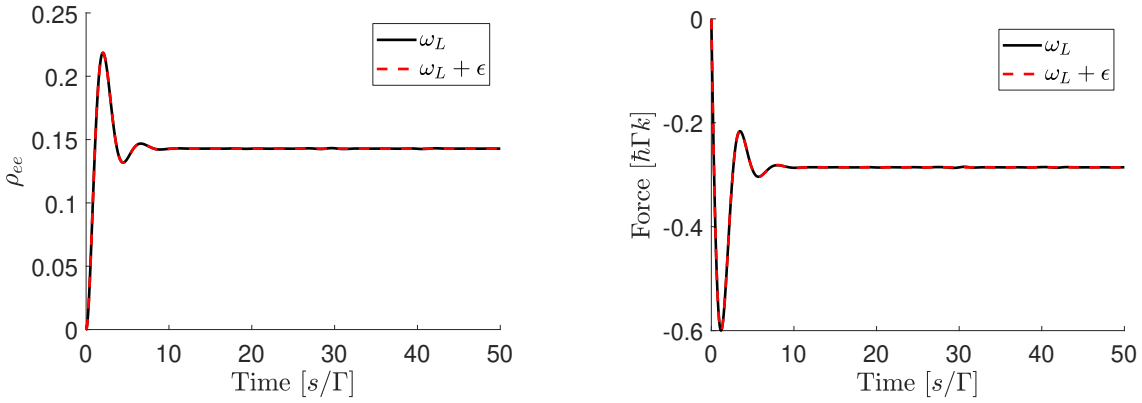

(a) (b)

Figure 3.5: (a) Probability of the two level atom being in the excited state ρ_{ee} for both transforms. (b) Force on the two-level atom for both transforms. There is no difference between the two choices of rotation rate. Note the legend indicates which transform was used for each line.

Here, as expected, we have shown that the frequency of the co-ordinate transformation does not effect physical parameters of the system. This is an obvious result but needed to be checked for completeness.

3.4 Force in 1d

With a numerical solution for $\tilde{\rho}_{eg}$ we can now calculate the force on the atom in 1d. As $\tilde{\rho}_{eg}$ no longer reaches a steady-state, we have yet to find an analytic expression for $\tilde{\rho}_{eg}$. We follow the method outlined in (2.1.8) remembering that Ω has been redefined in equation (3.10). Also that the density matrix ρ no longer has a steady state.

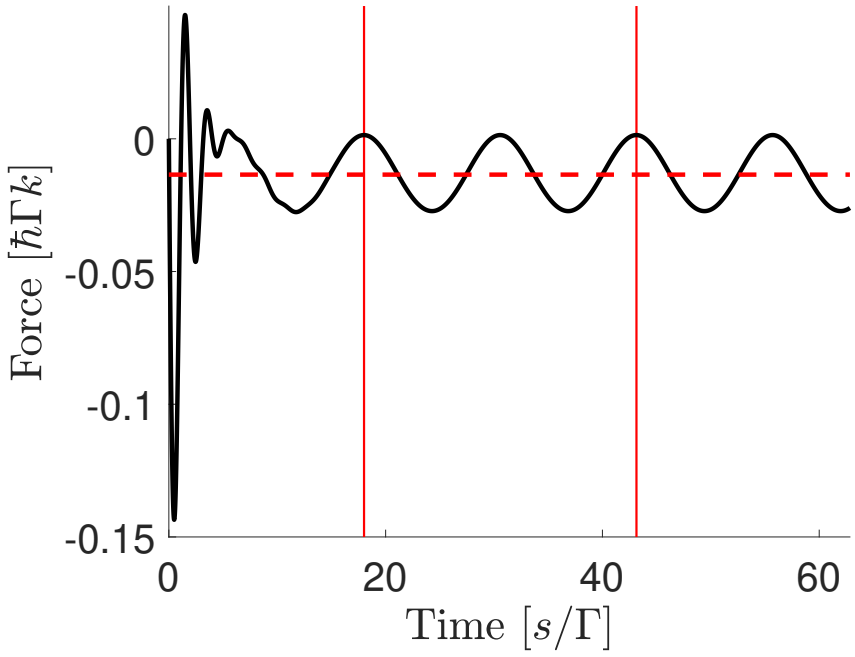

Figure 3.6: Force on the two-level atom that is at rest from one light field pushing the atom in the negative x-direction. The force was calculated using 2.38 and 3.9. The force oscillates at a rate of δ. It is worth noting that the force periodically becomes positive. A positive force means that the light field becomes attractive. Intuitively this seems impossible as from a quantum perspective this would indicate photons with negative momentum. The average of the force, which is measured between the two red lines to capture two full oscillations is non-zero, as shown by the red dotted line. In this plot $\delta = \Gamma/2$, $\Delta = -3\Gamma$ and each beam has equal power with $\Omega = \Gamma$.

Here we see that the force on the atom oscillates with a non-zero average force. However, the force does at times become positive. On the timescale at which the atoms move the force will undergo many oscillations, We can, therefore, average the force over many cycles. Again following the example set in section (2.2.1) we can now add in the velocity and position dependence to the equations by modifying the Δ giving,

$$\Delta = \Delta \pm v \cdot k \mp \mu' B. \tag{3.11}$$

We can now compare force-velocity curves between single and two colour in one dimension as we did in figure (2.5).

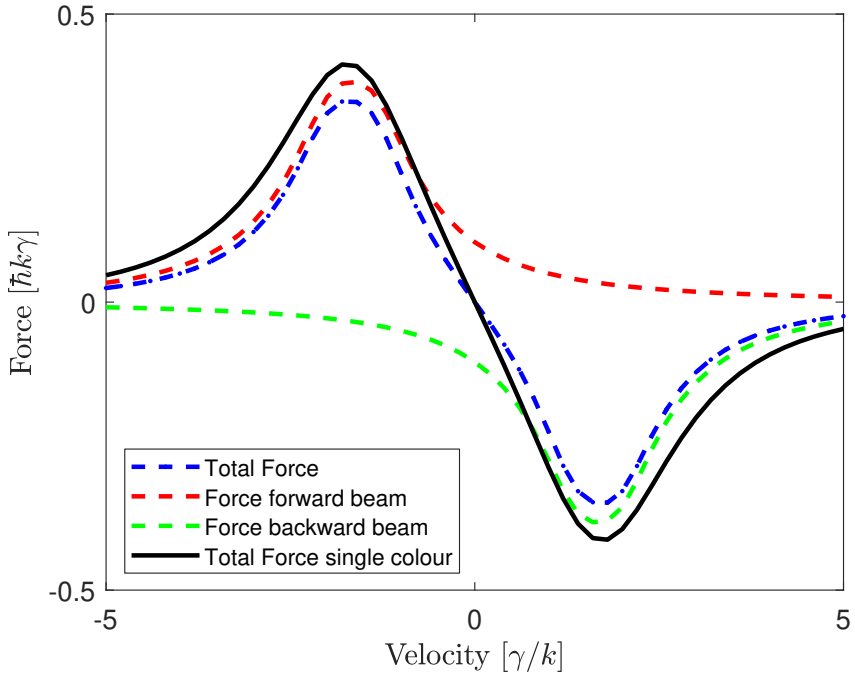

Figure 3.7: Force vs velocity, for the two colour case the force is time-averaged over several periods. The two colour curve is taken at $\delta = 3\,\text{MHz}$. The two colour force is lower at all points than the single colour force. The gradient of the force for small v has decreased in the two colour case. This gradient is a measure of α the damping rate in the MOT. The peak force in the two colour case is at the same location as the single colour as δ is to small for the peak to split.

In figure (3.7) we find that the force is lower at all velocities. For small velocities, the damping rate is given by the gradient of the force around $v = 0$. In figure (3.8) we show how the gradient around $v = 0$ depends on δ.

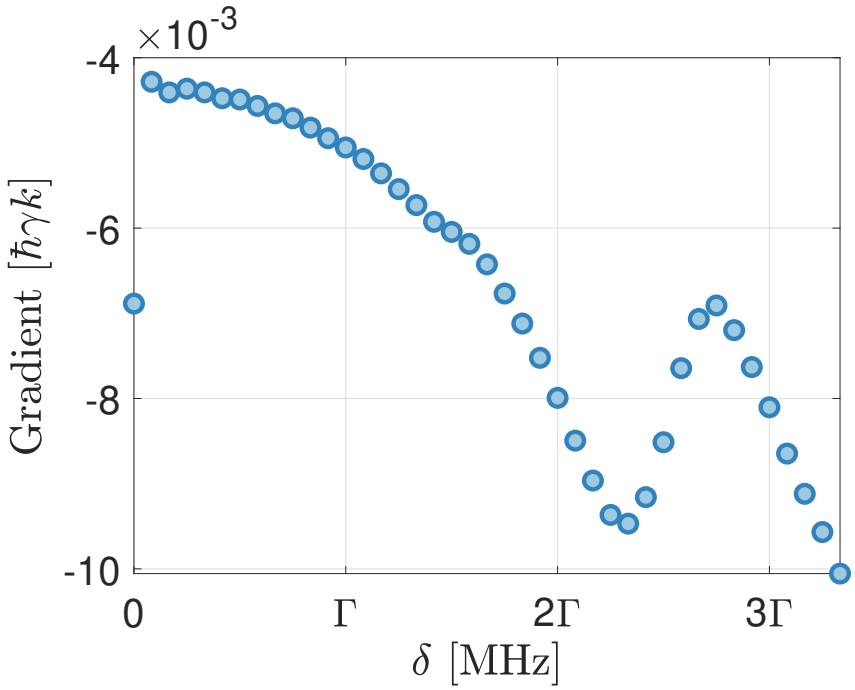

Figure 3.8: Gradient of the force about $v = 0$. as δ increases the gradient returns to a single colour value. There is a small deviation at $\delta = 1\,\text{MHz}$ which could be due to numerical errors. When $\delta > 2\Gamma$ then the behaviour of the system becomes non-monotonic. The discontinuity between $\delta = 0$ and $\delta \neq 0$ is due to the monochromatic nature of the light in the simulation. At $\delta = 0$ there is no beat note reducing the average force on the atom. For any $\delta \neq 0$ there is a beat note that reduces the average force on the atom.

As noted earlier, we find an unrealistic result where the gradient decreases discontinuously between $\delta = 0$ and the first measured value of δ. From section (2.1.9) the lower force implies that the steady-state temperature of a TCMOT will be higher than the single colour MOT. This is due to the reduced cooling rate of α which depends on the gradient of the force for small velocities.

3.4.1 Capture velocity

In section (2.2.2) we showed how the capture velocity could be calculated. Here we will follow the same calculations for the TCMOT. Due to the reduced force from the TCMOT, we have predicted a lower capture velocity for the TCMOT than the single colour MOT.

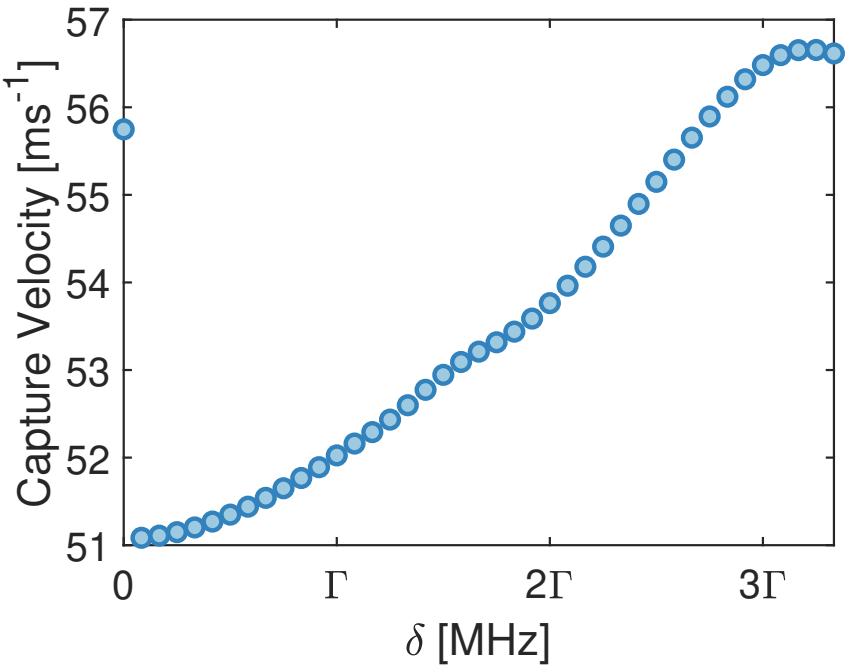

Figure 3.9: Capture velocity as a function of δ. At larger values of δ the capture velocity does not change as rapidly as was shown in figure (3.8). It is interesting to note that the capture velocity becomes larger than the single colour case at large δ. Here $\Omega_1 = \Omega_2 = \Gamma/2$ and $\Delta = -3\Gamma$. The discontinuity is due to the monochromatic nature of the light used in the calculations. When $\delta \neq 0$ there is a beat note that reduces the magnitude of the average force on the atom.

Again we see the same drop in capture velocity as we saw in the gradient of the force. Looking ahead to the results in chapter 5, we know that the peak atom number and minimum force for the two colour MOT occur at $\delta \simeq \Gamma/2$. None of the simulations done in this chapter can predict why the minimum occurs where it does. This could be due to the simulation not including the linewidth, or it could be due to another underlying factor that we have not simulated.

3.5 Conclusion

In this chapter, we derived the optical Bloch equations for a two-level atom with two incident light fields with a relatively small difference in frequency δ. To derive the equations we followed the same steps shown in chapter two. We found that with two frequencies the optical Bloch equations no longer reached a steady-state and instead oscillates with a frequency δ. We then went on to explore how the measurable variable ρ_{ee} changes with different parameters such as beam power and δ. We then used the optical Bloch

equations to calculate the scattering rate and force on an atom from the incident laser light. We found an un-intuitive result that the force from a single beam can become negative, and therefore attracting the atom towards the laser beam. The time-averaged force was still calculated to be repulsive. This change in the force on the atom leads to several predictions of the effect of the two light fields on the MOT. These changes are, an increase in the volume of the MOT due to a reduction in trap stiffness, an increase in temperature of the MOT due to the reduced damping co-efficient also increases the size of the MOT. The capture velocity decreases due to a range of different effects. We will use these predictions to direct the experimental investigations in chapter five.

Chapter 4

Experimental set up

In the previous chapters, we have discussed magneto-optical traps (MOT) in great depth. In this section, we will look at the necessary experimental apparatus for creating a MOT. As the setup used to generate a magneto-optical trap is complex we will break it down into subsections and address each section in turn. The equipment used in these experiments is highly sensitive to environmental factors such as temperature changes and vibrations. To minimise vibrations effects the experiment is mounted on an optical table. An optical table is a standard piece of equipment for many experiments involving free-space optical elements. The optical table has pneumatic legs to dampen vibrations and equally-spaced threaded holes so that experimental equipment can be clamped to the table. The lab is also air-conditioned to maintain the temperature inside the laboratory. The experiment is physically separated into two sections on the optics table, at one end there are the optics which are used to prepare the laser light before the laser light is sent to the other end of the optics table to the vacuum chamber via optical fibres. The experiments require ultra-high vacuum (10^{-10}mbar to 10^{-11}mbar which corresponds to a mean free path of 10^{6}m [Berman, 2014] so that the majority of atoms pass through the chamber without interacting with another atom.

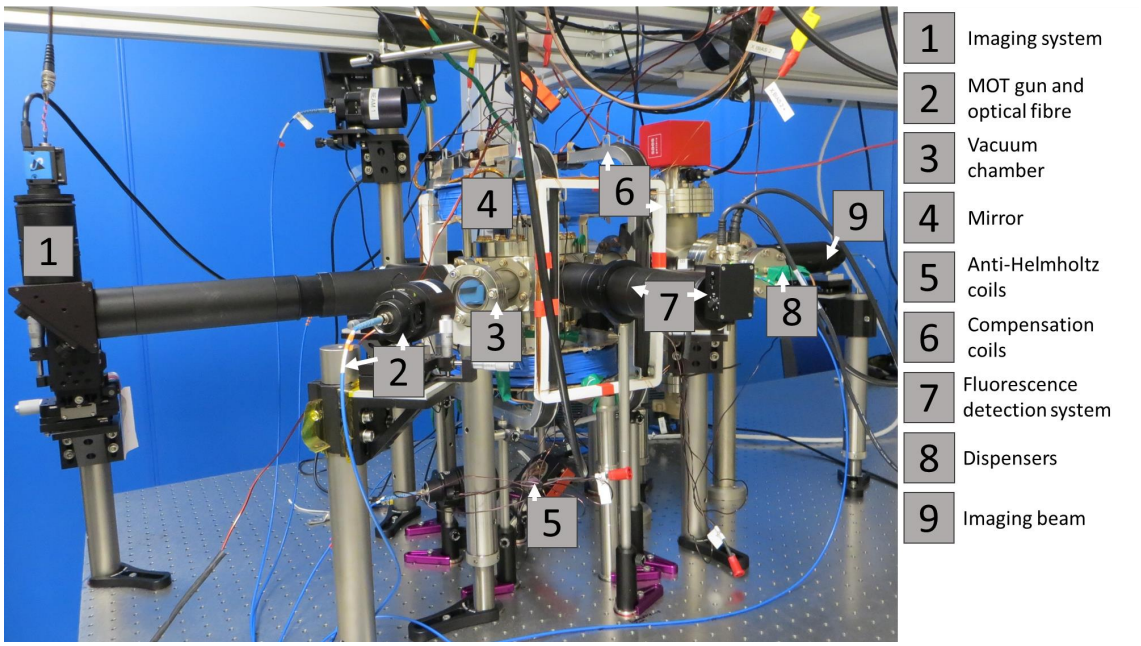

Figure 4.1: An image of our experimental setup with major components labelled.

Here we will give a brief overview of what each component is shown in 4.1 does. In this chapter, we will go more in-depth into most parts listed here.

1. The imaging system uses two lenses with a magnification of ∼0.25 and a focal point 15 cm from the centre of the vacuum chamber. The light is collected by a camera and the images are sent to a computer for processing.

2. The optical fibre brings light from the laser to the atoms. The MOT gun serves three purposes. First, it circularly polarises the laser light, second, the MOT gun expands the light from the fibre to a 2-inch diameter and finally, it collimates the light from the optical fibre.

3. The vacuum chamber isolates the atoms from the environment and allows an ultra-high vacuum to be maintained.

4. The mirror is at 45 degrees so that it gives better optical access for the vertical MOT guns and means the MOT guns can be mounted horizontally.

5. The anti-Helmholtz coils generate a linear magnetic gradient that is used to trap the atoms in the magneto-optical trap.

6. Compensation coils are used to cancel out the external magnetic fields inside the vacuum chamber.

7. The fluorescence detection system is used to capture light from the magneto-optical trap.

8. The dispensers are used to inject rubidium into the vacuum chamber.

9. The imaging MOT gun shines weak on resonance light onto the atoms during absorption imaging. The imaging light is aligned with the centre of the atom cloud and the imaging system.

Figure (4.1) shows the vacuum side of the experimental setup. The optical setup is covered later in this chapter in section (4.1.3).

4.1 Laser systems

In chapter two we looked at how laser light is used to cool a two-level atom. In the experiment, we use ^{87}Rb as it has one outer electron which gives an energy level structure that is similar to the two-level atom. However, there are extra complexities that arise from interactions with the atomic nucleus. The energy level structure of ^{87}Rb is shown in figure (4.2).

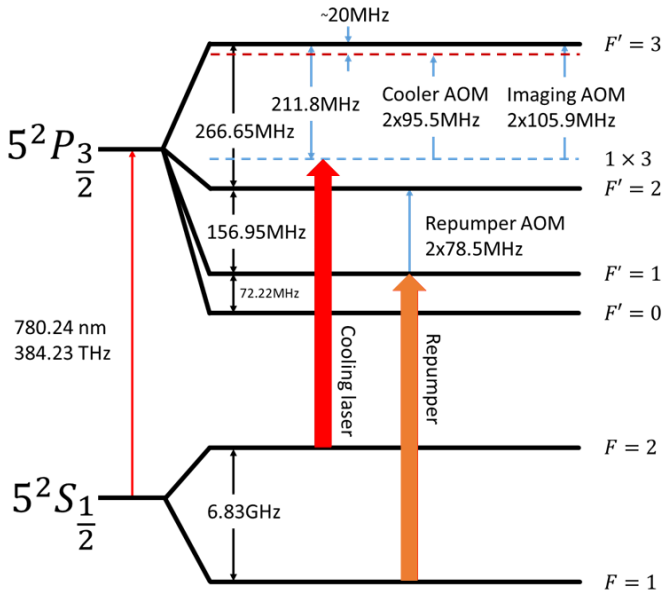

Figure 4.2: Energy level scheme for ^{87}Rb D2 line [Steck, 2001]. The cooling light is locked to the 1×3 peak. The frequency of the cooling light is then increased by 191 MHz to be 20 MHz red detuned from the $F' = 3$ energy level. The frequency of the imaging light is increased by 211.8 MHz to be on resonance with the $F' = 3$ energy level. The repumper light is locked to the $F' = 1$ peak, the frequency is then shifted up by 157 MHz to the $F' = 2$ energy level.

We use the $F = 2 \rightarrow F' = 3$ transition to cool the atoms, and this transition is therefore named the cooling transition. There is a small chance for the atom will be excited in the $F = 2 \rightarrow F' = 2$. In this state, the electron can decay back into the $F = 1$ state where it can no longer be addressed by the cooling laser. Due to the lack of interaction with the cooling light this state is called a dark state. Whilst the rate at which atoms fall into the dark state is low the rate is still high enough that it needs to be compensated for. To move the atoms out of the dark state we use a second light source. The repump light excites the atoms from the $F = 1 \rightarrow F' = 2$ state where the atoms can spontaneously decay back into the $F = 2$ state.

4.1.1 Laser locking

The laser light for the experiment is generated by a pair of TApro lasers from Toptica in a separate laser lab. These lasers can output 3 W and have a frequency range of 660 nm to 1495 nm. The cooling laser is locked to the 1×3 peak and the repumper laser is locked to the $F' = 1$ peak. The repumper and cooling light is coupled into separate optical

fibres which take the laser light to the experimental setup. Approximately 80 mW of repumper light is sent to the lab which is sufficient to meet the power requirements of the experiment. The laser lab cannot provide enough cooling light for the experiment, using a Toptica BoosTA pro the 30 mW of cooling light from the laser lab is amplified to 2.6 W and maintains the frequency of the seed light.

4.1.2 Acoustic optical modulators

To be able to perform an ultra-cold atom experiment we need to be able to finely control the frequency of the lasers. The frequency of the light is controlled using an acoustic-optical modulator (AOM). The AOM is comprised of a crystal and a resonator that creates a standing wave in the AOM crystal. The standing wave acts as a diffraction grating that can increase or decrease the frequency of light passing through the crystal depending on the order of diffraction [Donley et al., 2005]. The frequency of the standing wave is controlled by a radio frequency (RF) input to the AOM. The efficiency of the AOM can be controlled by the power of the RF and the angle of the AOM to the incident light. The AOM in the experiment is set up in a double pass scheme so that changing the frequency of the AOM does not change the position of the beam. A description of the general set up and usage of an AOM can be found in [Donley et al., 2005] [McCarron, 2007]. The AOM also acts as a fast switch that stops the laser light from reaching the experiment. In the two colour experiment, we want to maximise the frequency range over which the AOM efficiency remains constant. We found that to maximise the range over which the power remains constant we needed to minimise the cable that connects the AOM to the RF driver. This is due to impedance miss matches between the cable and the AOM [Stutzman and Thiele, 2012].

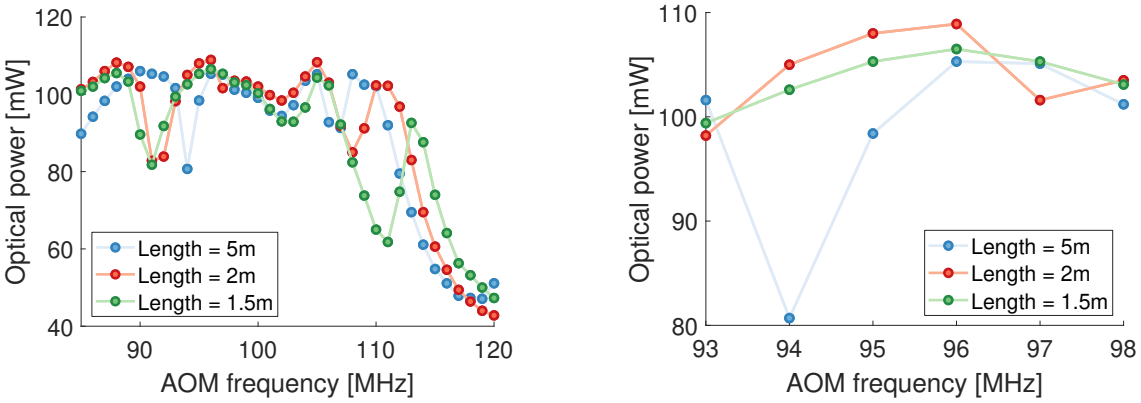

(a) (b)

Figure 4.3: (a) Optical power after a single pass through the AOM. There are two drops in power one around 90 MHz and 105 MHz. The distance between the drops in power increases as the RF cable length is decreased. (b) Close up of the range used in the two colour experiment. The short cable has the smallest change in power over the frequency range.

Figure (4.3a) shows how the efficiency of the AOM changes with frequency. The efficiency is calculated by measuring the power in the laser light before and after the AOM. The AOM was optimised for 95.5 MHz. There are sharp drops in power that move further apart in frequency space when the cable length is shortened due to a miss-match in impedance between the AOM driver, cable and AOM.

4.1.3 Optical layout

The experimental setup we use a six beam MOT. In this configuration, three pairs of counter-propagating beams of light are made to overlap in the centre of the chamber. Each beam of light has the same optical power and is circularly polarised. To get the six beams of light with equal powers and control the frequency of the laser light we use a collection of optical elements outlined in figure (4.4).

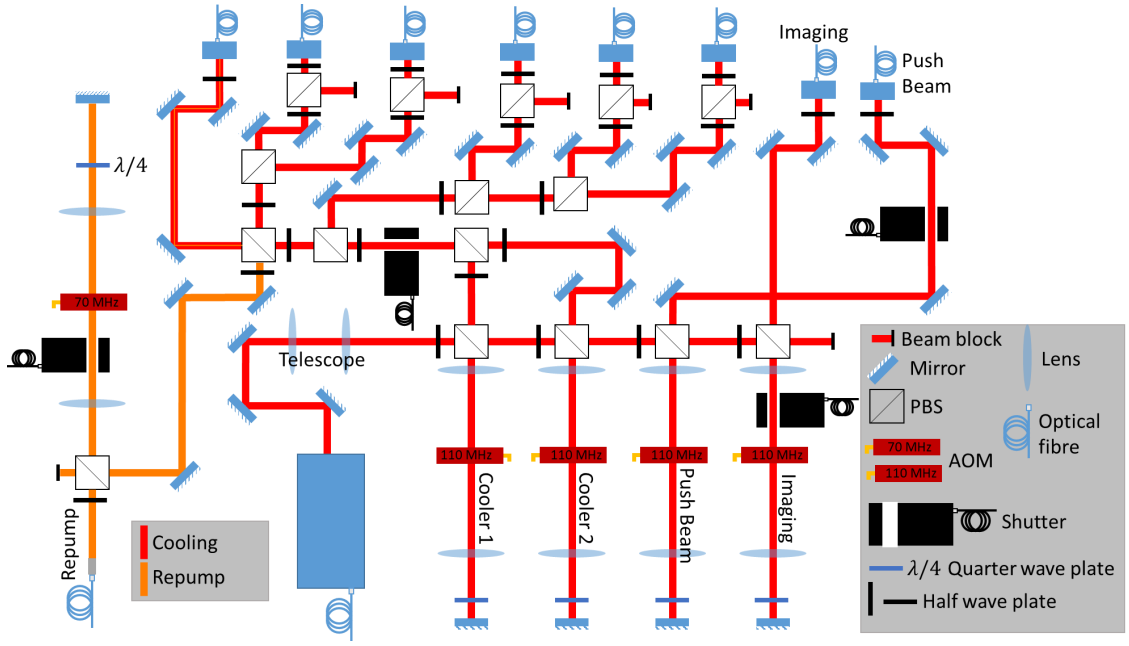

Figure 4.4: Optical layout for the two colour experiment. The laser light from the BoosTA is split into four AOM lines using polarising beam splitter cubes. The light from cooler one and cooler two are first mixed and then separated into 6 optical fibres. The push beam and imaging beams are coupled into separate fibres. The imaging AOM is kept off during the MOT loading due to changes in AOM efficiency when the AOM is warming up. Due to this the shutter is placed before the imaging AOM rather than after as is the case for the other beams. The repump light, the orange line is coupled into the far left fibre coupler with orthogonal polarisation to the cooling light.

The repumper frequency is shifted by an AOM from $F' = 1$ to $F' = 2$. The repumper light is then coupled into the left-most optical fibre along with the cooling light. The cooling light (red) from the laser lab is coupled into the BoosTA where the light is amplified to 2.6 W. The intensity profile of the BoosTA has multiple lobes and is difficult to get good fibre coupling efficiency with such an intensity profile. The telescope is used to reshape the light from the BoosTA to be more circular. The laser light from the BoosTA is split into 4 sections by half-wave plates and polarising beam splitter cubes. The majority of the power goes into cooler 1 and cooler 2. A small amount of optical power (> 1 mW goes to the imaging beam and push beam. The push beam is used to measure the forces on the MOT as explained in section (5.3.2). Excess power is absorbed by a high power beam dump at the end of the line of polarising beam splitter cubes. Cooler 1 and cooler 2 are combined with polarising beam splitter cubes shown in fig (4.5).

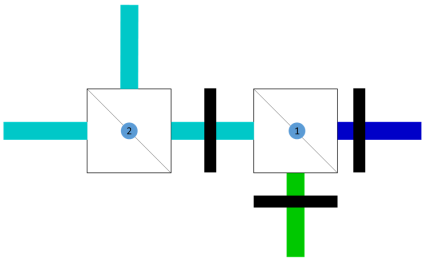

Figure 4.5: Close up on the setup to mix the two cooling lasers. Cooling laser 1 (Green) and cooling laser (2) is spatially overlapped at cube 1. The outputs at cube 2 have equal power and equal polarisation for each cooling beam. The black lines indicate half-wave plates used to control the polarisation of the beams.

The two cooling beams of light are equally split into six paths and coupled into optical fibres. Before the optical fibres, we placed a PBS to clean up the incoming polarisation. Adding the polarisation cleaning cube can not be done in beam one due to the repumper having orthogonal polarisation to the cooling lasers, a PBS here would reflect the repumper light rather than transmit the repumper light and so stop the repumper light from reaching the atoms. A half-wave plate is used to align the polarisation of the laser light to the fast axis of the optical fibre. This minimises the polarisation fluctuations caused by stress in the fibre.

To get an accurate measure for the time of flight, we need to be able to quickly turn the lasers off. Whilst the timing is controlled by a computer the physical act of turning the laser off combines two methods. First, the AOM can be turned off so that all the optical power is in the 0^{th} order where light is then blocked. The switching time of the AOM is on the order of ns, however, a small amount of light can leak through the AOM and reach the experiment. To completely block the light we use a shutter which can be triggered remotely. There is a delay of a several ms between when the shutter receives a signal and when the shutter is fully open or closed. This delay is on the order of 10 ms and can vary depending on the direction of the shutter if it is opening or shutting. These delays are incorporated into the control system to minimise the time delay. Combining these two methods we gain both fast switching of the laser light and a high extinction of the laser light.

Before the laser light enters the chamber the light is first passed through a 'MOT gun' [Gadge, 2018]. This comprises of a series of optical elements. First, the light is circularly polarised with a quarter-wave plate, then the light is expanded and collimated. The exact

profile of the light from the MOT gun depends on the precise alignment of optical elements. The average $1/e^2$ of the MOT guns used for cooling is 25.7 mm.

4.2 Imaging

In our experiment we use a combination of fluorescence imaging and absorption imaging. Absorption imaging uses a weak on resonance laser light (imaging light) that is shone on the atom cloud. By measuring the shadow the atoms leave on the intensity profile of the imaging light the size and atom number can be calculated [Reinaudi et al., 2007]. Absorption imaging is a destructive imaging technique as the atom cloud is dispersed during the imaging sequence. For each image, a new cloud needs to be loaded. We perform absorption imaging several ms after the optical and magnetic fields have been turned off so that the optical density of the MOT decreases and the cloud shape becomes more Gaussian which allows for a more accurate estimation of the atom number. Absorption imaging can not be used to do in trap imaging as it requires the atoms to be in the ground state to interact with the imaging light. To measure the size of the atom cloud in the trap we image the fluorescence profile of the atom cloud. In situ imaging of the atoms in the trap. This is done to calculate the density of atoms in the trap which is an important parameter in (5.2). A narrow band filter around 780.2 nm is used to reduce the levels of background light. An alternative imaging method uses phase rotation of light to measure the atom cloud in a magnetic trap in a semi non-destructive manner [Bradley et al., 1997].

4.2.1 Absorption imaging

Absorption imaging uses low power laser light that is resonant with the $F = 2 \rightarrow F' = 3$ transition. The atoms in the atomic cloud absorb the light and re-scatters the light in a random direction. This causes a drop in the intensity of the imaging beam over the size of the atom cloud and the shadow is detected on a CCD camera. Absorption images are taken in the absence of other light fields so that the atoms are in the ground state and will not interact with the imaging light. Absorption images are also usually taken without magnetic fields however the presence of a magnetic field can be accounted for by modifying the atomic scattering rate. Combining the absorption images with reference light and dark image we can calculate the optical density of the atom cloud [Smith et al., 2011].

Images were acquired with an Image source camera (DMK 23U618) which has 640x480 pixels and each pixel is 5.6 µm × 5.6 µm. Each pixel has 8bits of memory so each pixel reads between 0 and 255. reads between 0 and 255. Calibration of the imaging system was

done by fitting the centre of mass of an atom cloud to the parabolic trajectory when falling under gravity. We found the magnification to be 0.259 where we expected a magnification of 0.25.

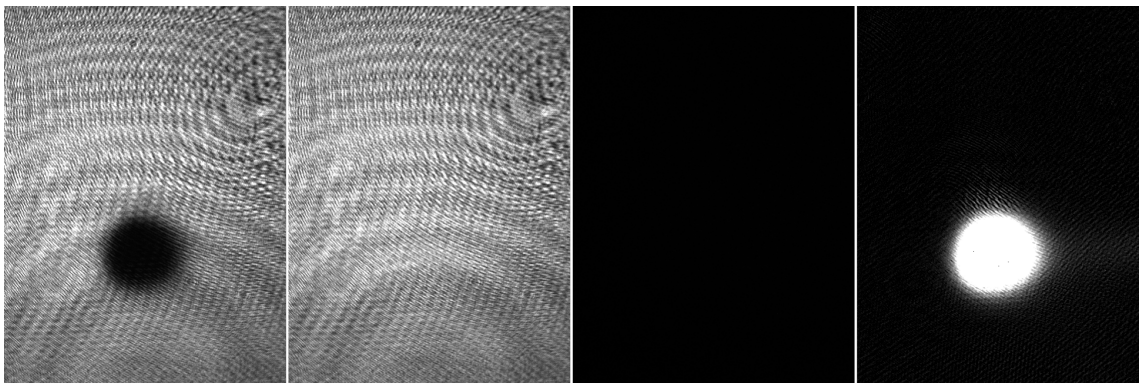

Figure 4.6: (a) Atoms image: Imaging light is absorbed by the atoms causing the dark spot on the image. (b) Light image: The light image is taken to measure the intensity profile of the imaging light. (c) Dark image: This image is taken so that the background light can be subtracted out. (d) Optical density image: This is the final result of an absorption image. By fitting this image to a Gaussian we can estimate the number of atoms in the cloud. Each image is $13.84\,\text{mm} \times 10.38\,\text{mm}$.

In figure (4.7) we scan the frequency of the imaging light and estimate the atom number. Using the measured atom number we can calibrate the frequency of the imaging beam by calculating the frequency at which we find the largest atom number. When the frequency of the imaging beam is on resonance with the $F = 2 \rightarrow F' = 3$ transition the atoms will maximally scatter the light (see section 2). This can also be used to measure the linewidth of the $F' = 3$ energy level.

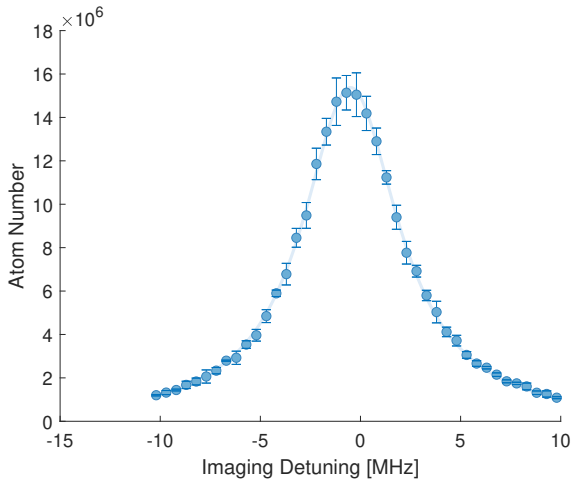

Figure 4.7: Estimated atom number vs the frequency of the imaging light. The blue line is a fit of a Lorentz profile with a linewidth of 5.9 MHz. The frequency of the imaging AOM was set to where the observed atom number is highest. This corresponds to a frequency of 106.5 MHz

4.2.2 Temperature

An important property of an atomic cloud is the temperature of the atoms. To measure the temperature of the atom cloud we remove the trapping fields. The atom cloud falls under gravity and expands ballistically. By fitting the optical density profile of the cloud to a 2d Gaussian function the size of the atom cloud can be calculated.

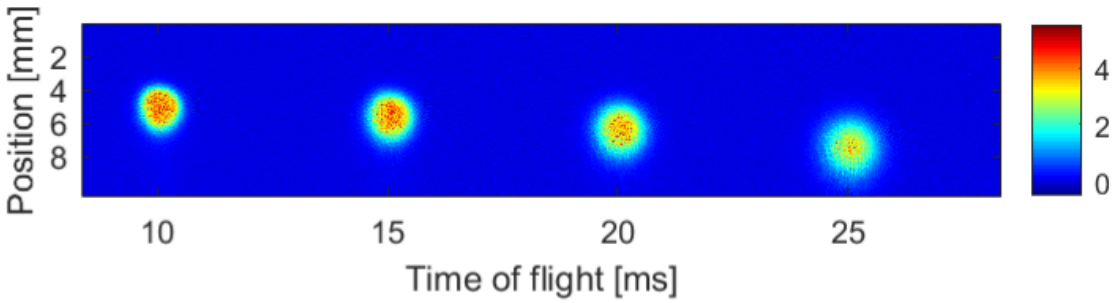

Figure 4.8: Optical density images of atoms in free fall. The centre of mass of the atoms follows a parabolic trajectory as the atoms accelerate under gravity. The atom cloud expands and becomes less dense as the time of flight increase. This atom cloud has an average temperature of 13.4 µK. The colour bar denotes the magnitude of the optical density.

The expansion of the cloud can be described by a convolution of the atoms momentum

and initial position. The size of the atom cloud after a time of flight t is given by

$$\sigma(t)^2 = \sqrt{\sigma_0^2 + \frac{k_B T}{m} t^2}. \tag{4.1}$$

Here $\sigma(t)$ is the size of the atom cloud after expanding for a time t, σ_0 is the initial size of the atom cloud, T is the temperature of the atom cloud, m is the atomic mass and k_B is the Boltzmann constant. By measuring the size of the atom cloud (σ) at a range of time of flights, we can calculate the gradient and therefore the temperature. For a large time of flight, the thermal term begins to dominate over the initial cloud size and the gradient of σ asymptotically approaches $k_B T/m$.

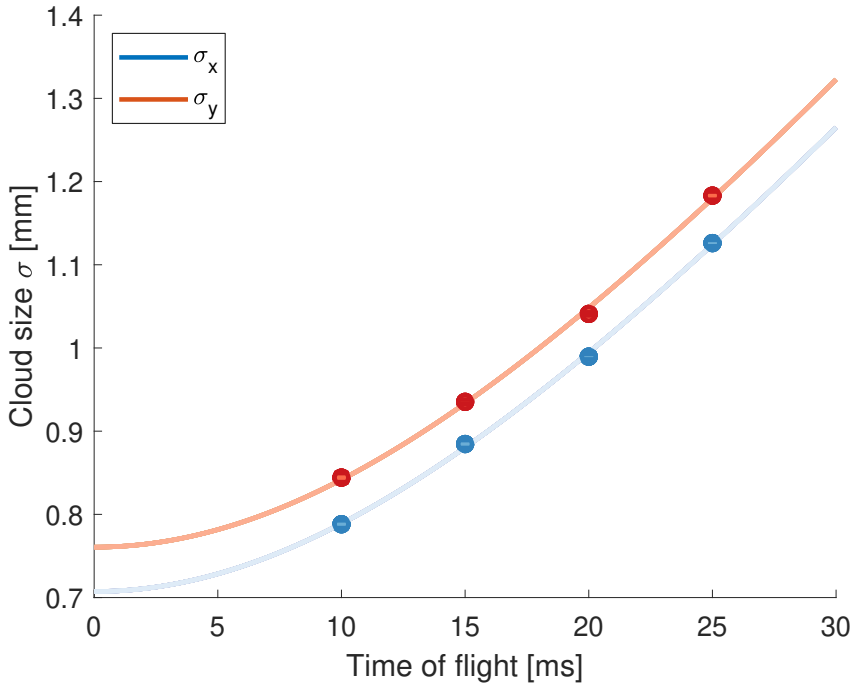

Figure 4.9: The expansion of the atom cloud in time of flight. At early times σ_0 dominates and at later times the expansion of the atom cloud becomes dominant. The temperature was measured to be 12.8 µK in the y-direction and 13.6 µK in the x-direction.

As the atoms are free-falling the maximum time of flight is set by the field of view. The field of view is limited by the windows to the vacuum chamber. In the experiment, the maximum time of flight was ~ 30 ms before the atom cloud became significantly clipped by the field of view.

4.2.3 Fluorescence imaging

In the two colour MOT experiment, we measure the volume and density of the atom cloud. Due to the high temperature of the atom cloud in the two colour MOT (see (5.2.3)

the cloud would expand rapidly when the fields were turned off for absorption imaging. To accurately measure the size of the atom cloud in the trap without measuring the temperature of the MOT we use fluorescence imaging. In fluorescence imaging we collect the light that has been re scattered from the atom cloud. To do this we focus the re-scattered light from the MOT onto a camera or photodetector. The images were taken at the end of the sequence when the atom cloud was fully loaded. Some consideration needs to be given to the scattering rate of the atom cloud between the single colour and two colour MOT when looking at the images as we expect the two colour scattering rate to be reduced by two-colour effects.

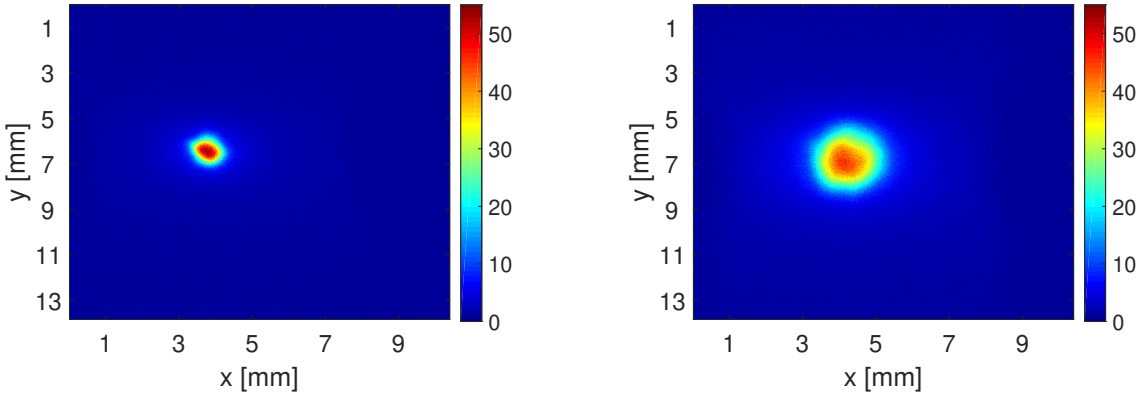

(a) (b)

Figure 4.10: (a) In trap fluorescence image for a single colour MOT (b) In trap fluorescence image for a two-colour MOT at $\delta = 0$. The in trap images give a more accurate value for the size of the atom cloud. The in-trap cloud has a less Gaussian profile that can be detrimental when estimating the volume.

The images in figures (4.10a) and (4.10b) show that the atom cloud has a roughly Gaussian profile with some minor deformities. The fluorescence light was captured for 100 µs, light and dark images were also taken for reference.

4.2.4 Fluorescence detection

Measurement of the fluorescence from the MOT can be done in real-time. This is done by capturing the fluorescence light onto a photo-diode. The photo-diode returns a voltage proportional to the fluorescence. The voltage is then read and displayed by an oscilloscope. The amount of fluorescence is proportional to the number of atoms in the trap [Jooya et al., 2013]. An absorption image is still required to calibrate the output voltage to the atom number.

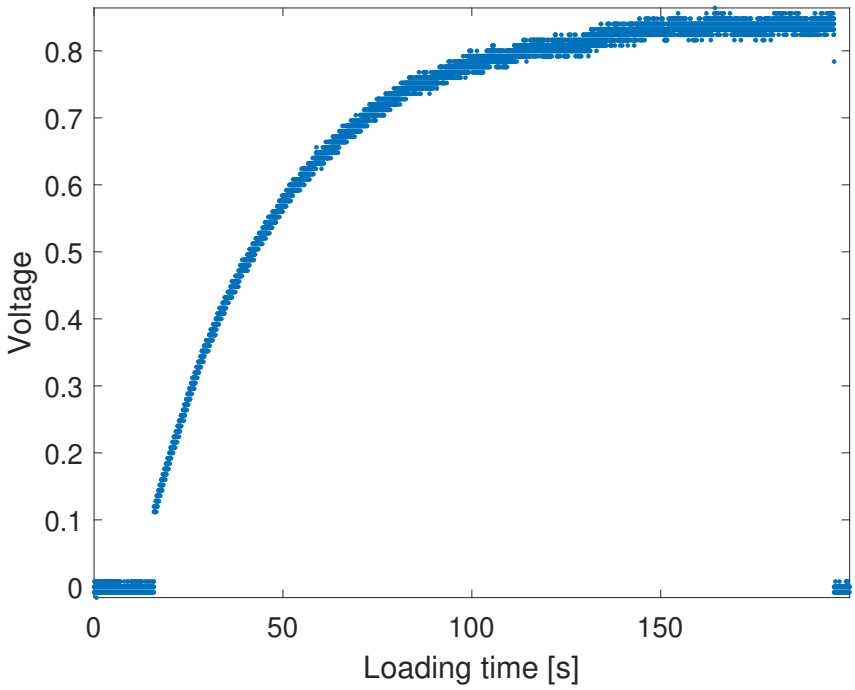

Figure 4.11: Magneto-optical trap loading curve. When the loading sequence beings at $\sim 15\,\mathrm{s}$ the voltage increase suddenly due to the background light. The signal increases in proportion to the number of atoms in the trap. The loading time was 180 s. There is a visible discretisation of the signal due to limitations of the camera.

Figure (4.11), shows the fluorescence as atoms are loaded into the trap. The loading time is 180 s and the atom number in the trap saturates before 180 s. Initially, the lasers are off and the output voltage is just from the background counts. When the light fields are turned on the voltage suddenly increases, this is due to the photo-diode capturing light that is scattered of the vacuum chamber. The voltage then increases proportionally to the atom number following equation (2.49).

4.3 Magnetic fields

As discussed in Chapter 2, the MOT requires a linear magnetic field gradient to apply a position dependant force to the atoms [Phillips, 1998a]. To generate this field we use a pair of coils in an anti-Helmholtz configuration. A complete description of the anti-Helmholtz fields can be found in [Youk, 2005]. The coils used to generate the anti-Helmholtz field are 16 cm apart and generate a gradient of 0.269 G/cm/ampere.

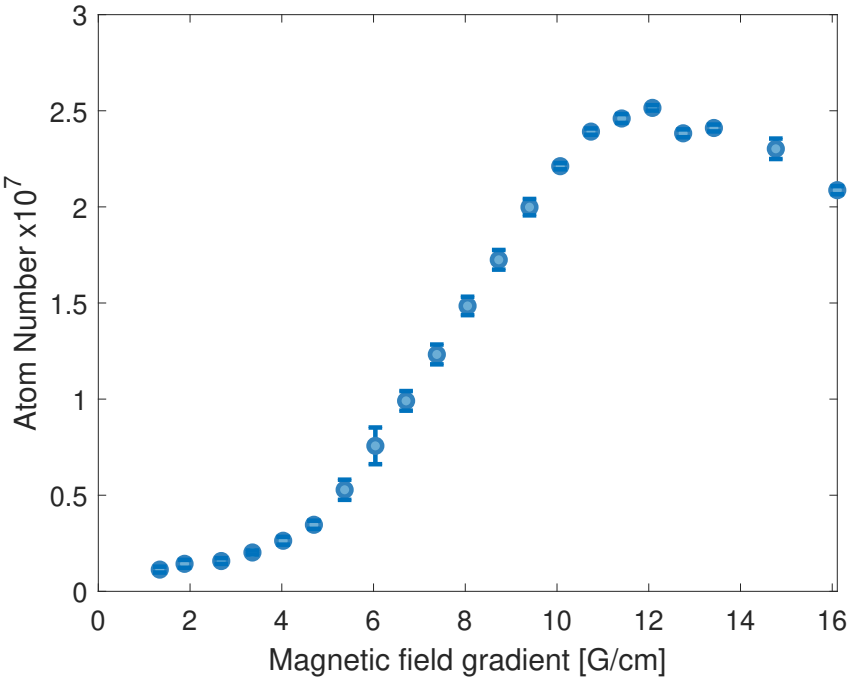

Figure 4.12: Atom number as a function of magnetic field strength. The atom number peaks at 12 G/cm. This corresponds to a current of 44.6 A, at this current the coils would begin heating up. In the two colour experiments we used 35 A which corresponds to 9.4 G/cm.

The laboratory environment is subject to stray magnetic fields. For example, the earth magnetic field ranges from $0.25\,\mathrm{G} - 0.65\,\mathrm{G}$ and the orientation can vary depending on location. These stray magnetic fields can cause the magnetic zero from the anti-Helmholtz to drift from the centre of the vacuum chamber. To offset these external magnetic fields we used 3 pairs of coils in Helmholtz configuration, one pair of coils for each Cartesian axis. A Helmholtz coil generates a uniform constant magnetic in the region between the coils pointing from one coil to the other. We refer to this constant field as a bias field. The magnetic field zero is aligned to the centre of the trapping beams by using the atom cloud. When the trapping field was turned off the atom cloud would expand uniformly as there is no positional trapping. If there was an external field the magnetic field would cause a directional bias of the force on the atoms. This extra force would accelerate the atoms. By tuning the currents in the bias coils we could offset the stray fields so that the atom cloud would expand uniformly.

4.4 Vacuum system

The vacuum chamber is a 6.0" Spherical Octagon from Kimball physics[1]. The vacuum chamber is mounted over the optical table on pillars to give full access to each direction of the vacuum chamber (see fig (4.1)). We used a roughing pump and a turbopump to evacuate the air out of the chamber then we gradually heat the vacuum chamber to $\sim 150\,^{\circ}\mathrm{C}$. This process is called bake out and is done to accelerate the rate at which material is removed from the vacuum chamber walls. The bakeout was done for one and a half weeks after which the chamber was allowed to cool. When the pressure in the vacuum chamber dropped below 1×10^{-8}mbar then the ion pump was turned on. This was done at a temperature of $100\,^{\circ}\mathrm{C}$. The final pressure in the vacuum chamber was 5.5×10^{-10}mbar.

[1] https://www.kimballphysics.com/

Chapter 5

Results of the two-colour magneto-optical trap experiment

5.1 Introduction

The two colour magneto-optical trap (TCMOT) was first demonstrated in [Qiang et al., 2012] where the TCMOT was shown as a method to increase the number of atoms trapped in a MOT. The increase in the number of trapped ultra-cold atoms helps the formation of a Bose-Einstein condensate (BEC) in multiple ways. First, evaporative cooling kicks atoms out of the trap to reduce the temperature of the remaining atoms in the trap [Ketterle and Van Druten, 1996]; a larger starting number of atoms allows for a faster and less efficient ramp to be used. A large atom number of atoms also increases the thermalization rate of the atoms in the trap, which can be beneficial in the long term as often the limiting factor in BEC experiments is the lifetime of the BEC. As we will show in chapter 6 the sensitivity of the BEC microscope is also benefited by a larger number of atoms. To better use the TCMOT as a source of atoms for the BEC-M we first needed to get a better understanding of the properties and underlying mechanisms of the TCMOT.

Here we will present the experimental data in 3 parts: first, we go over the characterisation of the physical properties of the TCMOT as a function of δ, the relative detuning, between the two red lasers. We will then present the results from the so-called push beam experiment which is used to directly measure the forces in the TCMOT. Finally, we will show the results of experiments to allow the TCMOT to be utilised with other cold atom systems. As before in chapter 3 we define,

$$\delta = \omega_1 - \omega_2, \tag{5.1}$$

where ω_1 and ω_2 are the frequencies of the two cooling lasers. It should, therefore, stand that the TCMOT should be the same for δ and $-\delta$. However, due to experimental considerations, this is never exactly the case. The introduction of the second frequency introduces a beat note between the two light fields. The combined laser light has an intensity modulation at a frequency of δ.

5.2 Characterisation of the two colour magneto optical trap

It is necessary to point out that we define two types of "single colour" magneto-optical trap (MOT). First, there is the single colour MOT which has only one cooling frequency. Second is the pseudo-single colour MOT which has two cooling frequencies with a difference of almost zero, however, we have measured a 120KHz difference in frequency the two cooling frequencies. This frequency difference is small when compared to the non zero values of δ so it is ignored. From here on when $\delta = 0\,\text{MHz}$ we are using the pseudo-single colour case.

In these experiments, we choose the average frequency of the two cooling lasers to be $\Delta = -2\pi \times 20\,\text{MHz}$. As it has been shown earlier by [Gadge, 2018], that the atom number peaks for both single and two colour MOTs at $\Delta = -2\pi \times 20\,\text{MHz}$.

5.2.1 Atom Number

The most appealing aspect of the TCMOT and why it has been considered for research is the increase in atom number in the trap. The change in atom number as δ is varied is shown in 5.1.

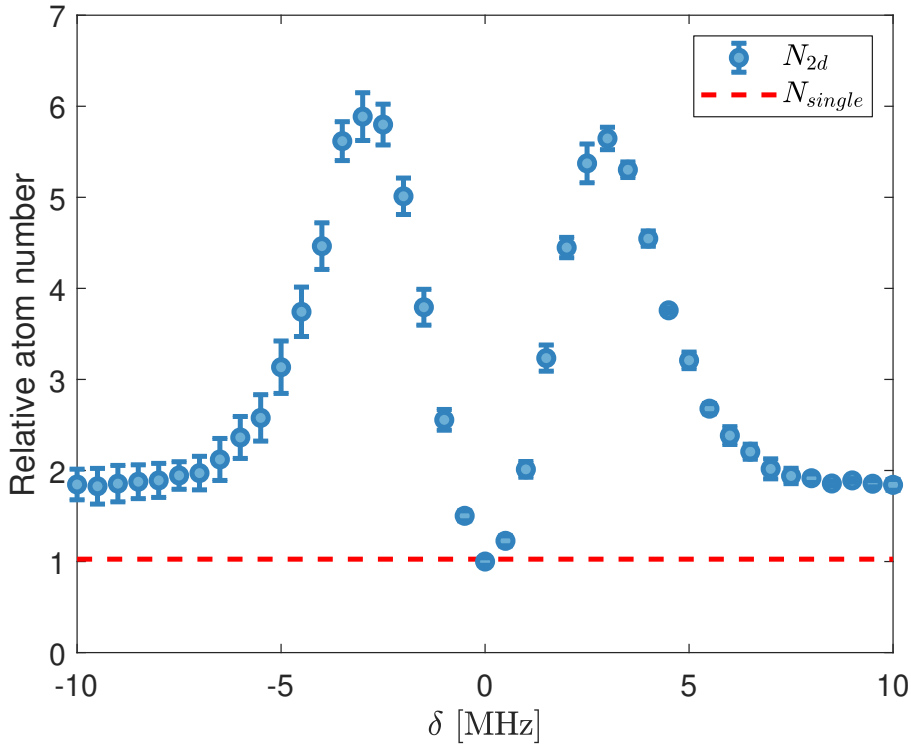

Figure 5.1: Relative atom number as a function of detuning. The atom number has been normalised to the single colour atom number. The atom number peaks at $\pm\Gamma/2 = 3\,\text{MHz}$ and falls to a constant value as $\delta > \Gamma$. The red line indicates the atom number for a true single colour MOT. The maximum atom number was 2.92×10^8. We observe a six times increase in atom number at the optimal two colour detuning.

As shown in 5.1 we find that the peak atom number for the TCMOT is 5.9 times that of the atom number in the pseudo-single MOTs. It is also interesting to note that the TCMOT atom number tends to a constant value at large $|\delta|$. This value is still larger than the pseudo-single MOT atom number. This suggests that the mechanism that increases the atom number in the TCMOT becomes frequency independent as δ becomes larger than Γ. Here Γ is the linewidth of the atomic transition, for $^{87}\text{Rb} = 2\pi \times 6.07\,\text{MHz}$. This will have a limit for very large values of δ. When $\delta \simeq \Delta$ as one of the beams will be on resonance or blue detuned and no longer cool the atoms. The experiment could not reach this limit due to limitations with the acoustic optical modulators (AOMs). In an ideal experiment, we expect the atom number to be symmetrical about 0, however, there are imbalances in atom number and relative position which are caused by two effects. First, if there is an imbalance in the optical power between the cooling lasers then peaks become mismatched in height. Second, there is a slight difference in the frequencies at 0 MHz of 120 kHz this causes a shift of the plot horizontally equal to 120 kHz.

5.2.2 Loading rate

As the final atom number is given by the balance between loading rates and loss rates we measured the loading curves of the TCMOT and found that the loading time of the TCMOT is much longer than that of the single and pseudo-single colour MOTs.

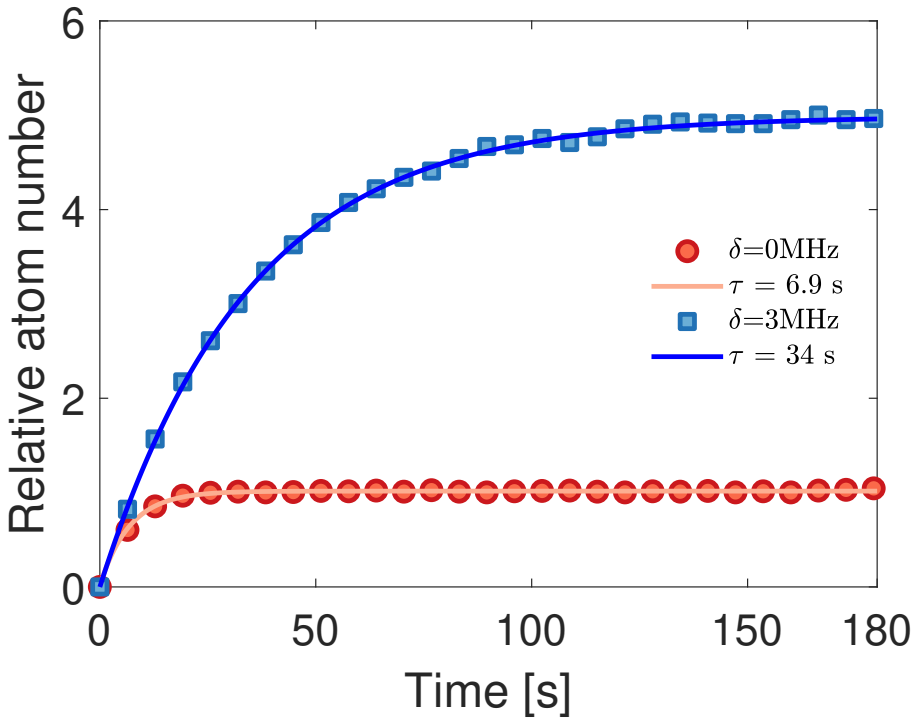

Figure 5.2: Relative loading rate curves for single (red) and two colour (blue) MOTs. The loading curves have been normalised to the final single colour level. The loading times are not normalised. The curves were fit to equation (2.49). In this setup, the loading time of the two colour MOT is 4.9 times longer than the loading time of the single colour MOT. This is proportional to the difference between the number of atoms in each trap.

We can see that in figure (5.2) at long times the atom number reaches a constant value where there is an equal number of atoms entering and leaving the trap. Given the MOT reaches a constant atom number we can re-arrange to give a relation between the number of trapped atoms and the volume of the atomic cloud. Whilst it would be cluttered to show all the loading curves for different values of δ we found that the loading times follow the same trend as the atom number, where the loading time is maximum at $\delta = \pm\Gamma/2$. We can measure the loading rate indirectly by fitting the curves to equation (2.49).

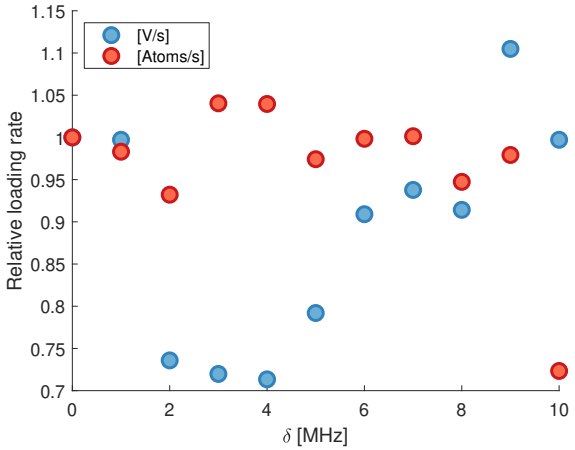

Figure 5.3: Relative loading rates as a function of δ. The blue points are taken from the fluorescence of the MOT and indicate a decrease in the loading rate as the atom number decreases. The red points are normalised to the measured atom number and these points don't exhibit the same decrease in loading rate that the fluorescence. The last point on the plot at $\delta = 10\,\text{MHz}$ seems to be anomalous. This data was taken from one scan of loading rates measured by fluorescence.

Figure (5.3) shows that when normalised by atom number the loading rate remains constant. The decrease in the blue points where the atom number increase indicates that the scattering rate has decreased which is predicted by theory. However, the actual loading rate number of atoms loaded remains constant which goes against the theoretical predictions. In section (2.2.3) we showed that the loading time τ depends on 3 factors. First, the background loss rate γ, remains constant and only depends on the background pressure which depends only on the experimental apparatus. The second mechanism for the loss of atoms from the MOT is the light-induced losses. The light-induced loss rate depends on two parameters first, β a time constant for the collisions and the average density of the MOT $\bar{n}$. Here we will go through the process to calculate the peak density of the TCMOT. We measure the size of the atoms cloud by fitting the fluorescence image to a 2D Gaussian. The results can be seen in figure (4.9).

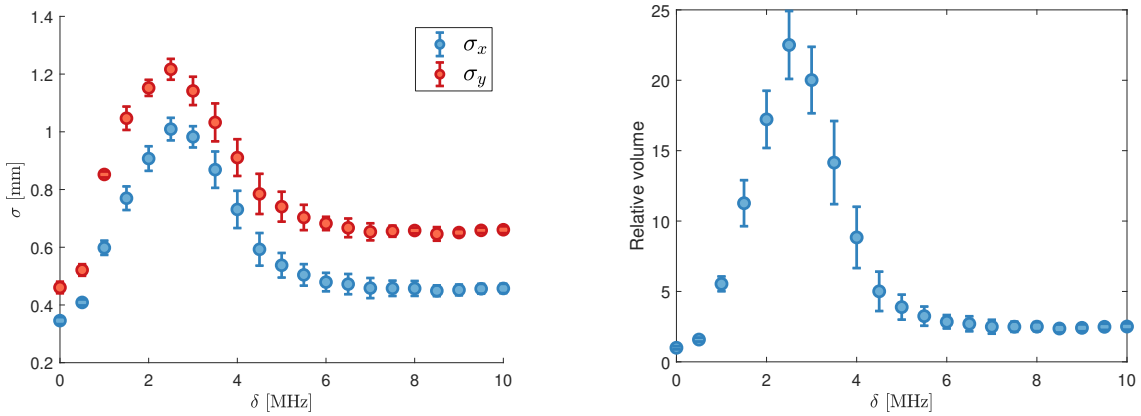

(a) (b)

Figure 5.4: (a) σ_x and σ_y as a function of δ measured in the trap with fluorescence imaging. The atom cloud is larger in the y direction that in the x direction and the difference becomes more pronounced at larger values of δ. (b) Relative volume of the MOT cloud as a function of δ measured in the trap with fluorescence imaging. The volume was normalised to $\delta = 0\,\text{MHz}$ and the peak volume was $19.5\,\text{mm}^3$.

Due to the geometry of the magnetic field generated by the Helmholtz coils being cylindrical symmetry, we assume that the atom cloud is also has a cylindrical symmetry and therefore $\sigma_x = \sigma_z$. We can then estimate the volume of the atom cloud using,

$$V = (2\pi)^{3/2}\sigma_x^2\sigma_y. \tag{5.2}$$

Equation (5.2) comes from estimating the density profile of a MOT to be Gaussian and integrating over space [Barrett, 2017]. As the image only captures a 2d projection of the cloud a full estimation can be difficult but has been attempted in [Overstreet et al., 2005]. Combining the atom number with the volume we can calculate the density of the TCMOT as a function of δ.

$$\bar{n}(\delta) = N(\delta)/V(\delta) \tag{5.3}$$

Following convention the density is measured in Atoms/cm^3.

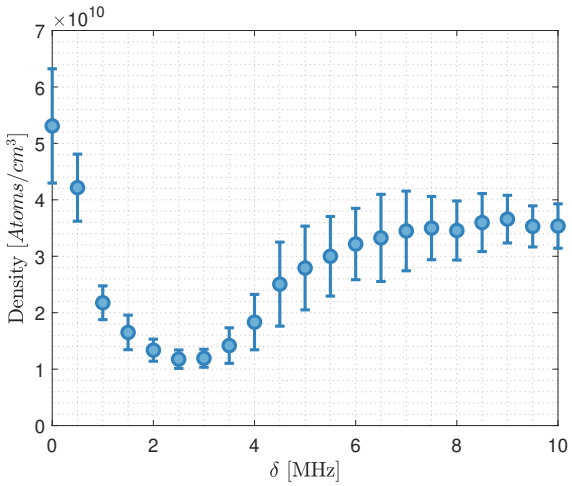

Figure 5.5: Atomic density as a function of δ. We can see that the density is minimum at $\delta = \Gamma/2$. This shows that the volume of the TCMOT increases faster than the atom number in the TCMOT. At large δ we see the density tending to a limit of $3.5 \times 10^{10}\text{Atomscm}^{-3}$ which is lower than the single colour value

The density is a minimum at $\delta = 3\,\text{MHz} \simeq \Gamma/2$ however, the peak is broadened making the exact value of δ where the minimum occurs unclear.

Again from equation (2.49) when $\dot{N} = 0$ then we can show,

$$V = \frac{\beta}{R - \gamma N} N^2. \tag{5.4}$$

If $\gamma N << R$ and β is constant then $V \propto N^2$.

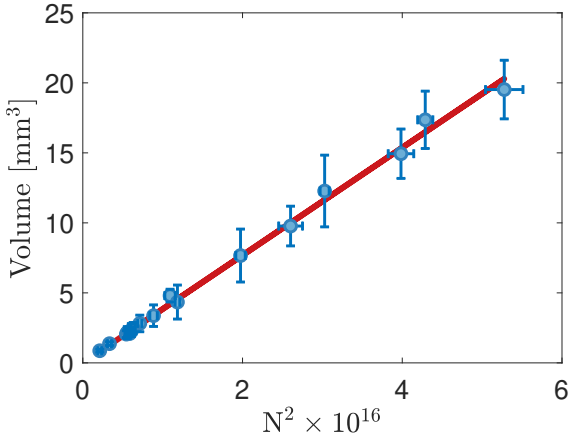

Figure 5.6: Volume as a function of N^2 where N is the number of atoms in the trap. The data was taken for a range of two colour detunings. The linear relation between N^2 and V implies that the light-induced loss rate β is constant.

We see in figure (5.6) that the gradient is between N^2 and V linear. This implies that the light loss collisions between two atoms β remains constant for both the single

colour and TCMOT. This contradicts the proposed explanation for the two colour MOT as presented by [Qiang et al., 2012]. The increase in atom number and loading time can now be attributed solely to an increase in the volume of the trapped cloud. Therefore the question becomes what causes the increase in this volume. As a first-order approximation we can assume that in the steady-state the damping term is negligible we can now estimate the size of the MOT in one direction using

$$k_b T = \kappa x^2, \tag{5.5}$$

here k_b is the Boltzmann constant, T is the temperature of the atom cloud and κ is the restoring force that pushes the atoms towards the centre of the trap. The large volume can arise due to a weaker trap or a larger temperature of the atoms in the MOT.

5.2.3 Temperature

One of the defining characteristics of a MOT cloud is the temperature of the cloud. The method to measure the temperature of an atom cloud is outlined earlier in chapter 3. In figure (5.7) we measure the temperature of the atom cloud as a function of δ.

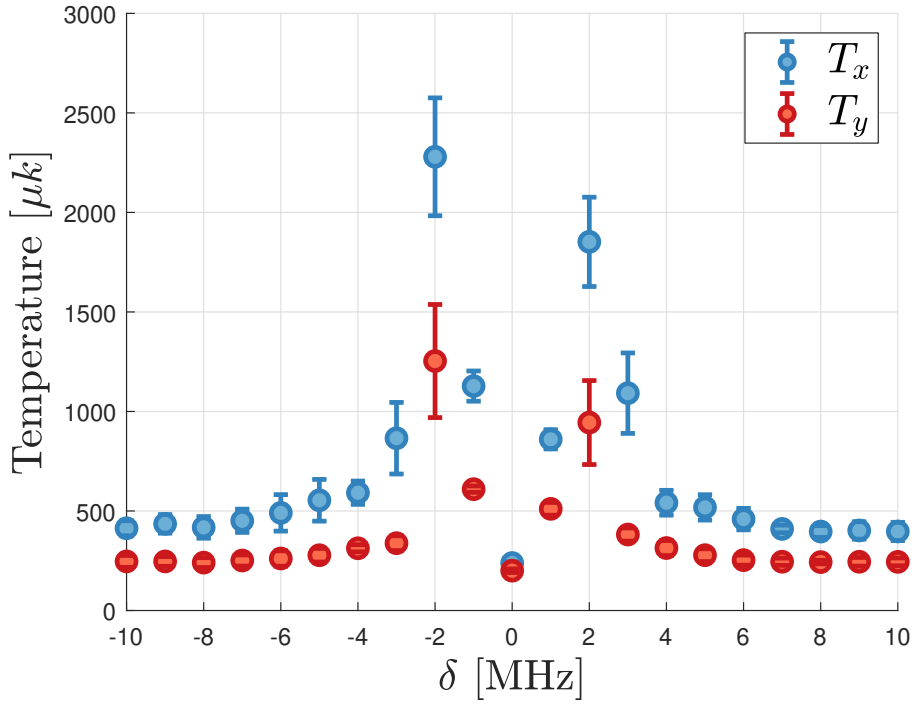

Figure 5.7: Temperature vs detuning. The temperature peaks at ±2 MHz. This is different from the peak atom number which peaks at ±3 MHz. There is a consistent miss-match between the temperature in the x and y directions. This is due to the different trapping frequency from the anti-Helmholtz coils which has twice the magnetic gradient in the y-direction than the x-direction.

There appears to be some disagreement between the value of δ where the peak temperature occurs and where the peak atom number occurs. In all cases, the two colour temperature is much higher than that of the single colour value of $\sim 100\,\mu\text{K}$. There is the possibility that at $\delta = 3\,\text{MHz}$ the very hot part of the atom cloud escaped before being imaged. Even if the atoms could not leave the imaging region in the $5 - 15\,\text{ms}$ of time of flight, the density of atoms could fall enough such that the atoms could not be differentiated from background noise.

5.3 Measuring the forces on the two colour MOT

To try and understand the TCMOT it is necessary to understand the forces that act on the atoms in the trap. To achieve this we followed the examples shown in [Kim et al., 2005] and [Xu et al., 2002]. In these papers, they displaced the atom cloud from its equilibrium position using an on resonance beam. When the beam is turned off the atom cloud returns to an equilibrium position undergoing damped harmonic motion. In a standard MOT set up the damping coefficient, β, is such that the motion of the atom cloud is critically damped. To observe oscillations of the atom position we minimise the power in the MOT beams. In the usually operating regime of the MOT the light intensity is many orders of magnitude than the saturation intensity. In this regime, the damping frequency exceeds the trapping frequency leading to the atoms being over-damped.

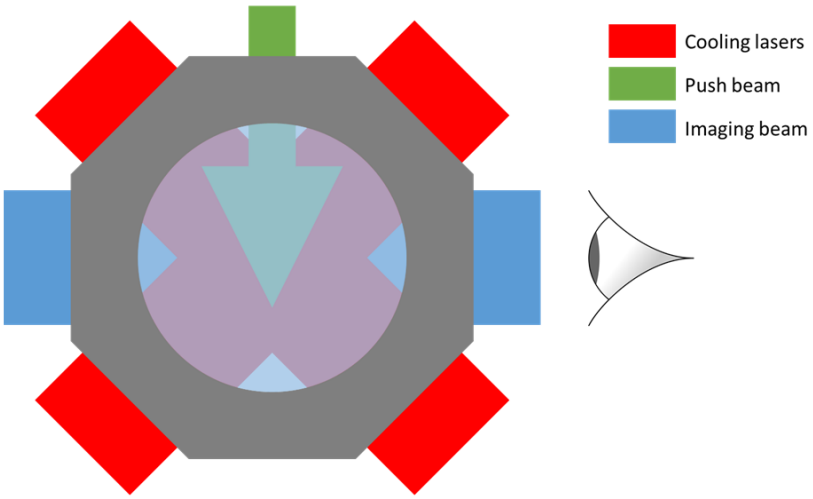

Figure 5.8: A basic top down image of the push beam layout. The push beam displaces the atom cloud perpendicular to the imaging beam as indicated by the green arrow. The push beam had a total power of 0.22 mW with a $1/e^2$ of 26 mm.

This set up is slightly complicated by the restoring force having components from two of the cooling beams. Therefore the total force on the atoms will be roughly $F_T = 2\sqrt{2}F$ depending on the exact angle of the beams to the atoms.

5.3.1 Damped harmonic oscillator theory

In this section we will go over the basic theory of the damped harmonic oscillator and how we will use this to recover the damping coefficient α and the spring constant κ. The motion of a damped harmonic oscillator is described by

$$m\ddot{x} + \alpha\dot{x} + \kappa x = 0. \tag{5.6}$$

As 5.6 is a homogeneous second order differential equation, 5.6 has a solution of the form,

$$x = e^{\lambda t}, \tag{5.7}$$

where λ is is the roots of the auxiliary equation

$$m\lambda^2 + \alpha\lambda + \kappa = 0. \tag{5.8}$$

Depending on the magnitude of the damping constant α and the spring constant k the system can be in one of three regimes. Which regime depends on the value of the discriminant

$$\zeta = \alpha^2 - 4m\kappa. \tag{5.9}$$

First, in the overdamped regime, the position of the oscillator decays exponentially towards the point of equilibrium. This case happens when $\zeta < 0$. Second, Critical damped where the oscillator returns to the origin in the minimum time and $\zeta = 0$. The third case is where the oscillator is under-damped, $\zeta < 0$. Here the oscillator will cross the origin several times. An under-damped oscillator is described by,

$$x = Ae^{-\gamma t}cos(\omega_1 t - \phi), \tag{5.10}$$

where

$$\omega_1 = \sqrt{\omega_0^2 - \gamma^2} \tag{5.11}$$

and ϕ is a phase shift determined by the initial velocity of the oscillator. Equation (5.10) describes an oscillator with an exponentially decaying amplitude. The frequency of the oscillations are effected by the magnitude of the damping. To recover α and κ we use the relations

$$\alpha = 2\gamma m, \tag{5.12}$$

and

$$\kappa = \omega_0^2 m. \tag{5.13}$$

5.3.2 Push beam experiment

Using the theory in chapters two and three we can estimate the values of α and κ. The functions for α and κ are taken from [Metcalf and van der Straten, 2001].

$$\alpha = \frac{|\Delta|}{\Gamma}\frac{8\hbar k^2 s_0}{(1 + s_0 + (\frac{2\Delta_\pm}{\Gamma})^2)^2}, \tag{5.14a}$$

$$\kappa = \frac{\partial B}{\partial x}\frac{|\Delta|}{\Gamma}\frac{8k s_0 \mu'}{(1 + s_0 + (\frac{2\Delta_\pm}{\Gamma})^2)^2}. \tag{5.14b}$$

Where $\Delta_\pm$ is the same as in equation (2.48). Here $\frac{\partial B}{\partial x} = \frac{1}{2}\frac{\partial B}{\partial z}$ and μ' is the effective magnetic moment for the transition. In this theory, κ can be expressed as a function of α as both α and κ are functions of the scattering rate of the atoms in the trap. The scattering rate is given by,

$$\frac{|\Delta|}{\Gamma}\frac{8 s_0}{(1 + s_0 + (\frac{2\Delta_\pm}{\Gamma})^2)^2}, \tag{5.15}$$

which is a function of detuning and intensity of the light. Therefore, we can express α and κ as,

$$\kappa = \frac{\mu'}{\hbar k}\frac{\partial B}{\partial x}\alpha. \tag{5.16}$$

This will come up again later in the results section when the two colour MOT breaks this dependence of κ on α. The absorption images can give accurate information on the position of the atoms however the density distribution is often not Gaussian especially for larger displacements and turning points. This makes atom number estimates more inaccurate. We fit the position of the cloud position using a 2d Gaussian. At large displacements, this can become inaccurate due to the deformation of the cloud.

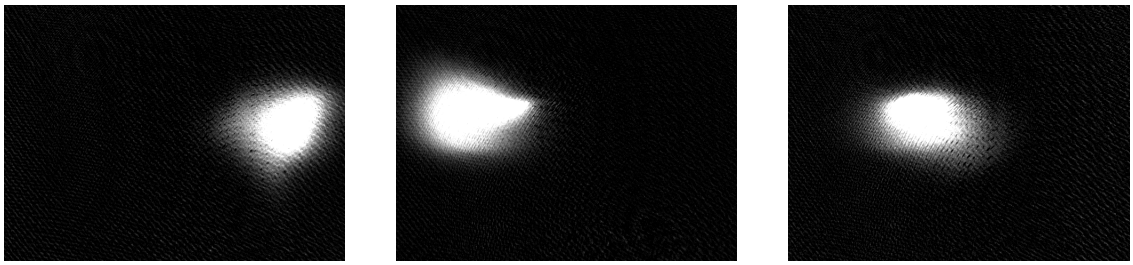

(a) 0 ms (b) 14 ms (c) 50 ms

Figure 5.9: Optical density images of the atom cloud for different release times which shows the atom cloud in different stages of the oscillation. Each image is 480 pixels by 640 pixels or 10.4 mm by 138 mm. The relative detuning between the two beams was 3 MHz (a) The atom cloud after loading with the push beam on. The atom cloud is displaced from the usual equilibrium position. The image was taken 0 ms after the push beam is turned off. (b) The atom cloud at the leftmost position in the oscillation. The cloud has deformed so that there is a central region from which atoms stream out to the left. The image was taken 14 ms after the push beam was turned off. (c) The final image was taken 50 ms after the push beam was turned off. The atom cloud is at the equilibrium position and is no longer oscillating.

5.3.3 Method

To observe under-damped oscillations we minimised the optical power in the cooling beams whilst still retaining 1×10^7 atoms in the trap. The optical power was 3 mW/beam/cooler with a $1/e^2$ of 27.03 mm. The push beam had total power of 0.22 mW with a $1/e^2$ of 26.5 mm. The push beam was aligned to the centre and the atoms so that the height displacement of the atoms by the push beam was minimised. At the MOT gun, the push beam light was circularly polarised however the polarisation of the push beam light into the optical fibre was not controlled therefore the final polarisation of the push beam light was random. The coils had a current of 35 A which translates to a magnetic field gradient of 9.8 Gcm^{-1}. During the loading of the atom cloud, the push beam was on such that the

atoms were loaded into the displaced position. The atoms were loaded in the trap for 90 s after which the push beam was turned off. We take images at 2 ms intervals with 500 µs time of flight. The short time of flight is necessary for fields from the anti-Helmholtz coils to go to zero so that it does not interfere with absorption imaging. The initial position the atom cloud varied by ~ 1 mm due to changes in the spring constant. This change is accounted for in the curve fitting when calculating α and κ.

5.3.4 Results

We found that α and κ have been reduced with a minimum at $\delta \simeq 3$ MHz. This section will go into more detail. Initially, in figure (5.10) we show a visual difference between the pseudo-single case and the two colour at $\delta = 3$ MHz case.

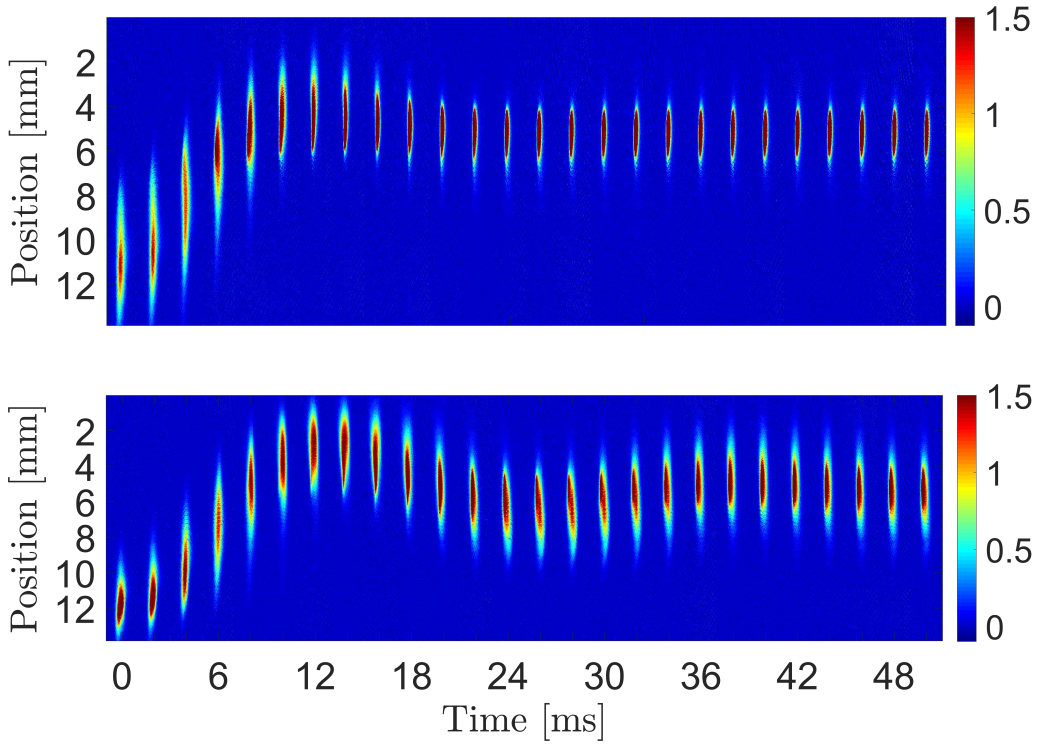

Figure 5.10: Top: Composite image of the atom cloud oscillating taken at $\delta = 0$ MHz. Bottom: Composite image of the atom cloud oscillating taken at $\delta = 3$ MHz. The lower plot $\delta = 3$ MHz visually has a different spring constant and damping co-efficient

In the top image of figure (5.10) the atoms undergo a half an oscillation before reaching a steady state. In the bottom image of figure (5.10) the atoms undergo several oscillations. In both cases, the optical power remains the same so the only difference between the two cases is the frequency difference between the two cooling lasers.

We aligned the push beam to the centre of the window and so that the beam passed

through the window at 90° Whilst we only wanted oscillations to occur in one dimension there was some oscillation in the y direction that we could measure and possibly some in the z direction which would be towards the camera and therefore we could not measure motion in that direction.

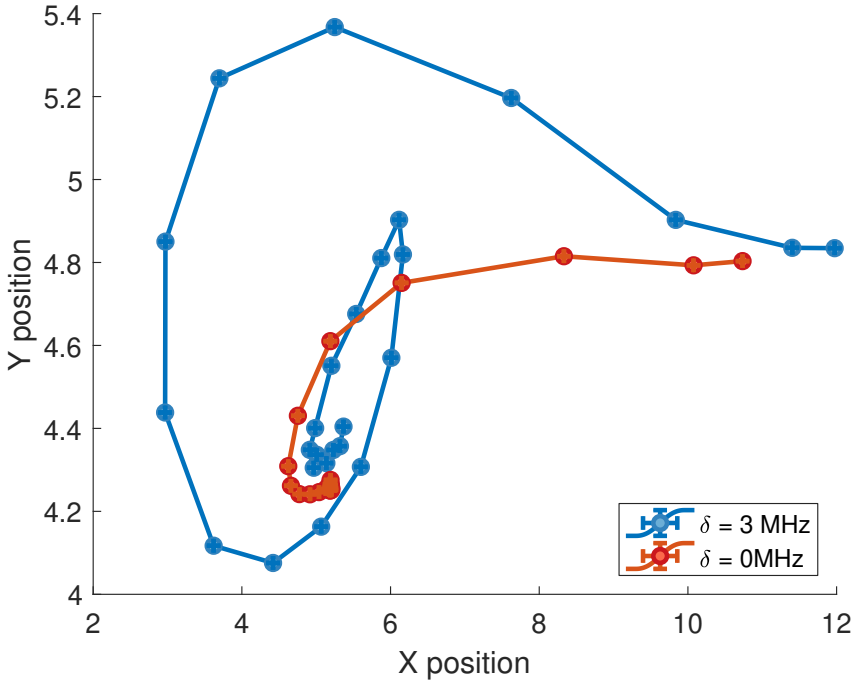

Figure 5.11: 2d view of the atoms undergoing damped harmonic motion. This image gives a more complete description of the motion of the atoms. The different values of δ also have a slightly different trap centre in the y-direction. Note that the scaling of the two-axis is not the same and that the Y-axis is $\sim 1/10$ the size of the x-axis.

It can be seen here that the orthogonal displacements were greater in the 3MHz case. We can attempt to re-create the 3d path of the atom cloud as it returned to the equilibrium position. Now that we have compared individual cases we scan δ and measure κ and α. We only ran the scan from $\delta = 0\,\text{MHz}$ to $\delta = 7\,\text{MHz}$ as beyond $\delta = 0\,\text{MHz}$ the results become consistent as demonstrated by the atom number.

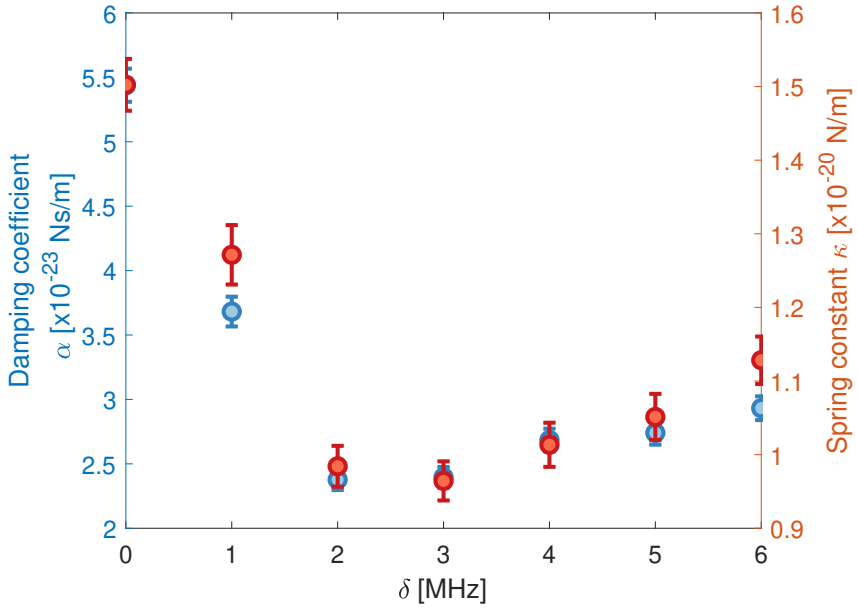

Figure 5.12: α and κ as a function of δ. Both α and κ have a similar profile to the atom number, where the minimum value of α and κ happens at $\delta \simeq \Gamma/2$.

Figure (5.12), α and κ both decrease as the atom number increases. The decrease in the force was predicted in the theory, however, as shown in fig (5.3) that the loading rate remains constant with δ. As the force decreases we would also expect a decrease in loading rate. This phenomenon is as yet unexplained. As we showed in equation (5.16) that κ is a function of α. To show the relation between the two and calculate the gradient, we plot α vs κ.

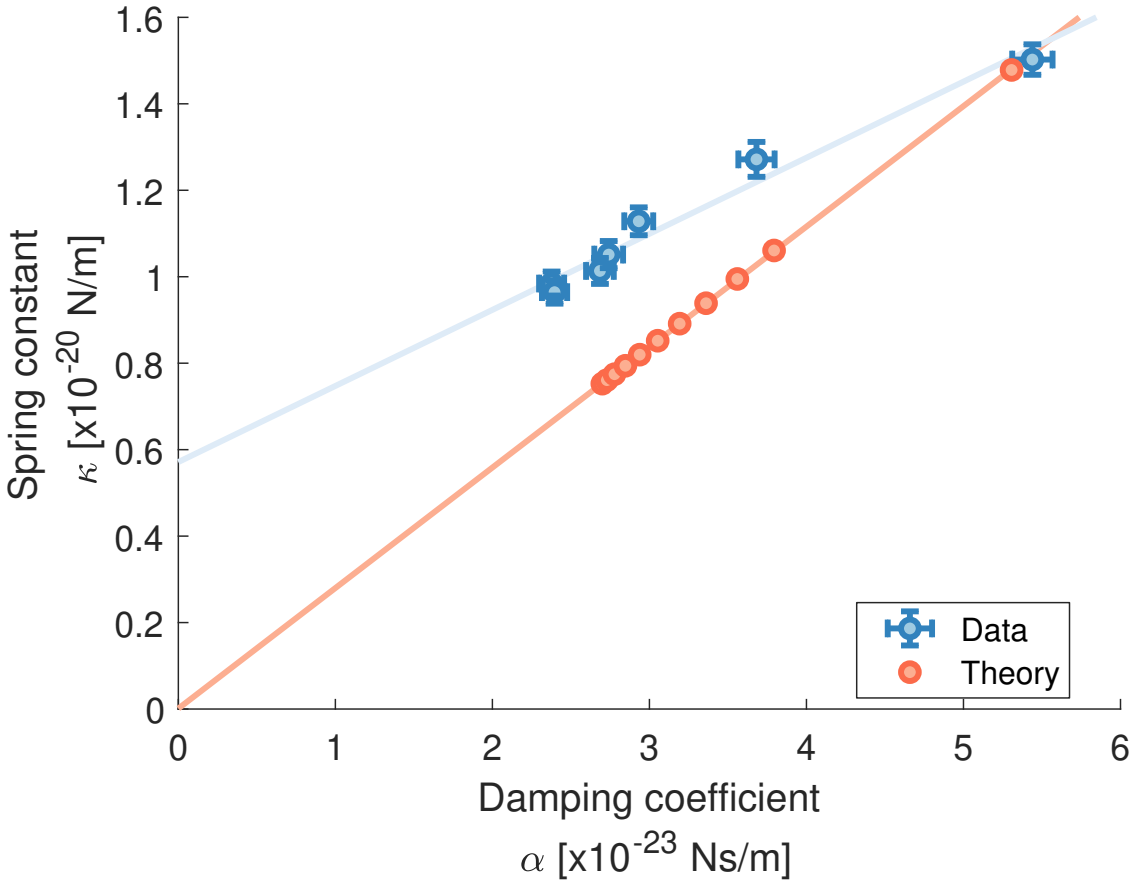

Figure 5.13: Plot of α vs κ. From equation (5.16) and the theoretical predictions, we expect the fit of the data to pass through zero. The theoretical prediction was made by estimating the light intensity and magnetic field gradient for the $\delta = 0\,\text{MHz}$ case. This was then used to simulate the atom trajectories. The trajectories were then fitted using the same fitting routine that fit the data.

As shown equations (5.16) we expect $\kappa = \eta\alpha$, where η is some gradient that depends on the scattering rate.

The result in figure (5.13) shows that $\kappa = \eta\alpha + c$ where c is an offset. This offset suggests that there is a trapping force that is independent of the scattering rate of the TCMOT. One source of the additional spring constant could be from a positional trapping force that arises from the beat note. The result is surprising but can help to explain the properties of the two colour MOT and differentiates the two colour MOT from a single colour MOT with lower beam power. The trapping force is higher than it would be for a single colour MOT with the same value of α. The the lower value of α leads to a higher steady-state temperature as shown in equation (2.45). The higher temperature increases the size of the atom cloud as shown in equation (5.5). In the single colour, case decreasing the intensity of the cooling beams would have a two-fold effect on the MOT size whereas

the effect is reduced in the two colour MOT when comparing equal α values.

5.4 Utilising the two colour MOT

Atom number is not the sole desirable property of a cold atom source. It is useful to maximise the phase space density of the MOT whilst retaining a large atom number as methods such as evaporate cooling cause atoms to be expelled from the trap. The two colour MOT has a large atom number but has a low density and a large cloud size. We then looked for a way to increase the phase space density of the MOT.

5.4.1 MOT compression

In this section, we demonstrated a method for cooling and compressing the two colour magneto-optical trap. We call this method "MOT compression" as it reduces the size of the MOT and increases the density of the MOT. This method returns the TCMOT to a single colour MOT but retains the two colour atom number due to the two different time scales over which the MOT returns to single colour. We will then go on to compare properties of the two colour MOT with MOT compression and the single colour MOT.

After the MOT had completed the loading cycle we tried turning off one of the cooling lasers and returning the other cooling laser to the optimum frequency (optimum for atom number).

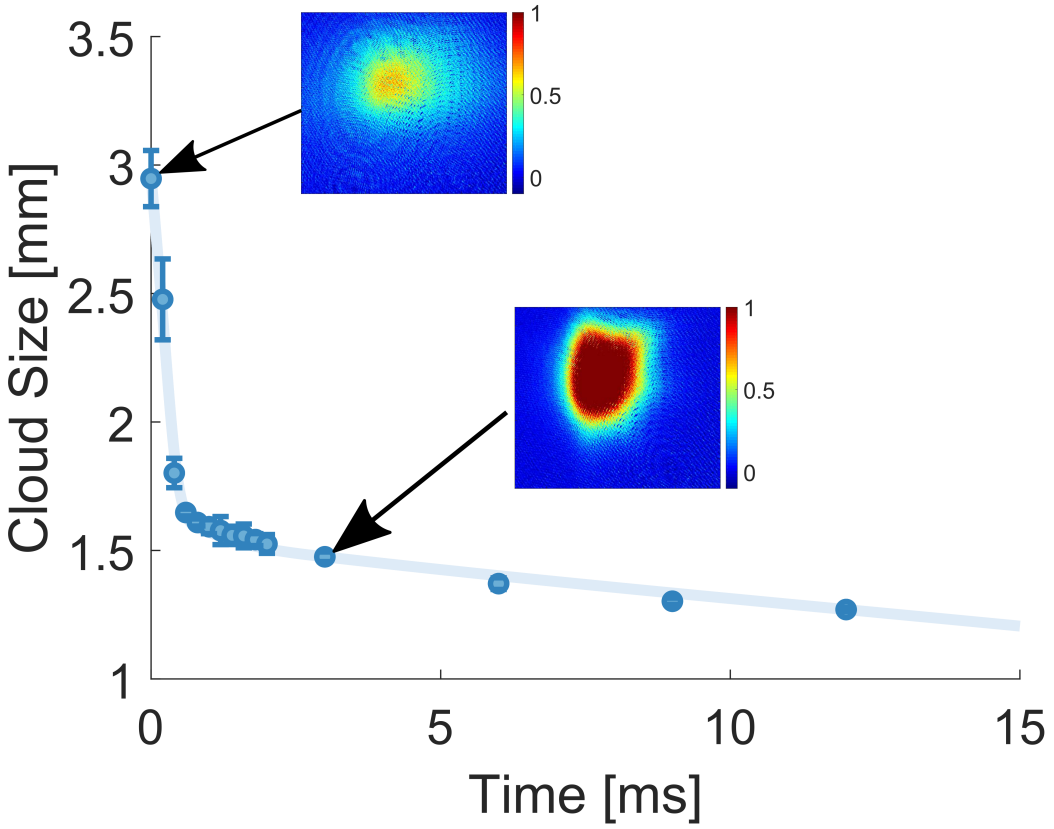

Figure 5.14: A plot of the cloud size as after the second cooling frequency has been turned off. The image insets are optical density images at different points in the MOT compression stage. These images show visually the increase in density of the atom cloud. The single colour MOT has an in-trap size of 0.9 mm. The blue line is a guide for the eye.

Here in figure (5.14) we see that the atom cloud collapses in size over ~ 3 ms. This compression is on the same time scale as the rate at which thermal atoms are cooled. The decrease in size is due to the increase in α so that the steady-state temperature decreases. This is true even when we turn off one of the beams to perform the MOT compression as opposed to making the two cooling lasers have the same frequency. We can assume that the MOT will have no memory of its initial conditions, therefore, we assume that the atom number would return to the single colour value.

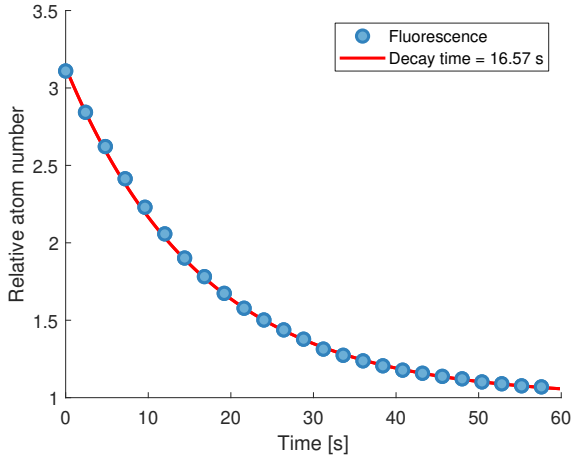

Figure 5.15: Fluorescence measure with a photo-diode. The atom number is proportional to the fluorescence and therefore the atom number. This then shows the rate at which atoms leave the trap

We can see in figure (5.15) that over a long time the atoms begin to leave the trap. The trend follows the loading rate differential equation (2.49) with different initial conditions. In this case, the loss rates exceed the loading rate and the trap loses atoms at an exponentially decreasing rate. Fortunately, the cooling and loss rate times scales are vastly different so that there is a window in which the atom cloud can be loaded into a magnetic trap.

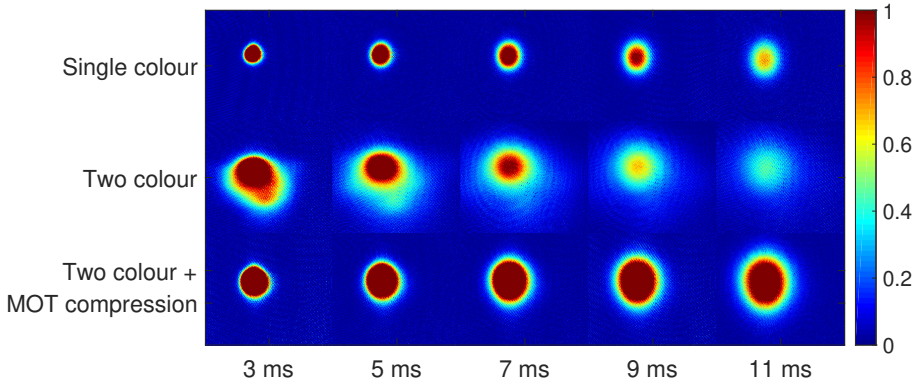

Figure 5.16: Left to right: Images taken at increasing time of flight 1-9ms with 2ms spacing. Top: true single colour The density colour map goes from yellow (high density) to blue (low density). The TCMOT + MOT compression has a higher central density than both the TCMOT and single colour MOT after 11 ms time of flight.

Figure (5.16) shows optical density images for three different cases, single colour, two colour and two colour with compression. The single colour and two colour with MOT compression have both been cooled using optical molasses. We can see that the two colour

MOT with compression has a higher optical density after 11 ms time of flight. The single colour MOT and two colour MOT with compression have similar expansion rates whereas the two-colour case the MOT seems to expand rapidly. This is because both atom clouds have a similar temperature of $\sim 13\,\mu K$ whist the two colour MOT is at a much larger temperature ($500\,\mu K$).

	Single Colour	Two colour
Atom Number	3.27×10^7	1.95×10^8
Temperature	$13.6\,\mu K$	$13.6\,\mu K$
Density Atoms/cm^3	4.06×10^{10}	3.3×10^{10}
PSD	5.33×10^{-6}	4.52×10^{-6}

Table 5.1: A comparison between the single and two colour magneto optical traps after molasses cooling. The temperature and atom density are similar however the atom number of the TCMOT is much larger than the single colour MOT.

This table shows that the two colour MOT can be used to get a similar phase space density to that of a single colour MOT whilst having $\sim \times 6$ the number of atoms. The density of the two colour MOT is lower than the single colour MOT by a small amount. The two colour MOT was compressed using to a pseudo-single colour MOT rather than a full single colour MOT. A full single colour MOT should recover an equal density as the single colour MOT.

5.5 Conclusion

In this chapter, we presented a novel method of improving the atom number in the magneto-optical trap. This was achieved by adding a second cooling beam that has a slightly different frequency from the first cooling beam. We showed that this setup resulted in a five to six times increase in the number of atoms in the trap. In the paper by Cao Qiang et al [Qiang et al., 2012] they stated that the increase in atom number was due to the increase in the trapping volume, which we have confirmed experimentally. In the paper they attributed this to a change in the light-induced loss rate, we have experimentally shown that this is not the case. We have found that the increase in volume is instead due

to a reduction in the cooling efficiency of the TCMOT and a reduction in the stiffness of the trap. The increased atom number is beneficial for the formation of BECs in multiple ways. First, the increased atom number offsets the losses due to evaporative cooling and secondly, the increased atom number and density result in shorter rethermalization time. However, the TCMOT increases the time it takes to fully load atoms into the trap. This can be offset by the use of a 2d MOT which is used in other experiments for the rapid loading of the magneto-optical trap [Berthoud et al., 1998].

Chapter 6

Ultra-cold atom magnetic microscopy

Magnetic microscopy is the measurement of magnetic fields on a microscopic scale. Ultra-cold atoms make effective magnetometers due to the low energy scales needed to effect the atoms [Wildermuth et al., 2005]. This makes the atoms very sensitive to magnetic fields. By confining the atoms in a one-dimensional trap, we can make the atoms sensitive to a single component of the magnetic field allowing ultra-cold atoms to act as a vector magnetometer. We measure magnetic fields with the ultra-cold atom magnetic microscope by measuring variations in atom density. This variation in atom density is proportional to the magnetic field being measured which we will refer to as B_{ext}. These magnetic fields are usually generated by wires but can arise from other sources.

Magnetic microscopes are used in a range of applications from measuring current flow in graphene [Tetienne et al., 2017] to measuring individual domains in [Nolting et al., 2000]. A range of magnetic microscopy techniques is summarised in [Freeman and Choi, 2001]. In this section, we will consider the use of ultra-cold atoms as a magnetic microscope and derive the sensitivity and responsivity of a cold atom microscope in the thermal and Bose-Einstein condensate (BEC) regime.

To accurately map out the spatial magnetic field of a sample we need fine spatial control of the atom cloud. To achieve this control we can use magnetic traps or optical traps and in some cases a mix of both. There is a verity of ways to create a magnetic trap for the atoms, these include atom chips [Folman et al., 2008], permanent magnets [Vuletic et al., 1998] and printed circuit boards (PCB) [Roy et al., 2017]. In this chapter, we will consider the cold atom magnetic microscope that strongly confines atoms in two axes and has weak confinement of the atoms in the third axis. In this type of trap, the

atom cloud is elongated in the weakly confined axis so that the trap is effectively one dimensional. We denote the magnetic field in the weak trapping direction as $B_{\parallel}$ and the magnetic field in the strong trapping direction as $B_{\perp}$. Outside the trap centre $B_{\perp}$ is much greater than B_{ext}.

In the strong trapping direction, the magnitude of the magnetic fields of the trap is much larger than the external magnetic field component. Therefore, the atoms are not affected by the external magnetic field in the strongly confined directions. In the weak trapping direction, the external magnetic field component is larger than the trapping fields and therefore can affect the spatial atomic density along the weak trapping axis. This allows the ultra-cold atom microscope to act as a vector magnetometer as it measures one direction of the magnetic field. The other directions of the magnetic field can be measured by changing which axis is weakly confined.

The responsivity of a system is defined by the input-output gain of a detector system. In the case of the cold atom microscope, we define responsivity as the magnitude of the change in atom density with a change in the measured magnetic field. The sensitivity of the system is a measure of what is the smallest change in the magnetic field that can be detected by the system. The sensitivity of the system depends on how precisely we can measure the change in atom density. How precisely we can measure the change in atom density depends on the imaging system measuring the atom density. Experiments have been shown to measure better than 1 atom/µm in absorption imaging [Wildermuth et al., 2005].

The potential energy a neutral atom gains due to a magnetic field depend on the magnetic sub-level the atom is occupying. An atom in a magnetic field has a Zeeman energy [Foot et al., 2005], (a more in-depth discussion of Zeeman splitting is covered in 2.2.1),

$$V = m_f g_f \mu_b |\vec{B}|. \tag{6.1}$$

Here m_f is quantum number associated with the Zeeman state of the atom, g_f is the Lande g factor for an electron and μ_b is the Bohr magneton. The atoms If the atom passes through a global zero in the magnetic field it can undergo a Majorana spin-flip [Brink and Sukumar, 2006]. The spin-flip changes the state of the atom from a trapped state to an anti-trapped state where the atom is expelled from the trap. To avoid Majorana spin-flip losses a homogeneous offset field is applied to the trap to remove the magnetic global zero.

6.0.1 Ioffe-Pritchard trap

The potential of a harmonic trap is given by,

$$V = V_0 + \frac{m}{2}(\omega_x^2 x^2 + \omega_y^2 y^2 + \omega_z^2 z^2). \tag{6.2}$$

where m is the mass of the atom in the trap and ω_i is the frequency of the trap in the i^{th} direction. In the real world, it is not possible to generate a perfect harmonic trap over a large volume. It is possible to generate a harmonic potential over a small volume with the potential becoming more anharmonic away from the centre of the trap. We will look at the Ioffe-Pritchard trap as an example of a trapping potential that approximates a harmonic potential over a small region [Pethick and Smith, 2008]. We also add in a small external field that will be measured by the cold atoms. As we mentioned in the introduction, $B_\perp$ is much greater than $B_{ext}(x, y)$, therefore, we can say that B_{ext} only has z dependence. The Ioffe-Pritchard trap is defined as [Pethick and Smith, 2008, p. 64],

$$\mathbf{B}_{trap}(x, y, z) = (B_0 + B_{ext}) \begin{pmatrix} 0 \\ 0 \\ 1 \end{pmatrix} + B^{''} \begin{pmatrix} -xz \\ -yz \\ z^2 - \frac{1}{2}(x^2 + y^2) \end{pmatrix} + B^{'} \begin{pmatrix} x \\ -y \\ 0 \end{pmatrix} \tag{6.3}$$

We then calculate the magnitude of the magnetic field $|\mathbf{B}|$

$$|\mathbf{B}| = (B_0 + B_{ext}) \sqrt{1 + \frac{r^2}{2(B_0 + B_{ext})} \left(\frac{B'}{(B_0 + B_{ext})} - \frac{B''}{2} \right)}, \tag{6.4}$$

where $r = \sqrt{(x^2 + y^2)}$. We then Taylor expand equation (6.3) to the first order giving,

$$|\mathbf{B}| = B_0 + B_{ext} + r^2 \left(\frac{B'}{B_0 + B_{ext}} - \frac{B''}{2} \right) + \frac{z^2 B''}{2}. \tag{6.5}$$

where $B^{''}$ is the curvature of the trap, $B^{'}$ is the gradient of the quadrapole trap and B_0 is the magnitude of the offset field. These values relate to the trapping frequencies by,

$$\begin{aligned} \omega_\parallel &= \sqrt{\frac{B'' m_f g_g \mu_b}{m}} \\ \omega_\perp &= \sqrt{\frac{m_f g_g \mu_b}{m} \left(\frac{B'}{B_0} - \frac{B''}{2} \right)}. \end{aligned} \tag{6.6}$$

Usually, the trapping frequencies are defined from $B^{'}$ and $B^{''}$ however in our simulations we define the trapping frequencies then calculate $B^{'}$ and $B^{''}$ for the Ioffe-Pritchard trap. The total potential experienced by the atoms is,

$$V(r) = V_0 + V_{ext} + \frac{1}{2} m \omega_\perp^2 r^2 + \frac{1}{2} m \omega_\parallel^2 z^2, \tag{6.7}$$

where,

$$V_{ext} = m_f g_f \mu_b B_{ext} \tag{6.8}$$

Here we have shown that the Ioffe-Pritchard trap approximates the harmonic trap over a small volume. We have also shown that the perturbing magnetic field can be separated from the trap. We can, therefore, consider variations in the external field as variations in the potential of the magnetic trap without needed to add the fields in a vector. We express the total magnetic field as

$$V(r) = V_0 + V_{ext} + V_{\parallel} + V_{\perp}. \tag{6.9}$$

6.1 Thermal atoms

In this section, we will show how thermal atoms in an Ioffe-Pritchard trap respond to a weak external magnetic field. When the temperature of the atoms is above the critical temperature of condensation, the density distribution of the atoms is described by the Boltzmann distribution,

$$n(r) = n_0 e^{-\frac{V(r)}{k_b T}}. \tag{6.10}$$

The peak atom density n_0 is calculated by dividing the total number of atoms N by the volume of the atom cloud occupies. However, to get a finite volume we must use a non zero value for $\omega_{\parallel}$. n_0 is therefore given by,

$$n_0 = \frac{N}{\iiint e^{\frac{\frac{1}{2}m\omega_{\perp}^2 r^2 + \frac{1}{2}m\omega_{\parallel}^2 z^2}{k_b T}} d^3 r}. \tag{6.11}$$

This equation is solved using the identity

$$\int_{-\infty}^{\infty} e^{\frac{x^2}{\beta}} dx = \sqrt{\pi\beta} \tag{6.12}$$

This then gives

$$n_0 = N\omega_{\perp}^2 \omega_{\parallel} \left(\frac{2\pi k_b T}{m} \right)^{-\frac{3}{2}}. \tag{6.13}$$

To go from a 3d density distribution to a 1d density distribution we integrate over the transverse directions again using the identity above to get,

$$n_{1d}(z) = \iint n(r) dx dy = \frac{2\pi k_b T}{m\omega_{\perp}^2} n_0 e^{-\frac{V_{\parallel} + V_{ext}}{k_b T}} \tag{6.14}$$

Figure (6.1) below shows the 1d density profile for atom clouds in the ideal potential at three different temperatures.

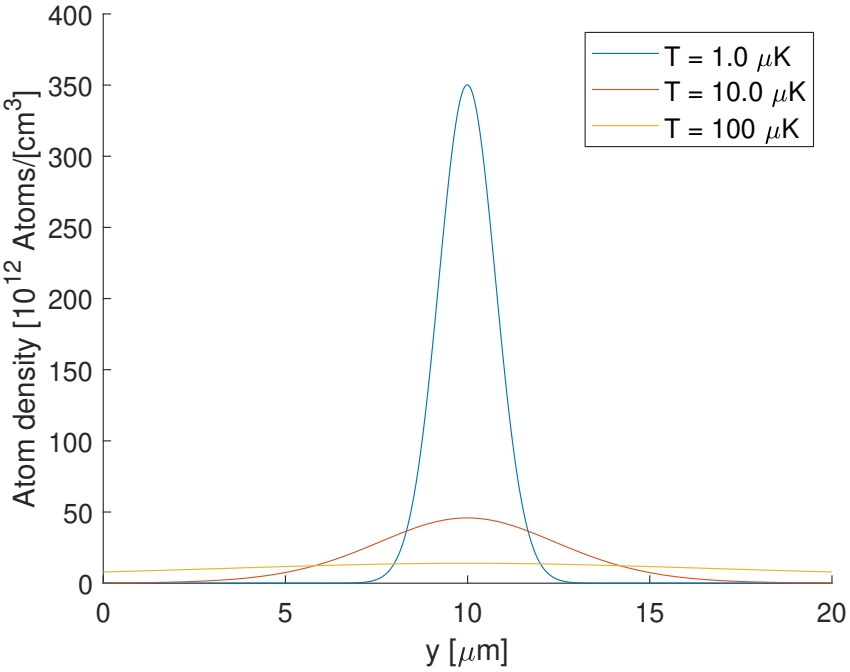

Figure 6.1: Gaussian distributions of thermal atoms in an Ioffe-Pritchard trap looking along the transverse direction. As the temperature increases, the width of the atom cloud becomes exponentially larger. Even at 100 µK the atom cloud becomes spread out over many µm. This highlights the importance of the atom cloud being cold for microscopy. $\omega_\perp = 2\pi \times 2\,\mathrm{kHz}$, $\omega_\parallel = 2\pi \times 10\,\mathrm{Hz}$ and each cloud has 1×10^4 atoms.

To recover the magnetic field in the transverse direction we can reverse this equation to get

$$V_{ext} = m_f g_f \mu_b B_{ext} = -k_b T ln(n_{1d}) + V_\parallel. \tag{6.15}$$

Depending on the relative direction of the magnetic field the atom density can increase or decrease. This equation breaks down when the external field becomes more than a perturbation, such that $V_{ext} \sim V_\parallel$.

6.1.1 Responsivity

The responsivity of the thermal atoms in the magnetic trap is defined as change in the local 1d atom density n_{1d} in the presence of an external field B_{ext}. The responsivity is expressed in a differentail form as shown in [Estève, 2004],

$$\frac{\partial n}{\partial B} = -\frac{2\pi\mu_b n_0}{m\omega_\perp^2} e^{-\frac{\mu_b B_{ext}}{k_b T}}. \tag{6.16}$$

Expanding all the terms we get

$$\frac{\partial n}{\partial B} = -\left(\frac{m}{2\pi(k_b T)^3}\right)^{\frac{1}{2}} N\mu_b\omega_\parallel e^{-\frac{\mu_b B_{ext}}{k_b T}}. \tag{6.17}$$

As B_{ext} is a small perturbation we can expand equation 6.17 to first order to find

$$\frac{\partial n}{\partial B} = -\left(\frac{m}{2\pi(k_bT)^3}\right)^{\frac{1}{2}} N\mu_b\omega_{\parallel}(1 - \frac{\mu_b B_{ext}}{k_bT}) \tag{6.18}$$

Therefore the responsivity of the thermal atom microscope is dependent on both atom number and temperature. There is also an interesting dependence on $\omega_{\parallel}$. The responsivity and sensitivity improve with a larger $\omega_{\parallel}$ due to the higher density however many of the approximations made so far have assumed that $\omega_{\parallel} z = 0$, so a larger $\omega_{\parallel}$ decreases the range that we can consider this approximation to be true.

6.1.2 Sensitivity of thermal atoms to external magnetic fields

An external magnetic field will change the local atom density in a trapped thermal atom cloud. This change in density can be measured and used to infer the change in the external magnetic field. For thermal atoms in a magnetic trap the relationship between atom density and the change in the external magnetic field is given by,

$$\Delta B_{ext} = -\frac{\Delta n_{1d}}{N\mu_b\omega_{\parallel}}\left(\frac{2\pi(k_bT)^3}{m}\right)^{\frac{1}{2}}. \tag{6.19}$$

The minimum change in atom density is limited by the experimental imaging system. The response of the atomic cloud to the external magnetic field can be tuned via, the temperature of the atomic cloud, the total number of atoms in the atomic cloud which increase the peak density and decrease the longitudinal trapping frequency. A ^{87}Rb cloud with 1×10^5 atoms at 1 µK has a sensitivity of 5.81 nT. At 10 µK the sensitivity worsens to 183.8 nK.

6.2 Bose-Einstein condensate

A Bose-Einstein condensate (BEC) is a state of matter which shows macroscopic quantum behaviour. The theory behind Bose-Einstein condensation is covered in great depth in the literature [Dalfovo et al., 1999, Pethick and Smith, 2008, Ketterle et al., 1998]. The BEC forms when atoms in a gas cloud are brought to very low temperatures. To stop the atoms that form the BEC from condensing into a solid at the low temperatures requires that the gas cloud has a very low density. At very low temperatures atoms act less like particles and more like waves. As we saw in (2.3) the equation for the de Broglie wavelength is,

$$\lambda_T = \left(\frac{2\pi\hbar^2}{mk_bT}\right)^{\frac{1}{2}}. \tag{6.20}$$

As the temperature, and therefore kinetic energy, of an atom, decreases the thermal wavelength of the atom increases. In a uniform medium, the condition for condensation is,

$$n_0\lambda_T^3 = \zeta(3/2) \simeq 2.61, \tag{6.21}$$

where n_0 is the density of atoms and $\zeta(3/2)$ is the Riemann zeta function evaluated at 3/2. The function $n_0\lambda_T^3$ is called the phase space density and is a unit-less measure of the number of states in a unit volume in phase space. Equation (6.21) states that the condensation condition occurs when there are 2.61 atoms per λ_T^3 in phase space. Rearranging (6.21) for temperature we find that phase transition to BEC occurs when,

$$T_c = \frac{2\pi\hbar^2}{mk_b}\Big(\frac{n}{\zeta(3/2)}\Big)^{2/3}. \tag{6.22}$$

The temperature calculated in equation (6.22) assumes there are no interactions between atoms. A repulsive interaction decreases the density of the atoms and would, therefore, decrease the critical temperature, while an attractive interaction would increase the density and increase the critical temperature [Wilkens et al., 2000].

6.2.1 Gross-Pitaevskii equation

The Gross-Pitaevskii equation (GPE) is a modified time-dependent Schrödinger equation to include the interaction between atoms and is given by [Griffin et al., 1996],

$$\left(-\frac{\hbar^2}{2m}\nabla^2 + V_{ext}(r) + g|\psi(r,t)|^2 \right)\psi(r,t) = i\hbar\frac{\partial}{\partial t}\psi(r,t), \tag{6.23}$$

where m is the mass of the atomic species. The non-linear interaction term $g|\psi(r,t)|^2$ is scaled by the coupling constant g which is given by,

$$g = \frac{4\pi\hbar^2 a_s}{m}. \tag{6.24}$$

Here a_s is the s-wave scattering length, which for ^{87}Rb, $a_s = 5.18\,\text{nm}$ [Egorov et al., 2013]. A positive coupling constant g equates to repulsive interactions between atoms in the BEC. It should be noted that g is only dependent on the atomic species and the scattering length a_s. In some experiments the scattering length can be controlled via Feshbach resonances [Chin et al., 2010] and can even be made negative, therefore making g negative which causes the atoms in the trap to attract to each other. The non-linear term $|\psi(r,t)|^2$ makes the GPE a non-linear equation that makes exact analytic solutions difficult except in very specific cases such as for a free particle and a soliton in 1d.

Thomas-Fermi approximation

For a sufficiently large BEC, we can solve the GPE without the kinetic energy term as the kinetic energy of the atoms is much smaller than the other energy scales involved and can, therefore, be ignored [Pethick and Smith, 2008, p. 168]. This approximation is called the Thomas-Fermi approximation. Solving the GPE without the kinetic energy term we find,

$$n(r) = \begin{cases} \frac{1}{g}(\mu - V(r)), & \text{if } \mu > V(r) \\ 0, & \text{otherwise} \end{cases} \tag{6.25}$$

Here μ is the chemical potential which is calculated by normalising 6.25 to a number of atoms N. In the case of the harmonic oscillator,

$$\mu = \frac{1}{2}\hbar\omega_{ho}\left(\frac{15a_sN}{a_{ho}}\right)^{\frac{2}{5}} \tag{6.26}$$

where we define

$$\omega_{h0} = (\omega_x\omega_y\omega_z)^{\frac{1}{3}} \tag{6.27}$$

which is the average frequency of the trap and the characteristic length of the ground state in the trap,

$$a_{h0} = \sqrt{\frac{\hbar}{m\omega_{h0}}}. \tag{6.28}$$

We can see in these equations that the atoms fill the potential up to the chemical potential giving the atom density the same shape as the trap.

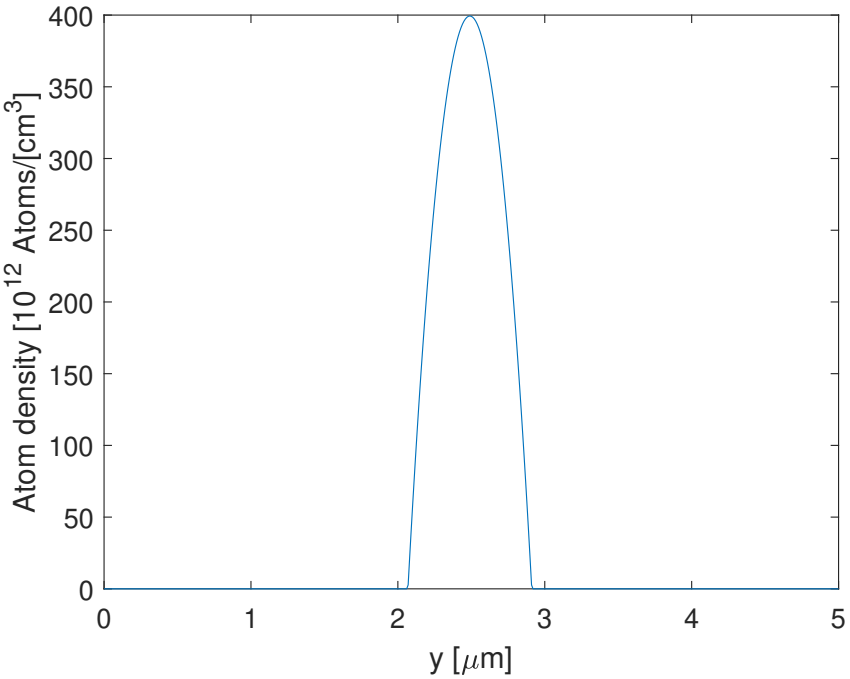

Figure 6.2: Distribution of atoms in a BEC in an Ioffe-Pritchard trap along the transverse direction. The atoms fill the trap to the chemical potential giving a sharp cut off giving the atom cloud density the shape of the potential. Note that the x-axis in this plot is 1/4 the size of the thermal atom plot. $\omega_\perp = 2\pi \times 2\,\mathrm{kHz}$, $\omega_\parallel = 2\pi \times 10\,\mathrm{Hz}$ and the width of the BEC is 842 nm.

6.2.2 Local density approximation

The local density approximation allows us to analytically calculate the 1d density distribution. The chemical potential μ is set by normalising the atom density to the total number of atoms [Gerbier, 2004]. The local density approximation changes the chemical potential spatially depending on the value of the potential. The local chemical potential is given by [Gerbier, 2004],

$$\mu_{l.e}[n_{1d}] = \mu - V. \tag{6.29}$$

Here $_{l.e}$ stands for local estimation. We can then relate the local chemical potential to the atom density in the trap by,

$$\mu_{l.e}[n_{1d}] = \hbar\omega_\perp\sqrt{1 + 4an_{1d}}. \tag{6.30}$$

Combining equations 6.29 and 6.30 and rearranging for n_{1d} we find,

$$n_{1d} = \left(\left(\frac{\mu - (V_\parallel + V_{ext})}{\hbar\omega_\perp}\right)^2 - 1\right)\frac{1}{4a_s}. \tag{6.31}$$

This gives us an equation for the one-dimensional density in the trap.

6.2.3 Responsivity

As before with the thermal atoms, we will calculate the response of the atom cloud. First, we fully expand equation 6.31 then differentiate by the change in magnetic field to get $\frac{\partial n}{\partial B}$,

$$\frac{\partial n_{1d}}{\partial B} = -\frac{\mu\mu_b - \mu_b V}{2a_s\hbar^2\omega_\perp^2}. \tag{6.32}$$

We then assume that $\omega_\parallel^2 z^2 \sim 0$ so that the only change to the density is due to the external field. For ^{87}Rb, $m_f g_f \simeq 1$, therefore we shorten the expression of the potential to, $V_{ext} = \mu_b B_{ext}$, giving,

$$\frac{\partial n_{1d}}{\partial B} = -\frac{\mu\mu_b - \mu_b^2 B_{ext}}{2a_s\hbar^2\omega_\perp^2}. \tag{6.33}$$

This has the same trend as the thermal atoms where the responsivity decreases linearly with B_{ext}. We find that the responsivity of the atom cloud decreases as the perpendicular trapping frequency $\omega_\perp$ is increased.

6.2.4 Sensitivity

As shown before with the thermal atoms, we can re-arrange the equation for the responsivity of the atom cloud to calculate the sensitivity of the BEC,

$$\Delta B = -\frac{2\Delta n_{1d} a_s \hbar^2 \omega_\perp^2}{\mu\mu_b}. \tag{6.34}$$

For a ^{87}Rb cloud with 1×10^5 atoms at 1 µK has a sensitivity of 548 pT which is roughly 10 times more sensitive than the thermal cloud at 1 µK. It is worth noting that the sensitivity is dependent on the transverse trapping frequency, where a smaller trapping frequency leads to a smaller i.e better sensitivity. This sensitivity comes with a reduction in the spatial resolution of the trap as the atom cloud occupies a larger area in the transverse direction. It also leads to a decrease in the chemical potential and therefore a decrease in the range of measurable magnetic fields. This is summarised below in figure 6.3.

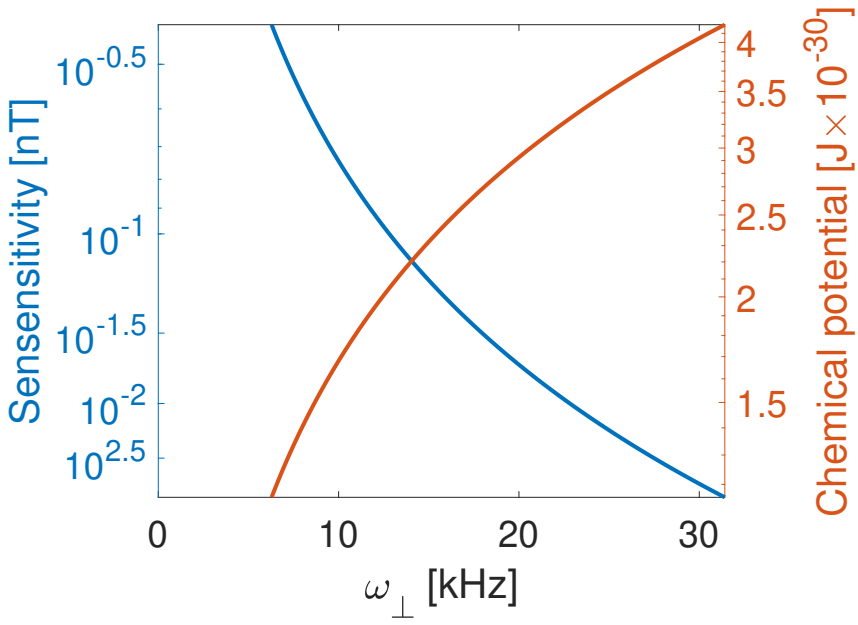

Figure 6.3: Figure showing how the chemical potential and sensitivity change depending on transverse trapping frequency $\omega_\perp$. The left plot shows that the sensitivity improves when $\omega_\perp$ decreases. The right plot shows that the chemical potential decreases when $\omega_\perp$ decreases. The decrease in chemical potential decreases the range of magnetic fields that can be measured by the BEC. By tuning $\omega_\perp$ we can control the sensitivity to magnetic fields and range of magnetic fields that can be measured by the BEC-M.

6.3 Comparison of sensitivity and responsivity

Both thermal atoms and a BEC can be used as a magnetic microscope using the regime presented above. Choosing which to use depends on the measurement being made. In table 6.1 we compare some scaling parameters of the two magnetometers.

	Thermal atoms	BEC
Atom number	$\Delta B \propto N$	$\Delta B \propto N^{-\frac{2}{5}}$
Temperature	$\Delta B \propto T^{\frac{3}{2}}$	-
$\omega_\perp$	-	$\Delta B \propto \omega_\perp^2$
Radial Size	$\sim 10\,\mu m$	$\sim 1\,\mu m$

Table 6.1: A summary of the how the sensitivity of the BEC-M and thermal cloud scales with different experimental properties.

The sensitivity of the thermal cloud is improved by reducing the temperature of the atom cloud. Cooling the atom cloud too far can lead to the atoms condensing into a

Bose-Einstein condensate.

6.4 Other methods of measuring current paths

Whilst this section has looked extensively at the BEC-M there are other methods for measuring the magnetic and the magnetic fields from silver nanowires. The list of methods is not exhaustive but covers the major competitors to the BEC-M. The measurement of currents from the silver nanowire network by the BEC-M are covered in the next chapter.

6.4.1 Conductive atomic force microscope

The conductive atomic force microscope (CAFM) is a variant mode of the atomic force microscope. The CAFM measures both the height and current flow between the tip and the surface of the sample [Lanza, 2017]. The CAFM does not directly measure the current but instead creates a conductivity map that measures the conductivity of a sample ground electrode [Shaw et al., 2016]. When using the CAFM on silver nanowires the conductivity measurement can lead to dead sections of nanowires appear to conduct current where a direct current measurement would show otherwise. The spatial resolution of the CAFM is set by the tip size [Shaw et al., 2016]. The average tip size for CAFM is $\sim 20\,\text{nm}$ which gives a much higher resolution that the BEC-M which is diffraction-limited to $\sim 780\,\text{nm}$.

6.4.2 Thermal imaging

By measuring the thermal radiation from the silver nanowires current paths can be directly measured. Direct measurement of the current paths in silver nanowires using a thermal microscope has been demonstrated by [Sannicolo et al., 2016]. The microscope used an InSb camera with 640×512 pixels with each pixel being $15\,\mu\text{m}$. The system has a $10\,\mu\text{A}$ current sensitivity. One issue with the thermal imaging is the relatively high currents needed for the camera to detect the thermal radiation.

6.4.3 Nitrogen vacancy centres

Nitrogen vacancy centres (N-V centres) are another method used to measure microscopic magnetic fields. N-V centres have not been used to directly measure current paths in silver nanowires. In a paper by Jean-Philippe Tetienne et al [Tetienne et al., 2017] N-V centres were used to measure the current flow in a sheet of graphene. The N-V centre was able to achieve a current sensitivity of $20\,\text{nA}$ with a spatial resolution of $50\,\text{nm}$. The

spatial resolution exceeds what the BEC-M can achieve, however, the BEC-M is an order of magnitude more sensitive. The image acquisition time for the N-V centres is on the order of hours.

6.5 Conclusion

The scaling behaviour of the thermal and BEC magnetometers responsivity is dependant on the magnitude of the external field compared to a characteristic energy scale of the magnetometer. For thermal atoms, the energy scale is set by the temperature of the atom cloud. At large magnetic fields, the responsivity of the thermal atoms asymptotically approaches zero. In practice, the limit on the number of detectable atoms will set an upper bound for the measurable magnetic field. The energy scale of the BEC is set by the chemical potential μ. The responsivity of the BEC changes linearly until the magnetic energy equals the chemical potential, $\mu_b B_{ext} = \mu$. At this point, all the atoms have been removed from that part of the trap and any increase in the magnetic field can not be measured.

To summarise, thermal atoms can be used to measure larger magnetic fields ($\sim 1\,\mu\mathrm{T}$) at the cost of sensitivity and spatial resolution due to the larger width of the cloud. The BEC-M can measure smaller magnetic fields and has a better spatial resolution than the thermal cloud. This comes at the cost of a smaller dynamic range of measurable magnetic fields.

Chapter 7

Bose-Einstein condensate microscope simulations

7.1 Introduction

In the last chapter, we showed that ultra-cold atoms can be used as sensors for microscopic magnetic fields. In this chapter, we will simulate a Bose-Einstein condensate (BEC) above a random network of silver nanowires. We will show that the BEC can measure the magnetic fields generated by the current in the silver nanowires and that we can use this measurement to reconstruct the currents in the silver nanowires. As we discussed in the introduction the need for transparent conductors has grown at a rapid pace over the last few years as it is used in solar panels and touch screens. Currently the majority of transparent conductors are made using indium tin oxide (ITO). Currently the price of indium is increasing, as of 2019 the price of indium was $390 which was 4% more than 2018 [USGS, 2020]. 36% of indium was sourced in china [USGS, 2020]. To solve these political and economic issues there is considerable research into alternate transparent conductors [Kumar and Zhou, 2010]. Silver nanowires could be a strong candidate to replace ITO as a transparent conductor[Van De Groep et al., 2012]. In this chapter, we will begin by describing how the silver nanowire networks are simulated. We will then describe the method for calculating the current distribution in the nanowire network using graph theory. We will then calculate the magnetic field generated by the silver nanowires using an analytic method. This method assumes that the silver nanowires are infinitely thin with a finite length. Next, we use the results from chapter six to simulate the BEC in an Ioffe-Pritchard trap with the external magnetic perturbations from the silver nanowires. Measuring the density distribution of the simulated BEC we can recover a 1d magnetic field distribu-

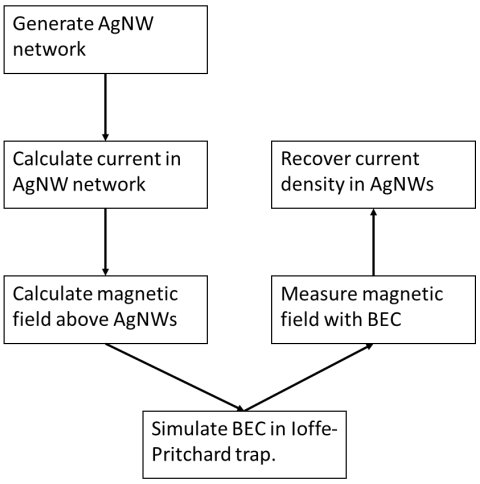

Figure 7.1: Flow chart showing the order of simulation. We can compare the results of sections on the same level. For example, we can compare the magnetic field from the nanowires that has been calculated analytically to the magnetic field measured by the BEC.

tion. By scanning the BEC over the network we build up a 2d image of the magnetic field above the silver nanowires. Finally, we will use an inverse method that is outlined in more detail later in the chapter to recover the current density in the silver nanowires. The order of calculations is summarised in 7.1. Usually calculating currents in complex systems we use Kirchhoff's laws [Balberg et al., 1983, Mutiso and Winey, 2013]. Due to the large number of connections, it is difficult to solve the system of equations by hand. Instead, we turn to graph theory and a gradient descent method to calculate the current in the silver nanowires. We will go into more detail later in the chapter. The magnetic fields generated by the current in the silver nanowire network are calculated analytically using a method outlined in [Barrett, 2017]. Once we have described the simulation we will the go on to present the results obtained using this simulation. These include simulations of silver nanowires at a range of different wire densities that are characterised by the transmittance of the network and the re-construction of the current using the BEC-M. We will also present height and current data that was taken by a conductive atomic force microscope (CAFM). We use this data to construct a network of straight wires that approximate the real data. From this, we calculate a measurement of the magnetic fields by the BEC-M and compare this to the conductivity map taken by the CAFM.

7.2 Simulating the nanowire network

In this section, we will describe in detail the process used to generate the nanowire networks. We will then go on to show how fixing the transmittance of the nanowire networks to defines the number of wires in the network. We show how the wire crossings are calculated. Finally, we go into graph theory to show how the currents in the nanowire networks are calculated.

7.2.1 Randomly generated nanowire networks

We first define a domain in which the nanowires are allowed to be generated. Then we choose the number of nanowires, which depends on the chosen optical transmittance of the nanowires. This is covered in more detail in section (7.2.3). For each nanowire, we randomly generate an x and y co-ordinate for one end of the nanowire within the bounded region. We then randomly generate an angle from $0-2\pi$ sampled from a uniform distribution and a length which is chosen from a log-normal distribution see figure (7.2b). Using the angle and length we define the coordinates of the other end of the silver nanowire. The second end can leave the domain but is limited by the length of the nanowire. If we were to force all the wires to be within the defined region we could induce edge effects that can produce anomalous results in the simulations. The domain in which the nanowires can be generated is much larger than the length of the nanowires. We define $\langle L \rangle$ as the mean length of the nanowire and σ is the variance in the length of the nanowires. At the top and bottom of the nanowire network, we add a long wire that spans the width of the domain (see fig (7.2a)). These wires simulate the electrodes through which current is passed.

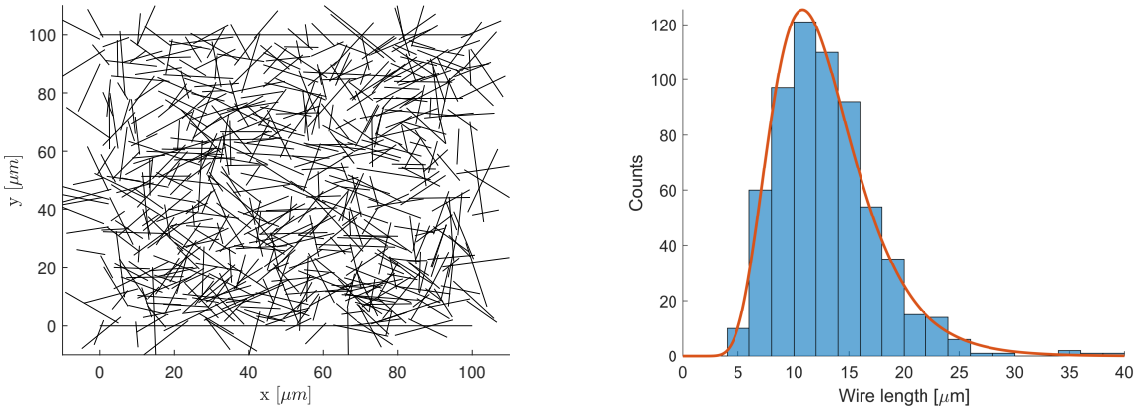

(a) (b)

Figure 7.2: (a) An example set of nanowires. The straight wires at $y = 0\,\mu\text{m}$ and $y = 100\,\mu\text{m}$ are added non-randomly and represent as electrodes. These wires define the start and endpoints for the current flow. (b) Distribution of the lengths of the silver nanowires. As there can not be negative length nanowires the distribution bunches up towards zero. In this case $\langle l \rangle = 12.6\,\mu\text{m}$ and $\langle \sigma \rangle = 4.6\,\mu\text{m}$ and there are a total of 622 wires.

7.2.2 Percolation theory

Percolation theory describes many properties of random networks such as we find in silver nanowires [Mertens and Moore, 2012]. The exact properties of the network depend on the shape of the constituent particles, for example, many of the constants are different for a network of thin sticks and spheres [Ni et al., 2018]. Given the nanowires have no length we estimate the nanowires density measure as [Large, 2016],

$$\eta = \frac{1}{A} \sum_{i}^{n} l_i^2. \tag{7.1}$$

Here A is the area of the domain, l_i is the length of the ith wire and N is the total number of wires. η is a measure of the fractional area the nanowires cover. As the nanowires in the simulation are one dimensional the area covered by a nanowire is taken to be a square with side length l, where l is the length of the nanowire. There is a critical density η_c, when the density of the network η is greater than the critical density we can expect connectivity over a long-range and when the density is less than the critical density we can expect some local connectivity but no connectivity over the whole network. For silver nanowires the critical density $\eta_c = 5.63726$ [Li and Zhang, 2009]. When the density of nanowires is similar to the critical density the network is at the percolation threshold. At a density above the percolation threshold the connectivity of nanowire network extends over large distance.

7.2.3 Transmittance

The density of a nanowire network can be measured by amount of light that passes through the nanowire network. This is called the transmittance of the nanowire network and is given by

$$T = 10^{-Q_{ext}\phi_s}. \tag{7.2}$$

Here T is the transmittance and is defined by two factors Q_{ext} and ϕ_s. Q_{ext} is the extinction efficiency of light on the nanowires [Haverkate and Feiner, 2006]. Q_{ext} depends on the interaction between the nanowire and the incident photons, Q_{ext} therefore depends on the thickness of the nanowire and the frequency of the incident photon. For this work we used the values given in [Large, 2016] which are $Q_{ext} = 0.3$ for $d = 30\,\text{nm}$ and $Q_{ext} = 1.6$ for $d = 120\,\text{nm}$ where d is the thickness of the nanowires. In equation (7.2), ϕ_s is the area fraction of the surface covered by silver nanowires. We can express ϕ in terms of the length and number of the nanowires and the are of the defined region,

$$\phi_s = \frac{N\langle L\rangle d}{A}. \tag{7.3}$$

Here N is the number of wires, as before $\langle L\rangle$ is the average length of the wires, d is the thickness of silver nanowires and A is the domain area. We can rearrange this equation so that we can define the desired transmittance and use that to calculate the number of nanowires required to achieve that transmittance.

$$N = -\frac{A}{d\langle L\rangle Q_{ext}} log_{10}(T) \tag{7.4}$$

7.2.4 Calculating wire crossings

Now that we have generated the silver nanowires, we calculate the crossing points between wires. There are several methods for doing this such as the Bentley-ottoman algorithm [Bartuschka et al., 1997] and the box-counting method [Li and Zhang, 2009]. For these simulations, we use a brute force method that compares each wire with every other nanowire. This method scales as $\mathcal{O}(N^2)$ where N is the number of nanowires, which is not optimal. However, the calculation of the magnetic fields from the nanowires takes much longer than any other calculation in the simulation therefore the time taken to calculate the wire crossings is negligible. To detect if two wires cross we define each wire as a unit vector. As long as the wires are not parallel the crossing point will occur when

$$a\vec{r_1} = b\vec{r_2}. \tag{7.5}$$

Here r_1 and r_2 are the vectors of the nanowires, a and b are both numerical constants. We can solve the equation for a and b. There are three different cases depending on the values of a and b and are covered below in figure (7.3).

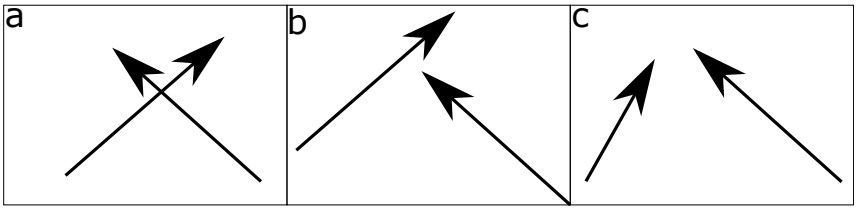

Figure 7.3: Figure showing the three-wire crossing cases a.) Case one: the wires cross in this case both a and b are less than one. b.) Case two: the wires do not cross but one of a or b is less than one. c.) Case three: the wires do not cross and both a and b are greater than one.

We then check if each nanowire is connected to the bottom electrode. Any wire not connected to the ground electrode is removed from the list of crossings as these nanowires will not be carrying current. If the second electrode is not in the list of connected wires then we know that the current does not flow across the region.

7.3 Generating currents in the nanowire network

The distribution of current in a grid of resistors is usually solved using Kirchhoff's laws [Feynman, 1964]. Calculating every current path between two points is an NP-hard problem which means that the problem scales exponentially. Instead, we will use graph theory to calculate the potential at each wire intersection. In this section, we will go through in steps the process to calculate the potential and current flow across the network.

7.3.1 Nanowire resistance

In the silver nanowires networks, there are two sources of resistance. First, the resistance from the bulk of the nanowire, the resistivity of a silver nanowire with a 30 nm diameter is $\rho = 1.59 \times 10^{-8} \Omega\,\mathrm{m}$ [Griffiths, 1962, p. 301]. For a nanowire with a diameter of 30 nm gives a resistance per unit length of $22.35\,\Omega\mathrm{m}^{-1}$. The second source of resistance comes from the contacts between two silver nanowires, this resistance is called the junction resistance and is studied in [Li and Zhang, 2010, Garnett et al., 2012]. In the simulations, we set the junction resistance to $100\,\Omega$ to be in line with the calculations in [Bellew et al., 2015]. The simulation of the junction resistance can be made more complex however this would

not add to these simulations and so were left out.

7.3.2 Graph theory

Graph theory is well covered in the literature [West et al., 1996] but we will be following the method outlined in [Large, 2016]. To better convey the ideas in this section we will use the case of one wire crossing the two-wire electrodes shown in figure (7.4a). First, a graph is a mathematical object constructed of nodes and edges. An edge connects two nodes and can have a weighting, edges can also be directional but this is not needed for the problem at hand. The node of a graph is formed when two or more edges meet. The value of a node is given by the sum of the weights of the edges that connect to the node. The degree matrix is a matrix that has a lead diagonal comprised of the weights and is zero elsewhere. The weighting of the edges is defined as,

$$w = \frac{1}{R}, \tag{7.6}$$

here R is a resistance. As mentioned in the section above there are two sources of resistance, the bulk resistance of the nanowire and the resistance of the junction. This information is stored in the so-called adjacency matrix. An adjacency matrix is a square matrix of size N where N is the number of nodes. The adjacency matrix is a representation of the connection of each node with each other node and the weighting of w.

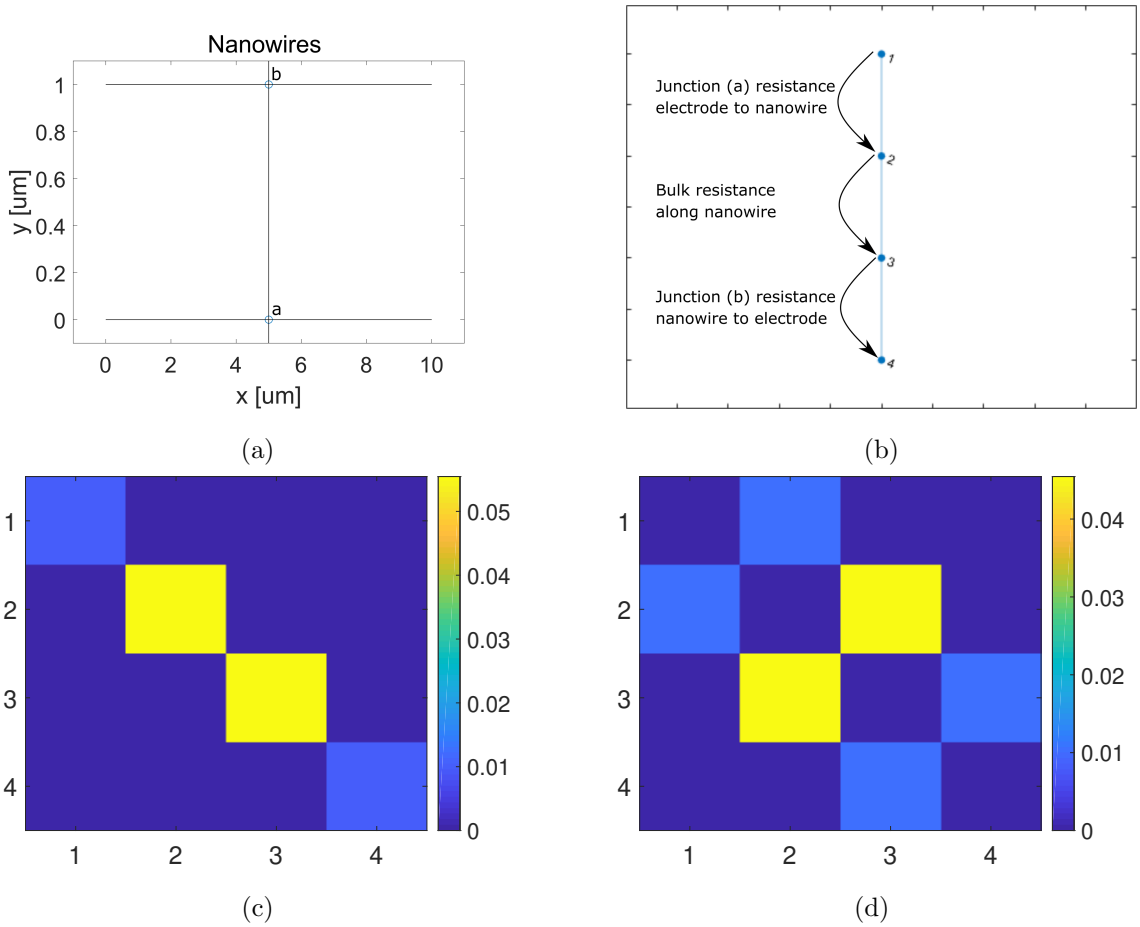

Figure 7.4: (a) A three wire network with two electrodes, top and bottom, and one nanowire connected to each electrode at (a) and (b). (b) The graph of the wire network shown in figure (a). The black arrows have been added to indicate the connection each edge of the graph represents. The edge from 1 to 2 represents the junction resistance between top electrode to the wire at (a) on figure (a). The edge 2-3 represents the resistance that arises from the wire between (a) and (b) on figure (a). The edge 3-4 represents the junction resistance between the wire and the bottom electrode at (b) on figure (a). (c) Visualisation of the degree matrix for the demonstration problem. The degree matrix is a square matrix size N, the only non zero terms are on the lead diagonal. (d) Adjacency matrix for the corresponding graph. The wire has a lower resistance than the junctions and therefore has a higher weighting.

We can combine the adjacency matrix and the degree matrix into what is known as the Laplace matrix which is defined as,

$$\mathcal{L} = D - A. \tag{7.7}$$

Here D is the degree matrix and A is the adjacency matrix. In the example case, we find

$$\mathcal{L} = \begin{pmatrix} 1/100 & -1/100 & 0 & 0 \\ -1/100 & (1/22 + 1/100) & -1/22 & 0 \\ 0 & -1/22 & (1/22 + 1/100) & -1/100 \\ 0 & 0 & -1/100 & 1/100 \end{pmatrix} \tag{7.8}$$

We can now use the equation,

$$\mathcal{L}\vec{v} = \vec{i}, \tag{7.9}$$

to solve for the potentials across the wires. Equation (7.9) is effectively Kirchhoff's laws expressed in matrix form. Here $\vec{i}$ is a list of sources and sinks in the network. We define the problem to only have one source (the input on the bottom electrode) and one sink (the output on the top electrode).

To solve for $\vec{v}$ we use an inbuilt MATLAB function call preconditioned gradient decent (PCG). This method attempts to minimise the residuals when solving equation (7.9). When the number of nodes becomes large the Laplace matrix also becomes large. The Laplace matrix lends itself to a sparse representation. The current along an edge is given by the difference in voltage in the nodes divided by the resistance of the wire $I = V/R$ otherwise known as Ohm's law.

7.3.3 Calculating magnetic fields

We calculate the magnetic fields from the silver nanowires in a volume above the nanowire network where the BEC is simulated. For each wire in the network, i.e wires that carry current, we calculate the magnetic field at each of the points in the 3d grid. We used the Biot-Savart law and a method outlined in [Barrett, 2017] to calculate the magnetic field from an infinitely thin wire. The vector components of the magnetic fields are summed to create a final magnetic field map for the silver nanowires. The junctions between nanowires do not generate a magnetic field.

7.4 Inverse methods

We want to recover the current density from the silver nanowires, in this section, we present the method to calculate the current density from the measured magnetic field. The magnetic field generated by a current density $J(r)$ is given by the Biot-Savart law,

$$B(r) = \frac{\mu_0}{4\pi} \int \frac{J(r') \times (r - r')}{|r - r'|^3} d^3r'. \tag{7.10}$$

The magnetic field is given by a convolution of the current density with a propagation function called the Greens function. In this case the Greens function is defined as ,

$$G(x-x',y-y',z)=\frac{\mu_0 d}{4\pi}\frac{1}{[(x-x')^2+(y-y')^2+z^2]}. \tag{7.11}$$

Here, d is the thickness of the medium the current is flowing in. We have set the surface of the current medium at $z'=0$. The Greens function smooths $B(r)$ proportionally to the distance from the current source. To calculate the current density from the magnetic field we solve the inverse problem. When the current density is unconstrained the inverse problem is ill-defined due to there being multiple solutions valid solutions for a given magnetic field distribution. When the current density is confined in one direction the inverse problem becomes well defined with a unique solution. We will use the coordinate system shown in figure (7.5).

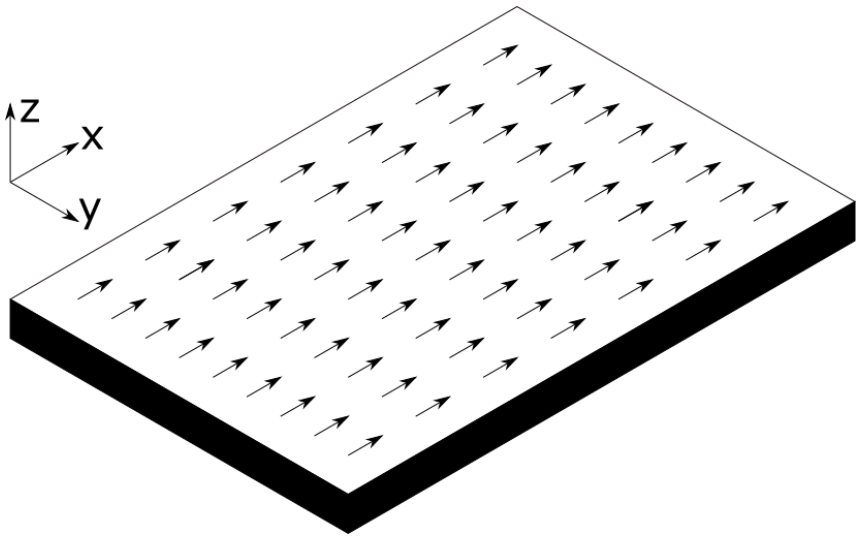

Figure 7.5: Uniform current flowing in the x-direction, represented by arrows, which generates a magnetic field in the y-z direction. Perturbations in the direction of the current flow generate a magnetic field in the x-z direction. Whilst there is no current flow in the z-direction the current can still fill the medium which has a thickness d.

Here we will show the method used to solve the constrained inverse method, the majority of the method is covered by Roth et al in [Roth et al., 1989]. I will add some comments and additions where necessary. We begin by considering the magnetic field in the x direction which is given by,

$$B_x(x,y,z)=\frac{d\mu_0}{4\pi}\int_{-\infty}^{\infty}\int_{-\infty}^{\infty}\frac{J_y(x',y')}{[(x-x')^2+(y-y')^2+z^2]^{\frac{3}{2}}}\times dx'dy'. \tag{7.12}$$

Here d is the thickness over which the current is flowing. As there is no current in the z direction the $J_z(r)y$ component of the cross product is zero. As this is a convolution it is

easier to solve this problem in Fourier space. The convolution in Fourier space is given by,

$$b_x(k_x, k_y, z) = g(k_x, k_y, z) j_y(k_x, k_y, z), \tag{7.13}$$

where b,j and g represent the Fourier transform of the magnetic field (B), current density (J) and greens function (G) respectively. Fortunately the Fourier transform of the greens function has an analytically solved [Gradshteyn and Ryzhik, 2014].

$$g(k_x, k_y, z) = \left(\frac{\mu_0 d}{2}\right) e^{-z\sqrt{k_x^2+k_y^2}}. \tag{7.14}$$

Here d is the thickness of the medium in which the current flows. We therefore recover the current density J_y by

$$J_y = \mathcal{F}^{-1}\left(\frac{b_x(k_x, k_y, z)}{g(k_x, k_y, z)}\right). \tag{7.15}$$

Where $\mathcal{F}^{-1}$ indicates the inverse Fourier transform. This is true so long as $g(k_x, k_y, z) \neq 0$ as $J_y(r)$ would become undefined. We assume that the current flow is conserved such that $\nabla J(r) = 0$, this is expressed in Fourier space by,

$$-ik_x j_x(k_x, k_y) = ik_y j_y(k_x, k_y). \tag{7.16}$$

Using this result it is possible to recover $J_x(r)$ for a measurement of $B_x(r)$ using,

$$J_x(r) = \mathcal{F}^{-1}\left(\frac{2k_y}{\mu_0 dk_x} e^{\sqrt{k_x^2+k_y^2}z} b(k_x, k_y, z)\right). \tag{7.17}$$

7.4.1 Filtering

Due to numerical errors and noise, it is necessary to apply a filter to j_y before using the inverse Fourier transform to recover J_y. We chose to use the Hann window to filter the signal due to the minimal impact on resolution. The Hann window is defined as,

$$w[k] = \begin{cases} \frac{1}{2}[1 + cos(\frac{\pi k}{k_{max}})], & k < k_{max} \\ 0, & k > k_{max} \end{cases} \tag{7.18}$$

The cut-off frequency k_{max} sets the largest spatial frequency included when reconstructing the current density. As the distance between the measured point and the current density sets the length scale in the Greens function we can set the maximum spatial frequency to be separation z where $k_{max} = 2\pi/z$.

7.5 Inverse method examples

Here we look at some examples of the inverse method at work. The first example demonstrates that the inverse method can recover the magnitude of the current density in ideal

conditions. The second example introduces noise into the equation and shows how accurate our filter approximation is.

7.5.1 Single wire

Here we show that the inverse method can recover the current density for a single wire. First, we generate a single wire with a finite width and height. The current flows in the y-direction so that the magnetic fields are generated in the B_x direction.

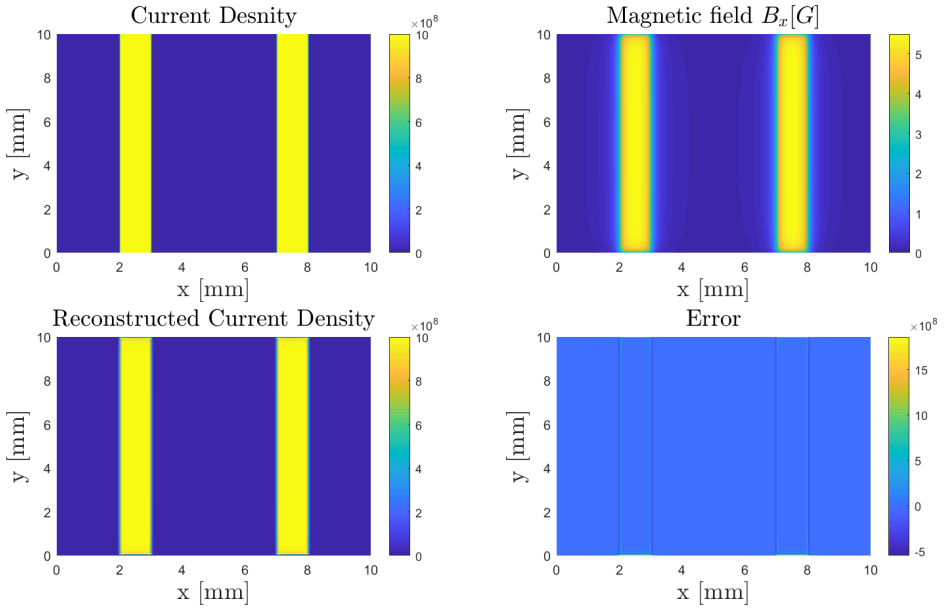

Figure 7.6: Top left: Current density in a pair of rectangular wires 10 mm long, 1 mm wide and 1 µm thick. Top right: Magnetic field measured at a height of 100 µm above the wire. Bottom left: Reconstructed current density. Bottom right: Difference between initial and measured current density. The error is largest around the edges of the wires due numerical errors that arise from the Fourier transform of a square top hat function.

The inverse method works well when there is no noise. Once we introduce noise into the system it becomes impossible to recover the exact underlying current density. Instead, we can only look at the quality of the recovered image. When the initial current density is known we can calculate the mean square error (MSE) and mean square deviation (MSD). The mean square error is the squared difference between the measured current density $J(x, y)$ and the reconstructed current density $J_r(x, y)$.

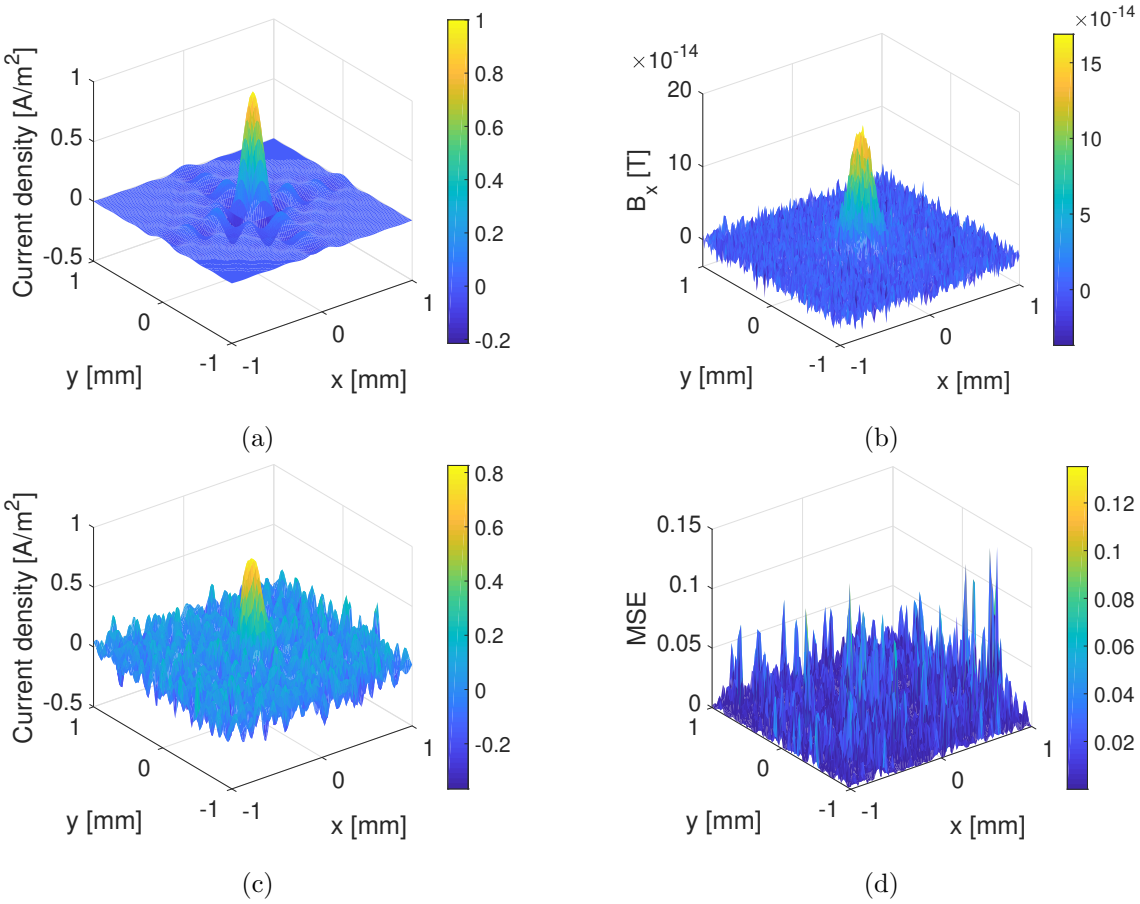

Figure 7.7: (a) Initial current density distribution is $J(x,y) = sinc(\omega_x X)sinc(\omega_y Y)$ where ω_x and ω_y set the length scale of the oscillations . (b) Magnetic field calculated from the current density at a height of 100 µm above the current density. The magnetic field was calculated by solving the forward problem and then normally distributed noise was added to the magnetic field. (c) Reconstructed current density from the magnetic field. The maximum allowed frequency by the Hann window was $k_x = k_y = 2\pi/z$ in this case $d = 100\,\mu m$. Note that the noise has been smoothed out, however, the noise has drowned out the 2nd peaks from the sinc function. (d) The mean square error (MSE) between the original current density and the calculated current density.

The mean squared deviation is given by,

$$MSD = \frac{\iint |J(x,y) - J_r(x,y)|^2 dxdy}{\iint |J(x,y)|^2 dxdy}, \tag{7.19}$$

and represents a single value that indicates how much the reconstructed current density deviates from the current density. When using an image the current density is discretized so the integrals are replaced by summations.

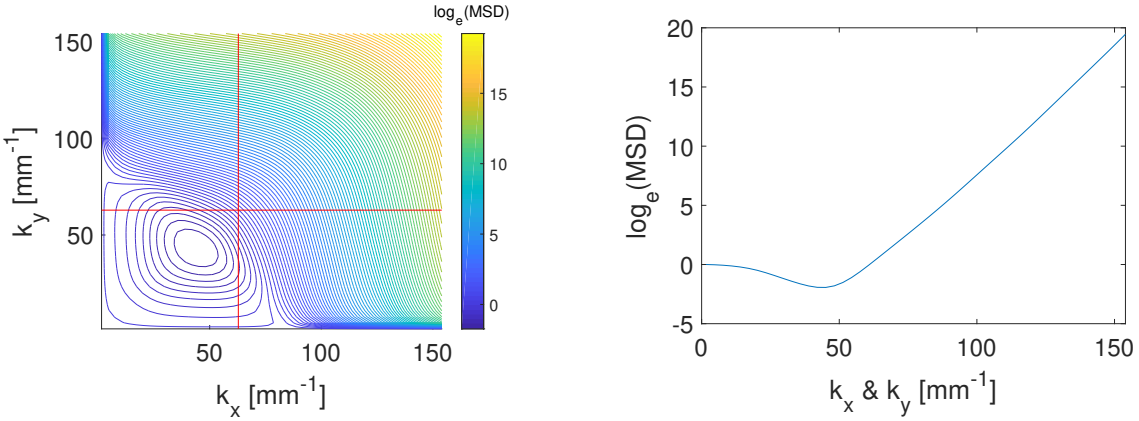

(a) (b)

Figure 7.8: (a) A two dimensional scan of the mean square error as a function of k_{xmax} and k_{ymax}. We take the log of the MSE to scale the plot. The red lines indicate where k_{xmax} and k_{ymax} are equal to $2\pi/z$. (b) A cut along the line $k_x = k_y$ to highlight the shape of the surface in plot (a).

In figure (7.8a) we compared how our estimation for the ideal cutoff frequency compares to the calculated ideal cutoff frequency for the filter. For these conditions we overestimated the optimal cutoff frequency, however, the difference between the estimated cutoff frequency and the optimum cutoff frequency is small enough to be acceptable. This global minimum depends on the relative magnitude of the noise to the signal. The smaller the signal to noise ratio the closer the minimum moves towards $k_x, k_y = 0$. Whilst our approximation that the ideal filter size is $2\pi/z$ isn't perfect it is a reasonable first guess.

7.6 Results

In this section, we will show the results of the BEC-M simulations near silver nanowire networks. We will begin by comparing BEC-M simulations to CAFM data taken by Dr Manoj Tripathi for this purpose. We will then show the results of using the BEC-M on simulated nanowire networks with a range of wire densities set by the transmittance.

7.6.1 Simulations with CAFM data

The CAFM was used to measure a portion of a silver nanowire network. The nanowires in the network have a diameter of 120 nm. The CAFM was scanned over a 10 µm × 10 µm region and recorded the height and conductivity of the nanowire network. Results of the scan are shown below in figure (7.9a) and (7.9b).

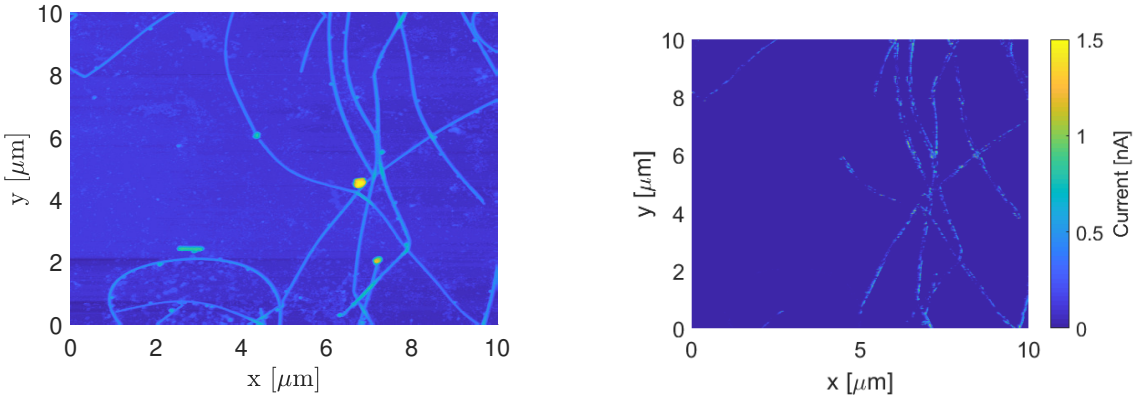

(a) (b)

Figure 7.9: (a) Height data of the silver nanowire network as taken by AFM. (b) Conductivity map of the silver nanowires. Note that the curved section lower left has a much lower conductivity ($\sim 0.1\,\mathrm{nA}$) than the majority of the nanowire network.

To simulate the current paths in this network we create an approximate the network made of straight wires as shown below in figure 7.10.

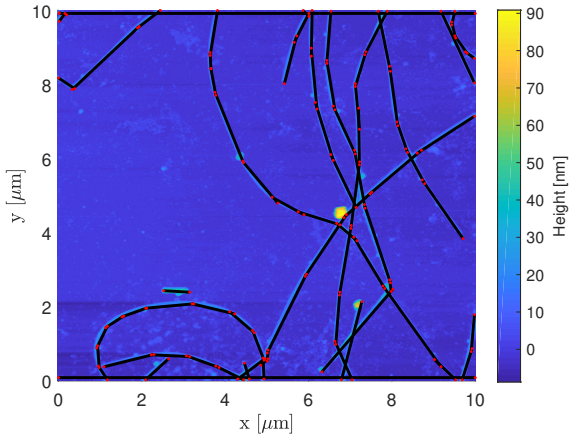

Figure 7.10: Figure showing the straight wire approximation overlaid on the height data. The start and endpoints of the wires are marked in red. Wires spanning the sample top and bottom were added to simulate electrodes.

The start and endpoints of the wires were chosen manually. We used the method outlined above to calculate the current in the wires starting from the bottom electrode to the top electrode. We used the same values for the resistance of the wires and junctions as given in the method. We then calculated the magnetic field 100 nm above the nanowire network.

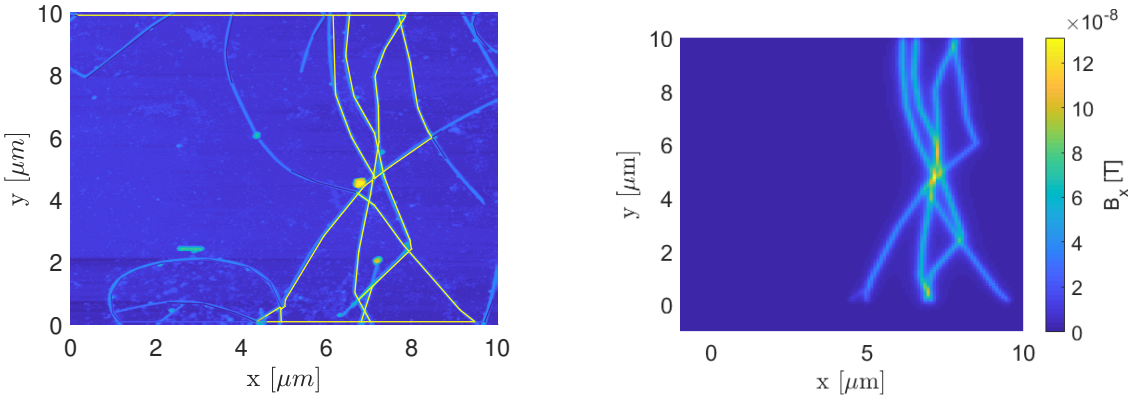

(a) (b)

Figure 7.11: (a) Wires with current are shown overlaid on the CAFM height map data. The input current in the bottom electrode is 100 nA. (b) X component of the magnetic field measured 100 nm above the nanowire network. At 100 nm the magnetic field closely follows the shape of the wires.

We then simulate a BEC 100 nm above the nanowire network. It was shown in [Sinuco-León et al., 2018] that a surface to BEC distance of 100 nm is possible. By measuring the changes in the density distribution of the BEC we recover a current density distribution that we can compare to the conductivity map taken with the CAFM. Whilst these two values are not directly comparable it is worth looking at some key differences between the two measurements.

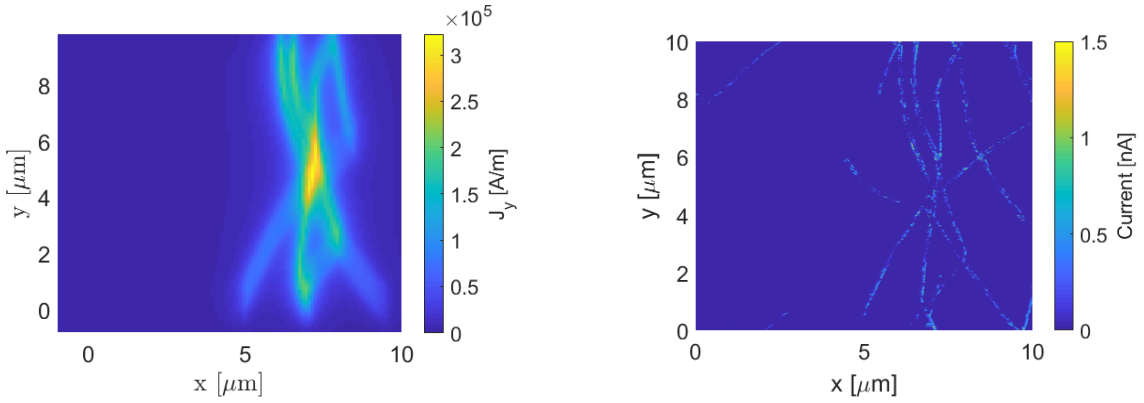

(a) (b)

Figure 7.12: (a) Simulated current density measured by the BEC-M. There has been some spreading of the predicted current density due to the finite width of the BEC. (b) Conductivity as measured by the CAFM. There are some areas in the CAFM data that do not appear in the BEC-M data. These parts of the network are connected to ground but do not carry current. This is most visible in the top left of the CAFM data where there is a conductive wire with no corresponding current density.

In the top left corner of the CAFM data fig (7.12b) we can see where the nanowire was connected one of the electrodes. In the corresponding BEC-M image fig (7.12a) we don't see any current measured. This highlights one of the major advantages of using the BEC-M to measure current paths. In figure (7.12a) we see that there a region of increased current density in the network. These areas of higher current can be indicative of hot spots in the nanowire network. Hot spots can be an indication of where the network can fail due to thermal effects. It is possible that the BEC-M can be used to measure the location of hot-spots in these networks.

7.6.2 Silver nanowire network

Here we show the results from simulations of silver nanowire networks with three different densities and optical transmittance. In these simulations, we set the nanowire thickness to be 120 nm. At a transmittance of 93% the network is below the percolation threshold. To ensure a network that connected the two electrodes we generated networks until a valid network was found. The BEC was scanned at a height of 1 µm above the nanowires and was scanned along from $y = 0$ µm to $y = 100$ µm with a 2 µm spacing.

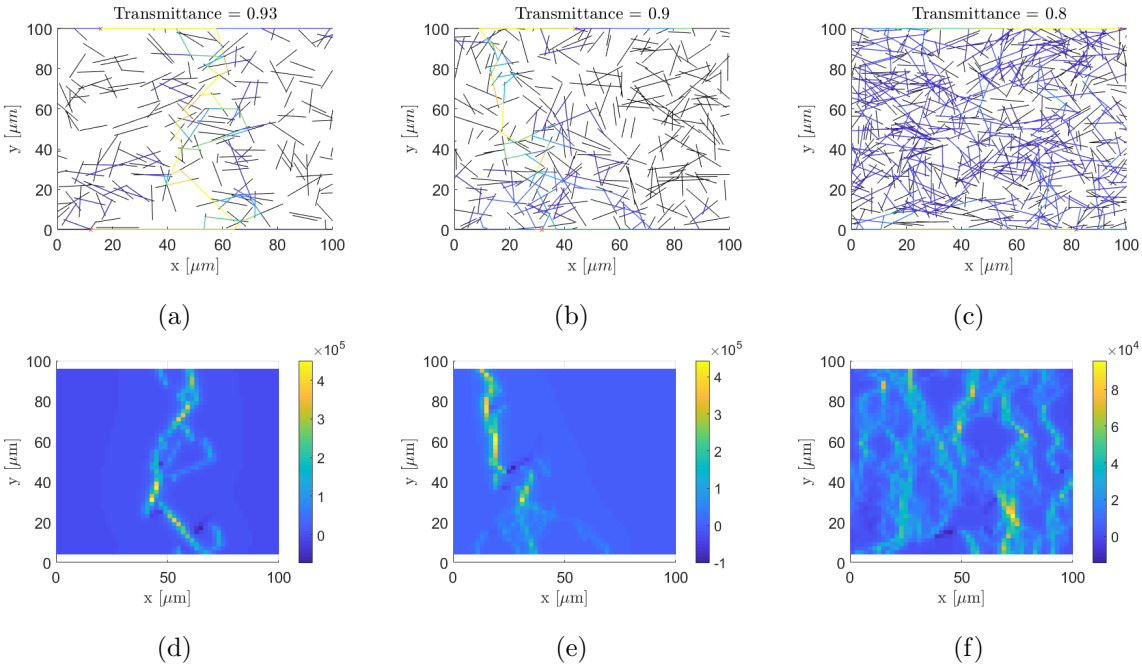

Figure 7.13: Figures (a),(b) and (c) show nanowire networks with a transmittance of 93%, 90% and 80% respectively. The wires are coloured depending on the relative current in each wire. Black wires have zero current. Figures (d),(e) and (f) show the reconstructed current densities from their respective networks. The input current was 1 µA. The trapping potential was $[\omega_\perp, \omega_\parallel] = 2\pi \times [3\,\mathrm{kHz}, 1\,\mathrm{Hz}]$. The trapping potential was chosen to minimise the curvature of the trap over the 100 µm imaging length.

In the above figures, we can see that at low density it is possible to make out individual wires. At higher densities, this becomes less clear however even at the 80% case still possible. In the 90% case we can see the current merging from several wires. In all 3 current density maps, there are sections where the current flows in the negative y-direction. This shows that the BEC-M can measure the current direction as well as the magnitude. These areas appear as dark patches on the figures. In the 80% case we can see a hot spot in the current in the lower right quadrant of the figure. This seems to indicate that even when the silver nanowire density becomes so large that we are measuring the sheet resistance hot spots in the current path will still be resolvable.

7.7 Conclusion

In this chapter, we outlined a method to simulate the current flow in the silver nanowire networks. We then went on to demonstrate how the two-dimensional inverse problem could be solved analytically. We also showed the effect of filtering has on recovering noisy data

and proposed a simple way to generate an upper bound in frequency space for the filter. We then went on to compare different methods of measuring current flow or conductivity in silver nanowire networks and how these methods compared to the BEC-M. Finally, we showed the results of the silver nanowire simulations, first with data taken by CAFM and then on simulated random networks.

Chapter 8

Summary and outlook

In chapter two we gave a theoretical description of the interaction between light and a two-level atom. We then went on to use this description to build a simple model for laser cooling and trapping of atoms. In chapter three we used the methods outlined in chapter two to derive a theoretical model for the two colour magneto-optical trap (TCMOT). We predicted that the TCMOT should have a lower scattering rate than a single colour MOT with the same intensity of incident laser light. The prediction of a lower scattering rate and therefore lower force from the cooling beams in the TCMOT motivated the push beam experiment in chapter five. We also predicted that the TCMOT should have a lower capture velocity than the single colour MOT, however, this prediction was not verified experimentally in chapter five. In Chapter four we show the experimental setup and describe the processes we used to optimise the experiment. In chapter five we presented the results from the TCMOT experiment. We found a maximum increase of six times in atom number along with an increase in the size and temperature of the MOT. We then presented a method to recover the phase space density of the TCMOT while retaining the increased atom number. The measurement of the spring constant and damping coefficient showed that both the spring constant and damping coefficients reduced with the TCMOT with the minimum value of the coefficients at a relative detuning of $\delta = \Gamma/2$. This reduction implies that the scattering rate decreases for the TCMOT. This is in agreement with the theoretical predictions given in chapter three however the theory fails to predict a minimum scattering rate at $\delta = \Gamma/2$.

In chapter six we show how both ultra-cold thermal atoms and a Bose-Einstein condensate (BEC) can be used for magnetic microscopy. First, we showed that one component of the magnetic field of an external homogeneous field could be separated from the magnetic fields making up the magnetic trap. We then derived a relation between the atom

density and the external magnetic field for both thermal atoms and the BEC. Using this result we showed how the sensitivity and responsivity of the thermal atom cloud and the BEC differs and gave cases for when each could be used as a magnetometer. In chapter 7 we simulated the use of the BEC-M to recover current densities in silver nanowire networks. We showed that the BEC-M could be used for a variety of densities of the silver nanowires. We also compared the simulations of the BEC-M to CAFM data and highlighted the advantages to directly measuring the current in the silver nanowires as opposed to the conductivity.

8.1 Future work

8.1.1 Two colour theory

While we have shown that the TCMOT can be used as a useful tool for cold atom experiments, the theoretical understanding of the TCMOT is still missing some key components. Most notable is the failure of the theory to predict the relative frequency δ, at which the atom number is maximum. We will try to follow the dressed state picture for two rotating frames as outlined in [Saiko et al., 2014]. It is also worth looking into the results shown in (5.13) as it lies outside theoretical predictions and can act as a guide towards what is missing in the theoretical picture.

8.1.2 Bose-Einstein microscope experiment

Whilst chapter 6 and 7 look only look at the BEC-M theoretically, we are taking steps in our lab to realise the BEC-M experimentally. At the time of writing, we have modified the experiment shown in chapter 4. The top window of the vacuum chamber has been replaced with an electrical feed-through. On the feed-through, we have placed a new printed circuit board (PCB), similar in design to the one shown in [Gadge, 2018]. The PCB has a series of wires to trap and transport the atoms using magnetic fields from an optically bright area to the sample area. This allows the experiment to have samples that would otherwise be destroyed by or block the laser light used for magneto-optical trapping. On the PCB there is a range of samples including 3d printed wires, silicon nitride membranes and silver nanowire networks.

8.1.3 Inverse methods in three dimensions

In chapter 7 we showed that the inverse problem has a unique solution when the current density is confined to flow in two-dimensions. In real systems, currents are not confined in 2d, therefore, we need to consider currents in all directions. Being able to reconstruct currents in 3d has applications in a wide range of fields such as magnetoencephalography [Barnes et al., 2004], superconductors [Kirtley et al., 1996] and measuring current flow in novel materials [Langlois and Coeuret, 1989]. The magnetic field in each direction can be generated by currents in the two orthogonal directions. Therefore there is no unique solution to the inverse problem in three-dimensions. To solve the inverse problem we can use one of two methods. First, we can measure the magnetic field at a range of heights above the current flow region. The extra information gained from these measurements should allow for the solution space to be constrained to a unique solution. Alternatively, we can use a Bayesian inverse method. The Bayesian inverse method uses prior knowledge about the system to constrain possible solutions. An outline of Bayesian inverse methods can be found in [Stuart, 2010, Dashti and Stuart, 2016].

Bibliography

[Anderson et al., 1995] Anderson, M. H., Ensher, J. R., Matthews, M. R., Wieman, C. E., and Cornell, E. A. (1995). Observation of bose-einstein condensation in a dilute atomic vapor. *science*, pages 198–201.

[Balberg et al., 1983] Balberg, I., Binenbaum, N., and Anderson, C. (1983). Critical behavior of the two-dimensional sticks system. *Physical Review Letters*, 51(18):1605.

[Barker et al., 2019] Barker, D., Norrgard, E., Klimov, N., Fedchak, J., Scherschligt, J., and Eckel, S. (2019). Single-beam zeeman slower and magneto-optical trap using a nanofabricated grating. *Physical Review Applied*, 11(6):064023.

[Barnes et al., 2004] Barnes, G. R., Hillebrand, A., Fawcett, I. P., and Singh, K. D. (2004). Realistic spatial sampling for meg beamformer images. *Human brain mapping*, 23(2):120–127.

[Barrett, 2017] Barrett, T. J. (2017). *An apparatus for the production of Bose-Einstein condensates in tunable geometries on a chip*. PhD thesis, University of Nottingham.

[Bartuschka et al., 1997] Bartuschka, U., Mehlhorn, K., and Näher, S. (1997). A robust and efficient implementation of a sweep line algorithm for the straight line segment intersection problem. In *in proc. workshop on algorithm engineering*. Citeseer.

[Bason et al., 2009] Bason, M. et al. (2009). *Coherent atom-light interactions in multilevel systems*. PhD thesis, Durham University.

[Bellew et al., 2015] Bellew, A. T., Manning, H. G., Gomes da Rocha, C., Ferreira, M. S., and Boland, J. J. (2015). Resistance of single ag nanowire junctions and their role in the conductivity of nanowire networks. *ACS nano*, 9(11):11422–11429.

[Bergeman et al., 1987] Bergeman, T., Erez, G., and Metcalf, H. J. (1987). Magnetostatic trapping fields for neutral atoms. *Physical Review A*, 35(4):1535.

[Berman, 2014] Berman, A. (2014). *Total pressure measurements in vacuum technology*. Academic Press.

[Berthoud et al., 1998] Berthoud, P., Joyet, A., Dudle, G., Sagna, N., and Thomann, P. (1998). A continuous beam of slow, cold cesium atoms magnetically extracted from a 2d magneto-optical trap. *EPL (Europhysics Letters)*, 41(2):141.

[Bradley et al., 1997] Bradley, C. C., Sackett, C., and Hulet, R. (1997). Bose-einstein condensation of lithium: Observation of limited condensate number. *Physical Review Letters*, 78(6):985.

[Brink and Sukumar, 2006] Brink, D. and Sukumar, C. (2006). Majorana spin-flip transitions in a magnetic trap. *Physical Review A*, 74(3):035401.

[Casimir and Polder, 1948] Casimir, H. B. and Polder, D. (1948). The influence of retardation on the london-van der waals forces. *Physical Review*, 73(4):360.

[Chin et al., 2010] Chin, C., Grimm, R., Julienne, P., and Tiesinga, E. (2010). Feshbach resonances in ultracold gases. *Reviews of Modern Physics*, 82(2):1225.

[Chu, 1992] Chu, S. (1992). Laser trapping of neutral particles. *Scientific American*, 266(2):70–77.

[Cohen-Tannoudji et al., 1998] Cohen-Tannoudji, C., Dupont-Roc, J., and Grynberg, G. (1998). Atom-photon interactions: basic processes and applications. *Atom-Photon Interactions: Basic Processes and Applications, by Claude Cohen-Tannoudji, Jacques Dupont-Roc, Gilbert Grynberg, pp. 678. ISBN 0-471-29336-9. Wiley-VCH, March 1998.*, page 678.

[Cornell and Wieman, 2002] Cornell, E. A. and Wieman, C. E. (2002). Nobel lecture: Bose-einstein condensation in a dilute gas, the first 70 years and some recent experiments. *Reviews of Modern Physics*, 74(3):875.

[Dalfovo et al., 1999] Dalfovo, F., Giorgini, S., Pitaevskii, L. P., and Stringari, S. (1999). Theory of bose-einstein condensation in trapped gases. *Reviews of Modern Physics*, 71(3):463.

[Das et al., 2016] Das, S. R., Mohammed, A. M., Maize, K., Sadeque, S., Shakouri, A., Janes, D. B., and Alam, M. A. (2016). Evidence of universal temperature scaling in self-heated percolating networks. *Nano letters*, 16(5):3130–3136.

[Dashti and Stuart, 2016] Dashti, M. and Stuart, A. M. (2016). The bayesian approach to inverse problems. *Handbook of Uncertainty Quantification*, pages 1–118.

[Davis, 1996] Davis, C. C. (1996). *Lasers and electro-optics: fundamentals and engineering*. Cambridge university press.

[Donley et al., 2005] Donley, E. A., Heavner, T. P., Levi, F., Tataw, M., and Jefferts, S. R. (2005). Double-pass acousto-optic modulator system. *Review of Scientific Instruments*, 76(6):063112.

[Dormand and Prince, 1980] Dormand, J. R. and Prince, P. J. (1980). A family of embedded runge-kutta formulae. *Journal of computational and applied mathematics*, 6(1):19–26.

[Durfee and Ketterle, 1998] Durfee, D. S. and Ketterle, W. (1998). Experimental studies of bose-einstein condensation. *Optics Express*, 2(8):299–313.

[Edelstein, 2007] Edelstein, A. (2007). Advances in magnetometry. *Journal of Physics: Condensed Matter*, 19(16):165217.

[Egorov et al., 2013] Egorov, M., Opanchuk, B., Drummond, P., Hall, B., Hannaford, P., and Sidorov, A. (2013). Measurement of s-wave scattering lengths in a two-component bose-einstein condensate. *Physical Review A*, 87(5):053614.

[Estève, 2004] Estève, J. (2004). *Du miroir au guide d'onde atomique: effets de rugosité*. PhD thesis.

[Fantanas et al., 2018] Fantanas, D., Brunton, A., Henley, S., and Dorey, R. (2018). Investigation of the mechanism for current induced network failure for spray deposited silver nanowires. *Nanotechnology*, 29(46):465705.

[Feynman, 1964] Feynman, R. P. (1964). Feynman lectures on physics. volume 2: Mainly electromagnetism and matter. *Reading, Ma.: Addison-Wesley, 1964, edited by Feynman, Richard P.; Leighton, Robert B.; Sands, Matthew.*

[Feynman, 1965] Feynman, R. P. (1965). Feynman lectures on physics. volume 3: Quantum mechancis. *Reading, Ma.: Addison-Wesley, 1965, edited by Feynman, Richard P.; Leighton, Robert B.; Sands, Matthew.*

[Folman et al., 2008] Folman, R., Kruger, P., Schmiedmayer, J., Denschlag, J., and Henkel, C. (2008). Microscopic atom optics: from wires to an atom chip. *arXiv preprint arXiv:0805.2613*.

[Foot et al., 2005] Foot, C. J. et al. (2005). *Atomic physics*, volume 7. Oxford University Press.

[Freeman and Choi, 2001] Freeman, M. and Choi, B. (2001). Advances in magnetic microscopy. *Science*, 294(5546):1484–1488.

[Gadge, 2018] Gadge, A. (2018). *A cold atom apparatus for the microscopy of thin membranes*. PhD thesis, University of Nottingham.

[Garnett et al., 2012] Garnett, E. C., Cai, W., Cha, J. J., Mahmood, F., Connor, S. T., Christoforo, M. G., Cui, Y., McGehee, M. D., and Brongersma, M. L. (2012). Self-limited plasmonic welding of silver nanowire junctions. *Nature materials*, 11(3):241.

[Gerbier, 2004] Gerbier, F. (2004). Quasi-1D Bose-Einstein condensates in the dimensional crossover regime. *Europhysics Letters*, 66(6):771–777.

[Gradshteyn and Ryzhik, 2014] Gradshteyn, I. S. and Ryzhik, I. M. (2014). *Table of integrals, series, and products*. Academic press.

[Griffin et al., 1996] Griffin, A., Snoke, D. W., and Stringari, S. (1996). *Bose-einstein condensation*. Cambridge University Press.

[Griffiths, 1962] Griffiths, D. J. (1962). *Introduction to electrodynamics*. Prentice Hall New Jersey.

[Haverkate and Feiner, 2006] Haverkate, L. and Feiner, L. (2006). Optical properties of cylindrical nanowires.

[Hong et al., 2015] Hong, S., Yeo, J., Lee, J., Lee, H., Lee, P., Lee, S. S., and Ko, S. H. (2015). Selective laser direct patterning of silver nanowire percolation network transparent conductor for capacitive touch panel. *Journal of nanoscience and nanotechnology*, 15(3):2317–2323.

[Jooya et al., 2013] Jooya, K., Musterer, N., Madison, K. W., and Booth, J. L. (2013). Photon-scattering-rate measurement of atoms in a magneto-optical trap. *Physical Review A*, 88(6):063401.

[Kawasaki et al., 2015] Kawasaki, A., Braverman, B., Yu, Q., and Vuletic, V. (2015). Two-color magneto-optical trap with small magnetic field for ytterbium. *Journal of Physics B: Atomic, Molecular and Optical Physics*, 48(15):155302.

[Ketterle, 2002] Ketterle, W. (2002). Nobel lecture: When atoms behave as waves: Bose-einstein condensation and the atom laser. *Reviews of Modern Physics*, 74(4):1131.

[Ketterle et al., 1998] Ketterle, W., Durfree, D., and Stamper-Kurn, D. (1998). Making, probing and understanding bose-einstein condensates, contribution to the proceedings of the 1998 enrico fermi summer school on bose-einstein condensation in varenna, italy.

[Ketterle and Van Druten, 1996] Ketterle, W. and Van Druten, N. (1996). Evaporative cooling of trapped atoms. In *Advances in atomic, molecular, and optical physics*, volume 37, pages 181–236. Elsevier.

[Kim et al., 2005] Kim, K., Lee, K.-H., Heo, M., Noh, H.-R., and Jhe, W. (2005). Measurement of the trap properties of a magneto-optical trap by a transient oscillation method. *Physical Review A*, 71(5):053406.

[Kirtley et al., 1996] Kirtley, J., Tsuei, C., Rupp, M., Sun, J., Yu-Jahnes, L. S., Gupta, A., Ketchen, M., Moler, K., and Bhushan, M. (1996). Direct imaging of integer and half-integer josephson vortices in high-t c grain boundaries. *Physical review letters*, 76(8):1336.

[Kominis et al., 2003] Kominis, I., Kornack, T., Allred, J., and Romalis, M. V. (2003). A subfemtotesla multichannel atomic magnetometer. *Nature*, 422(6932):596.

[Kosloff and Kosloff, 1983] Kosloff, D. and Kosloff, R. (1983). A fourier method solution for the time dependent schrödinger equation as a tool in molecular dynamics. *Journal of Computational Physics*, 52(1):35–53.

[Krüger et al., 2005] Krüger, P., Wildermuth, S., Hofferberth, S., Andersson, L. M., Groth, S., Bar-Joseph, I., and Schmiedmayer, J. (2005). Cold atoms close to surfaces: measuring magnetic field roughness and disorder potentials. In *Journal of Physics: Conference Series*, volume 19, page 56. IOP Publishing.

[Kumar and Zhou, 2010] Kumar, A. and Zhou, C. (2010). The race to replace tin-doped indium oxide: which material will win? *ACS nano*, 4(1):11–14.

[Langley et al., 2014] Langley, D., Lagrange, M., Giusti, G., Jiménez, C., Bréchet, Y., Nguyen, N. D., and Bellet, D. (2014). Metallic nanowire networks: effects of thermal annealing on electrical resistance. *Nanoscale*, 6(22):13535–13543.

[Langlois and Coeuret, 1989] Langlois, S. and Coeuret, F. (1989). Flow-through and flow-by porous electrodes of nickel foam. i. material characterization. *Journal of applied electrochemistry*, 19(1):43–50.

[Lanza, 2017] Lanza, M. (2017). *Conductive Atomic Force Microscopy: Applications in Nanomaterials*. John Wiley & Sons.

[Large, 2016] Large, M. J. (2016). *Structure-Property Relationships in Silver Nanowire Coatings*. PhD thesis, University of Surrey (United Kingdom).

[Le Kien and Hakuta, 2004] Le Kien, F. and Hakuta, K. (2004). Density operator and applications in nonlinear optics. *Lecture Notes, University of Electro-Communications, Japan*, 11.

[Lee et al., 2013] Lee, J., Grover, J., Orozco, L., and Rolston, S. (2013). Sub-doppler cooling of neutral atoms in a grating magneto-optical trap. *JOSA B*, 30(11):2869–2874.

[Levi, 2001] Levi, B. G. (2001). Cornell, ketterle, and wieman share nobel prize for bose-einstein condensates. *Physics Today*, 54(12):14–16.

[Li and Zhang, 2009] Li, J. and Zhang, S.-L. (2009). Finite-size scaling in stick percolation. *Physical Review E*, 80(4):040104.

[Li and Zhang, 2010] Li, J. and Zhang, S.-L. (2010). Conductivity exponents in stick percolation. *Physical Review E*, 81(2):021120.

[Lu et al., 1996] Lu, Z., Corwin, K., Renn, M., Anderson, M., Cornell, E. A., and Wieman, C. (1996). Low-velocity intense source of atoms from a magneto-optical trap. *Physical review letters*, 77(16):3331.

[Manning et al., 2018] Manning, H. G., Niosi, F., da Rocha, C. G., Bellew, A. T., O'Callaghan, C., Biswas, S., Flowers, P. F., Wiley, B. J., Holmes, J. D., Ferreira, M. S., et al. (2018). Emergence of winner-takes-all connectivity paths in random nanowire networks. *Nature communications*, 9(1):3219.

[Marcassa et al., 1993] Marcassa, L., Bagnato, V., Wang, Y.-j., Tsao, C., Weiner, J., Dulieu, O., Band, Y., and Julienne, P. S. (1993). Collisional loss rate in a magneto-optical trap for sodium atoms: Light-intensity dependence. *Physical Review A*, 47(6):R4563.

[McCarron, 2007] McCarron, D. (2007). A guide to acousto-optic modulators. *http://massey. dur. ac. uk/resources/slcornish/AOMGuide. pdf*.

[Mertens and Moore, 2012] Mertens, S. and Moore, C. (2012). Continuum percolation thresholds in two dimensions. *Physical Review E*, 86(6):061109.

[Metcalf, 1989] Metcalf, H. (1989). Magneto-optical trapping and its application to helium metastables. *JOSA B*, 6(11):2206–2210.

[Metcalf and van der Straten, 2001] Metcalf, H. and van der Straten, P. (2001). *Laser Cooling and Trapping*. Graduate Texts in Contemporary Physics. Springer New York.

[Minami, 2008] Minami, T. (2008). Present status of transparent conducting oxide thin-film development for indium-tin-oxide (ito) substitutes. *Thin Solid Films*, 516(17):5822–5828.

[Mutiso and Winey, 2013] Mutiso, R. M. and Winey, K. I. (2013). Electrical percolation in quasi-two-dimensional metal nanowire networks for transparent conductors. *Physical Review E*, 88(3):032134.

[Ni et al., 2018] Ni, X., Hui, C., Su, N., Jiang, W., and Liu, F. (2018). Monte carlo simulations of electrical percolation in multicomponent thin films with nanofillers. *Nanotechnology*, 29(7):075401.

[Nichols and Hull, 1903] Nichols, E. F. and Hull, G. F. (1903). The pressure due to radiation.(second paper.). *Physical Review (Series I)*, 17(1):26.

[Nolting et al., 2000] Nolting, F., Scholl, A., Stöhr, J., Seo, J. W., Fompeyrine, J., Siegwart, H., Locquet, J.-P., Anders, S., Lüning, J., Fullerton, E., et al. (2000). Direct observation of the alignment of ferromagnetic spins by antiferromagnetic spins. *Nature*, 405(6788):767.

[Overstreet et al., 2005] Overstreet, K., Zabawa, P., Tallant, J., Schwettmann, A., and Shaffer, J. (2005). Multiple scattering and the density distribution of a Cs MOT. *OPTICS EXPRESS*, 13(24):9672–9682.

[Park et al., 2015] Park, H.-G., Heo, G.-S., Park, S.-G., Jeong, H.-C., Lee, J. H., and Seo, D.-S. (2015). Silver nanowire networks as transparent conducting films for liquid crystal displays. *ECS Solid State Letters*, 4(10):R50–R52.

[Pethick and Smith, 2008] Pethick, C. J. and Smith, H. (2008). *Bose–Einstein condensation in dilute gases*. Cambridge university press.

[Petrich et al., 1995] Petrich, W., Anderson, M. H., Ensher, J. R., and Cornell, E. A. (1995). Stable, tightly confining magnetic trap for evaporative cooling of neutral atoms. *Physical Review Letters*, 74(17):3352.

[Phillips, 1998a] Phillips, W. (1998a). Laser cooling and trapping of neutral atoms. *Reviews of Modern Physics*, 70(3):721–741.

[Phillips, 1998b] Phillips, W. D. (1998b). Nobel lecture: Laser cooling and trapping of neutral atoms. *Reviews of Modern Physics*, 70(3):721.

[Phillips and Metcalf, 1987] Phillips, W. D. and Metcalf, H. J. (1987). Cooling and trapping atoms. *Scientific American*, 256(3):50–57.

[Pollock et al., 2009] Pollock, S., Cotter, J., Laliotis, A., and Hinds, E. (2009). Integrated magneto-optical traps on a chip using silicon pyramid structures. *Optics Express*, 17(16):14109–14114.

[Prentiss et al., 1988] Prentiss, M., Cable, A., Bjorkholm, J., Chu, S., Raab, E., and Pritchard, D. (1988). Atomic-density-dependent losses in an optical trap. *Optics letters*, 13(6):452–454.

[Proukakis et al., 2017] Proukakis, N. P., Snoke, D. W., and Littlewood, P. B. (2017). *Universal themes of Bose-Einstein condensation*. Cambridge University Press.

[Qiang et al., 2012] Qiang, C., Xin-Yu, L., Kui-Yi, G., Xiao-Rui, W., Dong-Min, C., and Ru-Quan, W. (2012). Improved atom number with a dual color magneto-optical trap. *Chinese Physics B*, 21(4).

[Raab et al., 1987] Raab, E., Prentiss, M., Cable, A., Chu, S., and Pritchard, D. E. (1987). Trapping of neutral sodium atoms with radiation pressure. *Physical Review Letters*, 59(23):2631.

[Radwell et al., 2013] Radwell, N., Walker, G., and Franke-Arnold, S. (2013). Ultra high densities of cold atoms in a holographically controlled dark spot trap. *arXiv preprint arXiv:1308.4586*.

[Reinaudi et al., 2007] Reinaudi, G., Lahaye, T., Wang, Z., and Guéry-Odelin, D. (2007). Strong saturation absorption imaging of dense clouds of ultracold atoms. *Optics letters*, 32(21):3143–3145.

[Rondin et al., 2014] Rondin, L., Tetienne, J.-P., Hingant, T., Roch, J.-F., Maletinsky, P., and Jacques, V. (2014). Magnetometry with nitrogen-vacancy defects in diamond. *Reports on progress in physics*, 77(5):056503.

[Rosi et al., 2018] Rosi, S., Burchianti, A., Conclave, S., Naik, D. S., Roati, G., Fort, C., and Minardi, F. (2018). Lambda-enhanced grey molasses on the D2 transition of Rubidium-87 atoms. *Scientific Reports*, 8.

[Roth et al., 1989] Roth, B. J., Sepulveda, N. G., and Wikswo Jr, J. P. (1989). Using a magnetometer to image a two-dimensional current distribution. *Journal of applied physics*, 65(1):361–372.

[Roy et al., 2017] Roy, R., Condylis, P. C., Prakash, V., Sahagun, D., and Hessmo, B. (2017). A minimalistic and optimized conveyor belt for neutral atoms. *Scientific reports*, 7(1):13660.

[Rudolph et al., 2015] Rudolph, J., Herr, W., Grzeschik, C., Sternke, T., Grote, A., Popp, M., Becker, D., Müntinga, H., Ahlers, H., Peters, A., et al. (2015). A high-flux bec source for mobile atom interferometers. *New Journal of Physics*, 17(6):065001.

[Saiko et al., 2014] Saiko, A., Fedaruk, R., and Markevich, S. (2014). Relaxation, decoherence, and steady-state population inversion in qubits doubly dressed by microwave and radiofrequency fields. *Journal of Physics B: Atomic, Molecular and Optical Physics*, 47(15):155502.

[Saint et al., 2018] Saint, R., Evans, W., Zhou, Y., Barrett, T., Fromhold, T., Saleh, E., Maskery, I., Tuck, C., Wildman, R., Oručević, F., et al. (2018). 3d-printed components for quantum devices. *Scientific reports*, 8(1):8368.

[Sannicolo et al., 2016] Sannicolo, T., Munoz-Rojas, D., Nguyen, N. D., Moreau, S., Celle, C., Simonato, J.-P., Brechet, Y., and Bellet, D. (2016). Direct imaging of the onset of electrical conduction in silver nanowire networks by infrared thermography: evidence of geometrical quantized percolation. *Nano letters*, 16(11):7046–7053.

[Shaw et al., 2016] Shaw, J. E., Perumal, A., Bradley, D. D., Stavrinou, P. N., and Anthopoulos, T. D. (2016). Nanoscale current spreading analysis in solution-processed graphene oxide/silver nanowire transparent electrodes via conductive atomic force microscopy. *Journal of Applied Physics*, 119(19):195501.

[Sinuco-León et al., 2018] Sinuco-León, G. A., Krüger, P., and Fromhold, T. (2018). Atom chips with free-standing two-dimensional electron gases: advantages and challenges. *Journal of Modern Optics*, 65(5-6):677–692.

[Smith et al., 2011] Smith, D. A., Aigner, S., Hofferberth, S., Gring, M., Andersson, M., Wildermuth, S., Krüger, P., Schneider, S., Schumm, T., and Schmiedmayer, J. (2011). Absorption imaging of ultracold atoms on atom chips. *Optics express*, 19(9):8471–8485.

[Steane et al., 1992] Steane, A., Chowdhury, M., and Foot, C. (1992). Radiation force in the magneto-optical trap. *JOSA B*, 9(12):2142–2158.

[Steane and Foot, 1991] Steane, A. and Foot, C. (1991). Laser cooling below the doppler limit in a magneto-optical trap. *EPL (Europhysics Letters)*, 14(3):231.

[Steck, 2001] Steck, D. A. (2001). Rubidium 87 d line data. visited on 17/09/2019.

[Steck, 2007] Steck, D. A. (2007). Quantum and atom optics. visited on 17/09/2019.

[Stuart, 2010] Stuart, A. M. (2010). Inverse problems: a bayesian perspective. *Acta numerica*, 19:451–559.

[Stutzman and Thiele, 2012] Stutzman, W. L. and Thiele, G. A. (2012). *Antenna theory and design*. John Wiley & Sons.

[Tetienne et al., 2017] Tetienne, J.-P., Dontschuk, N., Broadway, D. A., Stacey, A., Simpson, D. A., and Hollenberg, L. C. (2017). Quantum imaging of current flow in graphene. *Science advances*, 3(4):e1602429.

[Townsend et al., 1995] Townsend, C., Edwards, N., Cooper, C., Zetie, K., Foot, C., Steane, A., Szriftgiser, P., Perrin, H., and Dalibard, J. (1995). Phase-space density in the magneto-optical trap. *Physical Review A*, 52(2):1423.

[USGS, 2020] USGS, S. (2020). Mineral commodity summaries 2020. visited on 27/07/2020.

[Van De Groep et al., 2012] Van De Groep, J., Spinelli, P., and Polman, A. (2012). Transparent conducting silver nanowire networks. *Nano letters*, 12(6):3138–3144.

[Vengalattore et al., 2004] Vengalattore, M., Conroy, R., and Prentiss, M. (2004). Enhancement of phase space density by increasing trap anisotropy in a magneto-optical trap with a large number of atoms. *Physical review letters*, 92(18):183001.

[Vengalattore et al., 2007] Vengalattore, M., Higbie, J., Leslie, S., Guzman, J., Sadler, L., and Stamper-Kurn, D. (2007). High-resolution magnetometry with a spinor bose-einstein condensate. *Physical review letters*, 98(20):200801.

[Vinaji et al., 2009] Vinaji, S., Lochthofen, A., Mertin, W., Regolin, I., Gutsche, C., Prost, W., Tegude, F., and Bacher, G. (2009). Material and doping transitions in single gaas-based nanowires probed by kelvin probe force microscopy. *Nanotechnology*, 20(38):385702.

[Vuletic et al., 1998] Vuletic, V., Fischer, T., Praeger, M., Hänsch, T., and Zimmermann, C. (1998). Microscopic magnetic quadrupole trap for neutral atoms with extreme adiabatic compression. *Physical review letters*, 80(8):1634.

[Weiner et al., 1999] Weiner, J., Bagnato, V., Zilio, S., and Julienne, P. (1999). Experiments and theory in cold and ultracold collisions. *Reviews of Modern Physics*, 71(1):1–85.

[West et al., 1996] West, D. B. et al. (1996). *Introduction to graph theory*, volume 2. Prentice hall Upper Saddle River, NJ.

[Wildermuth et al., 2005] Wildermuth, S., Hofferberth, S., Lesanovsky, I., Haller, E., Andersson, L., Groth, S., Bar-Joseph, I., Kruger, P., and Schmiedmayer, J. (2005). Bose-Einstein condensates - Microscopic magnetic-field imaging. *Nature*, 435(7041):440.

[Wilkens et al., 2000] Wilkens, M., Illuminati, F., and Krämer, M. (2000). Dependence of the bec transition temperature on interaction strength: A perturbative analysis. *arXiv preprint cond-mat/0001422*.

[Xu et al., 2002] Xu, X., Loftus, T. H., Smith, M. J., Hall, J. L., Gallagher, A., and Ye, J. (2002). Dynamics in a two-level atom magneto-optical trap. *Physical Review A*, 66(1):011401.

[Yang et al., 2017] Yang, F., Kollár, A. J., Taylor, S. F., Turner, R. W., and Lev, B. L. (2017). Scanning quantum cryogenic atom microscope. *Physical Review Applied*, 7(3):034026.

[Youk, 2005] Youk, H. (2005). Numerical study of quadrupole magnetic traps for neutral atoms: anti-helmholtz coils and a u-chip. *Canadian Undergraduate Physics Journal*, 3(2):13–18.